TOWARDS A CELLULAR ARCHITECTURE OF THREE-DIMENSIONAL ARRAY OF MUSCLE FIBERS

A THESIS TO BE SUBMITTED TO

THE UNIVERSITY OF TRANS-DISCIPLINARY HEALTH SCIENCES AND TECHNOLOGY

FOR THE AWARD OF THE DEGREE OF

DOCTOR OF PHILOSOPHY

BY

DRISYA DILEEP

UNDER THE GUIDANCE OF

DR MINHAJ SIRAJUDDIN

INSTEM, BANGALORE

MAY 2024

THE UNIVERSITY OF TRANS-DISCIPLINARY HEALTH SCIENCES AND TECHNOLOGY

Private University Established in Karnataka by ACT 35 of 2013

BENGALURU - 560064

DECLARATION BY THE CANDIDATE

I declare that this thesis, entitled "**Towards a cellular architecture of three-dimensional array of muscle fibers**" submitted for the award of Doctor of Philosophy to THE UNIVERSITY OF TRANS-DISCIPLINARY HEALTH SCIENCES AND TECHNOLOGY, Bengaluru, is my original work, conducted under the supervision of my guide, Dr. Minhaj Sirajuddin. I also wish to inform that no part of the research has been submitted for a degree or examination at any university. References, assistance, and materials obtained from other sources have been duly acknowledged.

I hereby confirm the originality of this work and that there is no plagiarism in any part of the dissertation.

Place: Bengaluru **Signature of the Candidate**

Date: 29th May 2024

Name of candidate: Drisya Dileep

Reg. No.: 20418020209

(May/2019)

THE UNIVERSITY OF TRANS-DISCIPLINARY HEALTH SCIENCES AND TECHNOLOGY

Private University Established in Karnataka by ACT 35 of 2013

BENGALURU - 560064

CERTIFICATE

This is to certify that the work incorporated in this thesis "**Towards a cellular architecture of three-dimensional array of muscle fibers**" submitted by **Drisya Dileep** was carried out under my supervision. No part of this thesis has been submitted for a degree or examination to any other university. References, assistance, and materials obtained from other sources have been duly acknowledged. I hereby confirm the originality of this work and that there is no plagiarism in any part of the dissertation.

Date: 29th May 2024 **Signature of Research Supervisor**

Research Supervisor :
Dr. Minhaj Sirajuddin
Associate Investigator
Centre for cardiovascular development and disease mechanisms (CCBD)
Institute for stem cell science and regenerative medicine (inStem)
Bangalore life science cluster
GKVK campus, Bellary road, Bangalore-560065, India

This thesis is dedicated to Sandeep

ACKNOWLEDGEMENT

I would like to start by thanking Minhaj, my thesis advisor. I began working in Minhaj's lab as a JRF and eventually continued my PhD there because I was drawn to his philosophy of a happy lab. I gained a lot of knowledge from his mentorship and I always admired his approachability in both science and life. There were uncertainties, just as in many other PhD stories of other students, but his unwavering support and direction inspired me to complete my research without incident. I appreciate all the flexibility he gave me and the confidence he placed on me to complete this task.

The biological impact of our study has gained momentum with computer vision analysis, thanks to our collaboration with Dr. Kaleem Siddiqi's lab. Being able to work alongside Kaleem and Tabish was enjoyable. I was patiently and kindly guided by the fundamentals of computer vision algorithms used in our analysis by Kaleem and Tabish. I would like to thank Kaleem for the impeccable mentorship he provided during this project. I thank Tabish for all his efforts because without the hard work he put into developing the computational pipeline for the project's quantitative analysis, this thesis would not have been complete. I appreciate Tyler's assistance with visualizations that made our findings more aesthetically striking.

I thank Dr. Ramkumar Sambasivan (Ram) and Dr. Dhandapany Perundurai (Dhan), members of my thesis committee, for their insightful comments and fruitful conversations regarding my thesis research work.

I appreciate Dr. Jyotsna Dhawan and Dr. Sankar Srinivas for taking the time to talk with me and for their inputs for the preliminary details of my thesis proposal. In early attempts, training with microscopes and imaging was greatly aided by Dr. Manoj Mathew, the former facilities in charge of CIFF, and Dr. Ganesh from Olympus, who provided support.

I thank CSIR for the fellowship and the University of Trans-disciplinary Health Sciences and Technology (TDU) for the registration. I appreciate Ravi Kumar from TDU and Valsala from the inStem academic office for helping me complete the necessary paperwork for my PhD thesis. I appreciate the formalities with the CSIR fellowship documents done by Sunitha, Shobha, Shrikant, and Raju.

Members of the Minhaj Lab in the past and present have consistently adhered to the philosophy of a happy lab. I was introduced to the lively lab environment by the first generation of PhD students and postdocs, who also helped me realize how fun life might

be throughout the early to mid-stages of my PhD career. It had been pleasure working with Archana, Lama, Shubham, Mamta, Archita, Lakshmi, Sujana, Venkat, and Ipsa. Sharing the lab space with Nivya, Rayees, Sarika, Susobhan, Ishan, Anwesha, Kaiser, and Victor is enjoyable. I learned to recognize the necessity for various viewpoints to be applied to different challenges in science and life from the Minhaj lab setting, which included many people from diverse Indian-geographical/cultural origins. I appreciate the summer interns I got to work with, Aurelia and Sapna, for their time in accompanying some steps and attempting some visualizations respectively. I thank all the people I interacted with in the past and present as part of the Minhaj lab.

I would like to thank the former members of the Dhan lab, Anupam, Adithi, Ilayarajan, and Deepak, for their support and assistance in handling the mice. I appreciate everyone who has engaged in conversations from Dhan Lab and Tina Lab in the past and present. I thank Dr. Aditi Bhattacharya and Dr. Siddhartha Datta for their support in providing with rat heart samples.

Those who work in the CIFF, lab kitchen, instrumentation, IT, civil, electrical, housekeeping, canteen, stores, medical, reception, security, and other departments at the BLisc campus owe heartfelt thanks for their services. I appreciate the feedback and reagent shared with me from the BLisc campus personnel from different labs.

I am fortunate to have known Ashina and Shubham for many years, and several conversations with them helped me look at life more positively. It was enjoyable to talk with Cyrin, Athira, Athma and Vijaya about issues pertaining to uncertainty in research and I am thankful to them. Finally, I would like to thank my family for their support. Sandeep has been a blessing in my life for his companionship and his appreciation for my passion. I am grateful to everyone who encouraged me, including my parents- Jessy & Dileep, Gowtham, Deepu Maman, my in-laws- Sheebha & Jayarajan, grandparents, teachers, Achamma, Sangeeth, Naila, and other well-wishers.

Table of figures

List of Appendix Tables

List of Appendix Figures

LIST OF ACRYONYMS

mya: Million years ago
DT-MRI: Diffusion-tensor magnetic resonance imaging
DCM: Dilated cardiomyopathy
HCM: Hypertrophic cardiomyopathy
PSAX-PML: Parasternal short axis- papillary muscle
HLA-4C: Horizontal long axis-4 chamber
SNR: Signal to Noise Ratio
MI: Myocardial Infarction.
CM: Cardiomyocytes
EC: Endothelial cells fibroblasts
SMC: Smooth muscle cells
FB: Fibroblasts
mm: Millimeter
μm: Micrometer
FoV: Field of view
PPM: Papillary Muscle
LAD: Left anterior descending
LCX: Left circumflex artery
RCX: Right circumflex artery
RCA: Right coronary artery
RV: Right ventricle
LV: Left ventricle
RyR: Ryanodine Receptors
MyBPC3: Myosine binding protein C3
PKC: Protein kinase C
DMD: Duchenne muscular dystrophy
AHA: American heart association
AV: Atrio ventricular
RI: Refractive index

AUTHOR CONTRIBUTION

The author of this thesis played a leading role in conceptualizing and implementing the biological aspects and interpreting the outcome of the data analysis of this project in consultation with Dr. Minhaj Sirajuddin. This included sample preparation, 3D-confocal imaging, hand segmentation of the test datasets, data analysis, and interpretation. In collaboration with Dr. Tabish Syed, the author optimized the computational pipeline for data analysis, testing ground truth data, and interpreting the results. Dr. Tabish Syed provided codes for the computational pipeline, including pre-processing, stitching of fields of view, and orientation reconstructions in consultation with Dr. Kaleem Siddiqi. Dr. Syed also helped in the implementation of the algorithms. Dr. Tyler Sloan developed high-resolution visualizations of the streamlines and glyphs used in some figures.

SYNOPSIS

The geometric organization of myofibers in the mammalian heart wall supports synchronous contraction and electrical conduction while also providing mechanical strength. The mammalian heart wall is densely packed with cardiomyocytes that are aligned end-to-end to form them (1). Myofiber malformations can result in pathological cardiac illnesses, including cardiomyopathy, remodelling after myocardial infarction, and electrical propagation (1). Myofibers have been described as a helical continuum on a coarse spatial scale, looping around the heart chambers (1,2). A three-layer model(3) and descriptions such as nested donuts, toroids and pretzels(4), and a single helical band are among the competing models of fiber organization that still exist (5). Despite the lack of an agreed-upon model, the current heart wall fiber geometry models used in cardiovascular research are primarily obtained from millimeter-resolution diffusion-tensor magnetic resonance imaging (DT-MRI)(4,6–9). These models consistently support a smooth counter clockwise rotation of the heart wall fibers in transmural penetration and, by definition, forbid singularities in fiber orientation. There are also myofiber orientation rule-based models and minimal surface models that are generally in line with the DT capabilities of MRI (10). In addition, statistical atlases of fiber geometry derived from imaging of numerous participants were obtained using DT-MRI (11,12). While these models can progress research on the electrical and mechanical functions of the heart wall (13), they all have issues with spatial resolution because, at this scale, hundreds of cardiomyocytes can fill a single voxel.

Micron-scale light microscopy allows the recovery of myofiber shape at the resolution of individual cardiomyocytes. However, studies in this area have so far concentrated on thin sections of heart tissue (11) or 3D stacks of heart tissue without determining myofiber geometry (15,16), or based on histological sections that are typically only suitable for two-dimensional imaging (17,18). Recent research has not recovered myofiber or cardiomyocyte orientation at the whole-heart scale. Remarkably, the geometry and orientation of cardiomyocytes with respect to myofibers at the micron scale remain unknown.

To address this fundamental issue, we integrated computer vision methods with deep and wide imaging based on confocal light microscopy. Using these two techniques, we were able to determine the micron-scale orientations of cardiomyocytes over the whole

long- and short-axis ventricular regions of mouse hearts. Our three-dimensional reconstructions at exceptional spatial resolution uncovers previously unreported long-axis bands of fibers at the outer ventricle walls and are distinct from the helical or circumferential myofibers. This finding marks a conceptual advance in understanding the architecture of myofibers of the heart. Virtually all computational models of heart-wall contraction or electrical wave propogation do not include the unique long-axis outer-wall fiber structure. Its involvement could significantly improve our understanding of heart wall mechanics and electrical conduction and create new avenues for research on disorders associated with changes in fiber organization at different spatial scales in the heart wall tissue.

The current study titled '**Towards a cellular architecture of three dimensional array of muscle fibers'** is divided into six chapters.

Chapter 1 outlines and reviews the literature on heart wall geometry and open questions. Chapter 2 describes the Objectives and experimental approach of the study. Integrating fluorescence-based micron-scale heart imaging, geometric image analysis, and myofiber reconstruction methods for microscopic images is a crucial advancement in our study. This combination led to a resolution gain of three orders of magnitude in scale (i.e., from millimeters to microns), revealing an entirely new fiber system that has escaped discovery by previous lower-resolution imaging methods. A detailed description of our pipeline and findings will be highlighted in Chapters 3 and 4. The results of this study have been communicated and are currently under submission. A preprint version of this manuscript titled 'Myofiber reconstruction at micron scale reveals longitudinal bands in heart ventricular walls'available at the biorXiv repository. The current limitations of this study are explained in Chapter 5. Our cardiomyocyte orientation reconstructions from thick heart tissue sections can lay the foundation for future pipeline establishment for cellular-scale imaging of cleared intact mouse hearts in their native context and disease states. Chapter 6 discusses these future directions and our attributes for the present understanding of heart wall mechanics, adding implications for studying diseases related to myofiber disorganization.

Motivation for this thesis

Given the crucial role that myofiber organization of the heart wall plays in regulating electrical conduction and dynamics of the heart wall, recovering cardiomyocyte and myofiber geometry at the cellular level is of utmost importance. The majority of available models, which function at the millimeter scale, show a continuous network of helical fibers rotating from the outer to inner walls in a clockwise orientation; however, they are unable to arrive at a common model. The present heart wall models, primarily developed from DT-MRI and millimeter-scale imaging, are insufficient because they may fit hundreds of cardiomyocytes in a single voxel and lack cellular-scale information. We sought to reproduce the intricate geometry of myocytes and myofibers in the ventricular walls at the micron scale using confocal microscopy and computer vision techniques. This discovery could make essential advancements in our understanding of the structure and operation of the heart walls.

Chapter 2: Objectives

The primary objective of this thesis is to elucidate the 3D architecture of cardiomyocyte orientation for intact ventricular heart tissue at a micron-meter scale resolution. The output from this work will enable us to comprehend the blueprint for the cellular architecture of a wild-type heart, as it is controlled by cardiomyocytes. This can be applied to understand the modifications in cardiomyocyte orientation induced by dilated cardiomyopathy (DCM) and hypertrophic cardiomyopathy (HCM).

The specific objectives of this study are detailed below.

1. Establish a pipeline for tissue preparation for deep imaging using confocal microscopy.
2. Integrative approaches for deep tissue image analysis and estimation of myofiber orientation.
3. 3D reconstruction of myofiber orientation using tractography at cellular/micron scale.

Chapter 3: Methods and Materials

Sample preparation and imaging:

We obtained mouse and rat hearts from wild-type female C57BL/6 and Wistar strains, respectively. All cardiac samples were perfused with 1X PBS that was heparinized to prevent blood clots. We used a modified CLARITY technique to clear heart tissue (19).As illustrated in Fig. 1A, cleared mouse hearts, uncleared fixed mouse hearts, and rat hearts were sectioned into short- and long-axis sections using Compresstome VF-300. For labeling, we used wheat germ agglutinin (WGA, W21404, Thermo Fisher) conjugated to Alexa Fluor 633 at 150 µg/ml. The heart tissues were stained with WGA and then placed in RIMS imaging solution (88 percent Histodenz, Sigma D2158 in 20mM Phosphate buffer, pH 7.5). The cardiac tissues were then mounted with a spacer and two coverslips of 170µm thickness. Confocal images were taken using an Olympus FV3000 confocal microscope coupled with Olympus PlanApo 1.25X and Olympus UCPLFN 20X CorrM32 85 mm scale air objectives (NA=0.73). A lower magnification image that covered the entire tissue block area was created for each section using a 1.25X objective. Olympus FluoView^{TM} software was used to map the field of view. 320x320 pixel fields of view with isometric voxel sizes of 1.98 μm^3 was used with a 20X objective for micron-scale imaging. Image stacks with maximum depths of 300 µm and 50 µm were acquired for cleaned and uncleared heart tissues. The sample was excited with a 640 nm laser line, and an emission between 650 and 670 nm was recorded.

Pre-processing of heart tissue image stacks:

We employed iterative Richardson-Lucy deconvolution along with total variation regularization for deconvolution to deal with the nonideal point spread function (PSF). Unsupervised denoising was applied to deconvolved image stacks using a dictionary learning technique. The overlapping fields of view were tiled using phase correlation in the Fourier domain between the adjacent fields of view.

Estimation of cell orientation using structure tensor and myofiber reconstruction:

The intensity gradient of the WGA stain, which was absorbed by cell membranes (Fig. 1B) was used to calculate myocyte orientation. We computed the structure tensor for each voxel in the stack of the deconvolved and denoised images. To capture the long-axis orientation of myocytes, we assigned the orientation in the direction where the intensity fluctuated the least to each voxel. To verify their validity, we compared the structure tensor-based predictions of cell orientations with the ground-truth orientations of many manually segmented myocytes. To illustrate the angular changes, we employed

a 3-dimensional array of pivoting cylinders and streamlines, or "orientation glyphs," to visualize the parula-color-coded orientation field (Fig. 1B).

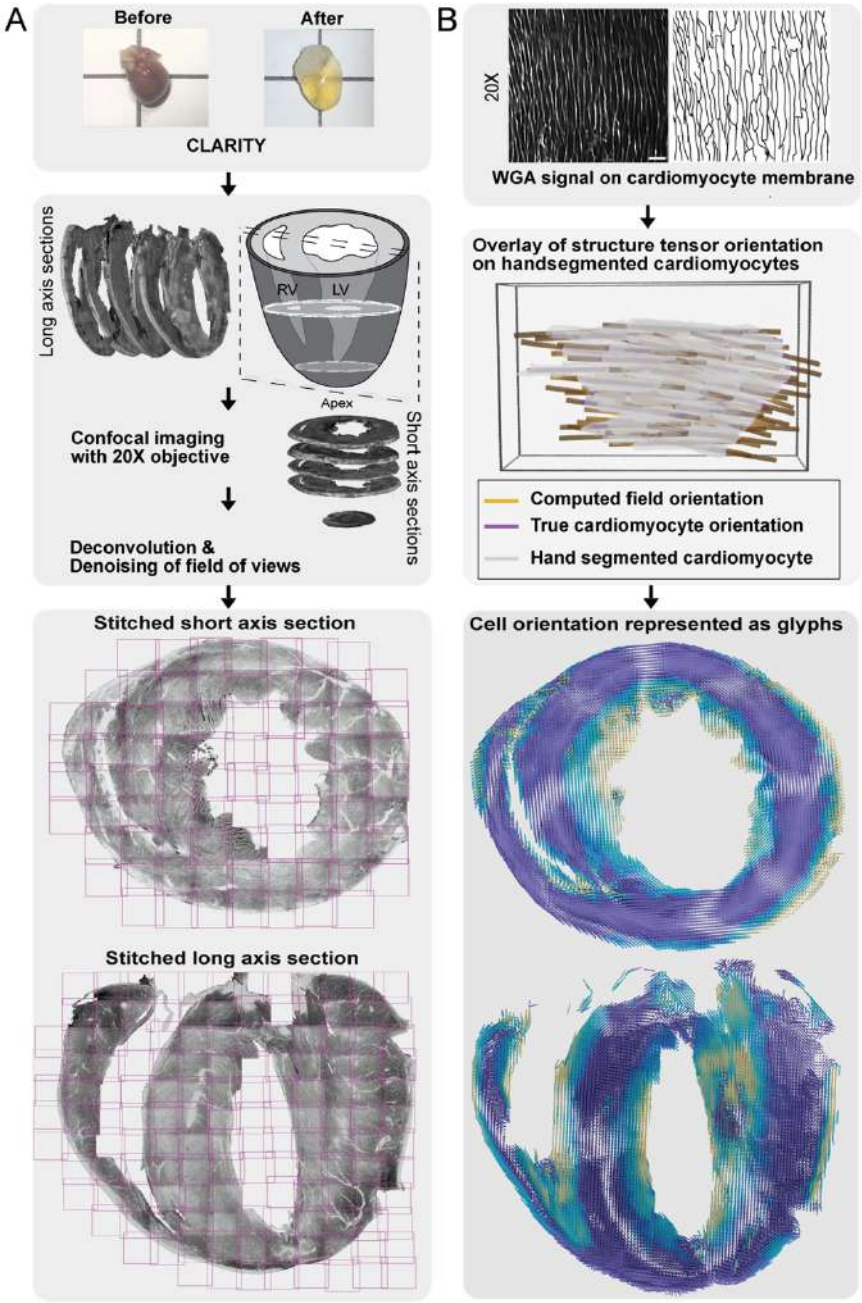

Synopsis Figure: Scheme for tissue preparation, imaging, and computational analysis. **A.** Flowchart illustrating the tissue preparation, imaging, and pre-processing pipeline. The top row depicts representative images for clearing (CLARITY) of the entire heart tissue. The middle row shows the tissue sections obtained in different orientations. The bottom panel shows the generation of a composite tiled image from the acquired field of views. **B.** A flowchart illustrating the computational pipeline for estimation and orientation reconstructions of myofibers. The top row shows the features of cardiomyocytes picked up by WGA staining intensity gradient with respect to the cell membrane. The middle row shows the orientation estimation from many hand-segmented cardiomyocytes, which is computationally estimated. This ground-truth

experiment validated the computational pipeline of the orientation estimation as an independent experiment. The bottom row shows the operations performed on the stitched composite image.

Chapter 4: Results and Conclusions

The heart pumps blood and functions because of the synchronized contraction of cardiomyocytes. A consensus model for myofiber geometry does not yet exist because of the limited spatial resolution of whole-heart imaging methods and the fragmented nature of histological studies. We provide the first three-dimensional reconstruction of myofibers across the entire mouse ventricular wall at micron-scale resolution. In the outer ventricular wall region, our micron-scale imaging analysis revealed prominent and distinct longitudinal myofiber bands orthogonal to the well-known circumferential bands in the middle wall.

Chapter 5: Limitations

Mouse ventricular heart regions were the primary subjects of this thesis. Conclusions on myocyte orientation in the atrial or basal ventricular areas or other muscle systems were not addressed in this thesis; hence, the details of myocyte orientation in the atrium, basal regions, or other muscle systems will not be included. This longitudinal outer wall system's functional role in regulating heart contractions is still up for question. Modeling biophysical characteristics and cellular variations between circumferential and longitudinal myofiber connections must be explored.

Chapter 6: Discussion

Our imaging revealed the presence of a fiber system similar to that in rat hearts. Similar fiber patterns have been reported in other organs and the entire animal body, indicating that this unusual longitudinal fiber geometry is not exclusive to the heart (20,21) .The smooth muscle peristaltic motions found in the esophagus and intestinal tubes are known to depend on the coexistence of circumferential and longitudinal fiber systems at the organ level(20). However, the orthogonal arrays in these layered muscle fiber structures occupy an equivalent volume, which is a significant distinction between them and the heart .

REFERENCES OF SYNOPSIS

1. Zipes DP, Libby P, Bonow RO, Mann DL, Tomaselli GF. Braunwald. Tratado de cardiología: Texto de medicina cardiovascular. Elsevier Health Sciences; 2019. 2425 p.

2. von Deuster C, Sammut E, Asner L, Nordsletten D, Lamata P, Stoeck CT, et al. Studying Dynamic Myofiber Aggregate Reorientation in Dilated Cardiomyopathy Using In Vivo Magnetic Resonance Diffusion Tensor Imaging. Circ Cardiovasc Imaging. 2016 Oct;9(10):e005018.

3. The Functional Anatomy of Ventricular Contraction | Circulation Research [Internet]. [cited 2022 Dec 19]. Available from: https://www.ahajournals.org/doi/abs/10.1161/01.res.1.2.162

4. Fiber architecture of the left ventricular wall: An asymptotic analysis - Peskin - 1989 - Communications on Pure and Applied Mathematics - Wiley Online Library [Internet]. [cited 2022 Dec 19]. Available from: https://onlinelibrary.wiley.com/doi/abs/10.1002/cpa.3160420106

5. Torrent-Guasp F, Buckberg GD, Clemente C, Cox JL, Coghlan HC, Gharib M. The Structure and Function of the Helical Heart and Its Buttress Wrapping. I. The Normal Macroscopic Structure of the Heart. Semin Thorac Cardiovasc Surg. 2001 Oct 1;13(4):301–19.

6. Savadjiev P, Strijkers GJ, Bakermans AJ, Piuze E, Zucker SW, Siddiqi K. Heart wall myofibers are arranged in minimal surfaces to optimize organ function. Proc Natl Acad Sci. 2012 Jun 12;109(24):9248–53.

7. Regional localisation of left ventricular sheet structure: integration with current models of cardiac fibre, sheet and band structure☆ | European Journal of Cardio-Thoracic Surgery | Oxford Academic [Internet]. [cited 2022 Dec 19]. Available from: https://academic.oup.com/ejcts/article/32/2/231/452588

8. Measuring and Mapping Cardiac Fiber and Laminar Architecture Using Diffusion Tensor MR Imaging - HELM - 2005 - Annals of the New York Academy of Sciences - Wiley Online Library [Internet]. [cited 2022 Dec 19]. Available from: https://nyaspubs.onlinelibrary.wiley.com/doi/full/10.1196/annals.1341.026?casa_token=mGZ4WwQO0UIAAAAA%3A3NrcFWgEg5MstIS9rTrYytf_uOPZsHFZTz-HcbDG22MvmAw-oxR-9xh_E7BEhRPnvcj6zJUJMTxofw

9. Geodesics as a mechanically optimal fiber geometry for the left ventricle. - Abstract - Europe PMC [Internet]. [cited 2022 Dec 19]. Available from: https://europepmc.org/article/med/8147836

10. A Novel Rule-Based Algorithm for Assigning Myocardial Fiber Orientation to Computational Heart Models | SpringerLink [Internet]. [cited 2022 Dec 19]. Available from: https://link.springer.com/article/10.1007/s10439-012-0593-5

11. A Computational Framework for the Statistical Analysis of Cardiac Diffusion Tensors: Application to a Small Database of Canine Hearts | IEEE Journals & Magazine | IEEE Xplore [Internet]. [cited 2022 Dec 19]. Available from: https://ieeexplore.ieee.org/abstract/document/4359061/

12. Lombaert H, Peyrat JM, Croisille P, Rapacchi S, Fanton L, Cheriet F, et al. Human Atlas of the Cardiac Fiber Architecture: Study on a Healthy Population. IEEE Trans Med Imaging. 2012 Jul;31(7):1436–47.

13. Conduction in the Heart Wall: Helicoidal Fibers Minimize Diffusion Bias | Scientific Reports [Internet]. [cited 2022 Dec 19]. Available from: https://www.nature.com/articles/s41598-018-25334-7

14. Seidel T, Edelmann JC, Sachse FB. Analyzing Remodeling of Cardiac Tissue: A Comprehensive Approach Based on Confocal Microscopy and 3D Reconstructions. Ann Biomed Eng. 2016 May 1;44(5):1436–48.

15. Free-of-Acrylamide SDS-based Tissue Clearing (FASTClear) for three dimensional visualization of myocardial tissue | Scientific Reports [Internet]. [cited 2022 Dec 19]. Available from: https://www.nature.com/articles/s41598-017-05406-w

16. Nehrhoff I, Ripoll J, Samaniego R, Desco M, Gómez-Gaviro MV. Looking inside the heart: a see-through view of the vascular tree. Biomed Opt Express. 2017 Jun 1;8(6):3110–8.

17. Anderson RH, Smerup M, Sanchez-Quintana D, Loukas M, Lunkenheimer PP. The three-dimensional arrangement of the myocytes in the ventricular walls. Clin Anat. 2009;22(1):64–76.

18. Young, Legrice, Young, Smaill. Extended confocal microscopy of myocardial laminae and collagen network. J Microsc. 1998 Nov;192(2):139–50.

19. Yang B, Treweek JB, Kulkarni RP, Deverman BE, Chen CK, Lubeck E, et al. Single-Cell Phenotyping within Transparent Intact Tissue through Whole-Body Clearing. Cell. 2014 Aug 14;158(4):945–58.

20. Diamant NE. Physiology of Esophageal Motor Function. Gastroenterol Clin North Am. 1989 Jun 1;18(2):179–94.

21. Mittal RK. Longitudinal muscle of the esophagus: its role in esophageal health and disease. Curr Opin Gastroenterol. 2013 Jul;29(4):421.

22. Orthogonal muscle fibres have different instructive roles in planarian regeneration | Nature [Internet]. [cited 2022 Dec 19]. Available from: https://www.nature.com/articles/nature24660

Table of Contents

ABSTRACT

This thesis presents a novel method for reconstructing three-dimensional myofiber orientation across entire mouse ventricular walls at the micrometer scale, significantly improving upon the limited spatial resolution of existing methods. This resolution improvement enables a comprehensive understanding of myofiber geometry and reveals a new fiber system, which has remained elusive due to the limitations of existing imaging techniques. The methodology combines tissue clearing (CLARITY), high-resolution confocal microscopy, and advanced computer vision techniques to reconstruct myofibers across entire mouse ventricular walls at the micron scale resolution. From the fluorescence signal at cardiomyocyte boundaries, this method extracts information where the intensity gradient provides unbiased estimates of the eigenvectors associated with the structure tensor. The resulting reconstructions reveal a complex geometry of myofibers, including prominent long-axis fibers that are orthogonal to the well-known circumferential ones. These findings corroborate previous studies that employed lower-resolution methods but provide unprecedented detail about the three-dimensional organization of myofibers. Moreover, our methodology led to the discovery of an additional cell layer in the outer ventricular wall, a significant finding that reshapes our understanding of heart wall structure. This cellular layer lies in a thin shell and forms a continuum with longitudinally arranged cardiomyocytes in the inner walls, with a complex geometry at the apex. The findings from this study pave the way for the investigation of myofiber remodeling in heart diseases, providing a valuable tool for elucidating the mechanisms underlying cardiac dysfunction associated with structural changes. By unraveling the intricate organization of myofibers, this work has significant implications for our understanding of heart function and cardiac diseases.

CHAPTER-1
INTRODUCTION

1.1 Origin of the heart as an organ

The heart is an organ that starts beating from a very early embryonic stage and continues to function by pumping oxygen-containing fluid/blood to different parts of the body throughout its lifetime (1,2). The architecture of the heart varies across different classes of vertebrates without compromising its fundamental function, that is pumping fluids/blood (1). In this study, I aim to study the organization of heart organ at cellular scale.

An interesting aspect of heart evolution is that the earliest known hearts were not used for pumping blood, but instead for pumping fluid through the circulatory systems of simple invertebrates such as worms and jellyfish (1). The invertebrate hearts are simple contractile structures composed of muscle cells that can create fluid flow through the organism, shaped as a linear tube with a single cell layer and pulsatile contractility. However, they are limited by undefined chambers or valves, enabling an open circulatory system (3). Blood vessels and vasculature architecture developed as animals become more complex and begin to move around. With the increased complexity of the whole body of organism, hearts have also started to evolve to pump blood around the organism. The advanced versions of heart in the evolutionary tree resulted in compartmentalization of the heart into two or three or four chambers. The four-chambered heart separates oxygen-rich and oxygen-poor blood, making the circulatory system more efficient in delivering oxygen to the body's tissues.

Heart-like musculature can be found in a variety of different organisms (3), including:

- Many invertebrates, such as worms and jellyfish, have simple contractile structures that perform the functions of a heart, pumping fluid through their circulatory systems.
- Fish have a two-chambered heart consisting of an atrium and a ventricle, with more peristaltic capacity to control in and out flow of fluids pumping blood to the gills and the rest of the body.
- Amphibians also have a two-chambered heart, but their heart is more advanced than fish, allowing for more efficient blood oxygenation.
- Birds and mammals have a four-chambered heart, which allows the separation of oxygen-rich and oxygen-poor blood, making their circulatory system more efficient in delivering oxygen to the body's tissues.

1.2 Anatomy of mammalian heart

Anatomically mammalian heart is divided into right-left parts and contain two ventricles and atriums each side separated by a septal wall (4). In addition to the chambers, tricuspid, pulmonary, mitral, and aortic valves control a unidirectional flow path for the blood and prevent backflow. Deoxygenated blood from the body is taken in by the right atrium and pumped to the right ventricle, which ultimately transfers it to the lungs for reoxygenation (Figure 1). The oxygenated blood is drawn from the lungs and channeled to the left ventricle by the left atrium, which is then pumped it to the rest of the body. The arteries, veins, and capillaries in heart aid in controlling the activity of blood flow and enable effective blood pumping (Figure 1). The network of coronary arteries provides the vital nutrition required for myocardial function by supplying oxygen-rich nutrients along the perimeter.

The American Heart Association (AHA) classification system for the anatomy of the human heart is a thorough and in-depth method for describing cardiac structures based on their position in the left ventricle at the mesoscale (mm scale) (5). The three categories of AHA classification system for the anatomy of the heart are basal, mid-ventricular (Parasternal short axis- papillary muscle (PSAX-PML) and Horizontal long axis-4 chamber (HLA-4C) regions, and apical (5). For having a consensus localization of the region of the heart across different acquired datasets and to link it to the data bank in future, we have adapted the AHA terminology. The right and left ventricular outflow tracts, right and left atrioventricular (AV) valves, and right and left papillary muscles make up the basal region. The ventricular septum and coronal components are part of the mid-ventricular region as shown in Figure 2. The chordae tendineae, papillary muscles, and the mitral and tricuspid valves are all found in the apical region. Each side of the heart is divided into four divisions by the AHA system: anterior, septal, inferior, and posterior walls. Each wall can then be further divided into three segments; apical, mid-ventricular and basal which are further subdivided into six or seven small parts known as subsegments. This segmentation allows clinicians to accurately localize heart tissue and diagnose any potential issues quickly and efficiently.

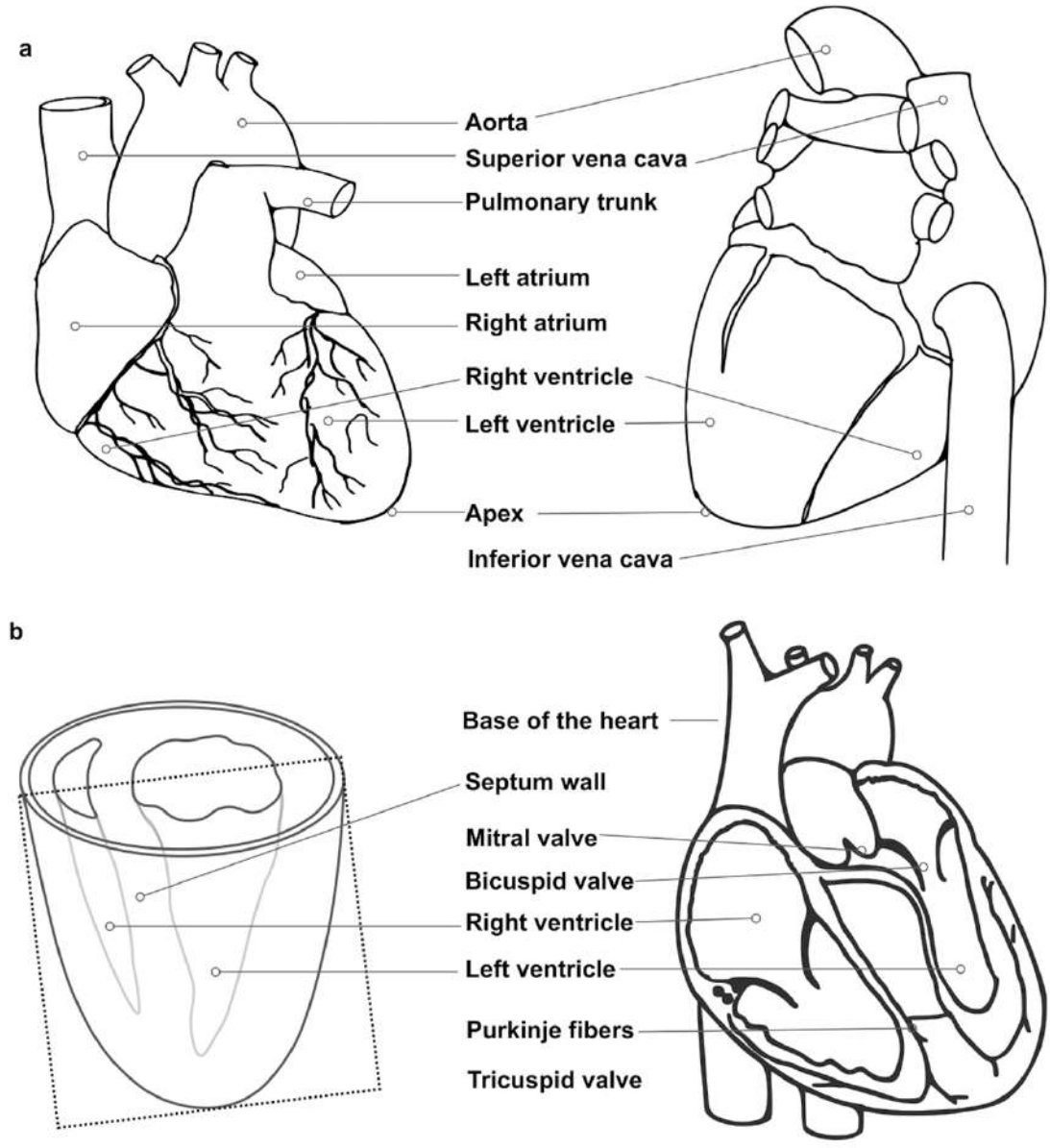

Figure 1. Graphical representation of anatomical features for mammalian heart.
a. Overview of the coronary arteries and cardiac veins – anterior and posterior views.
b. ventricular chambers (left) and valves (right) that controls blood flow in heart.

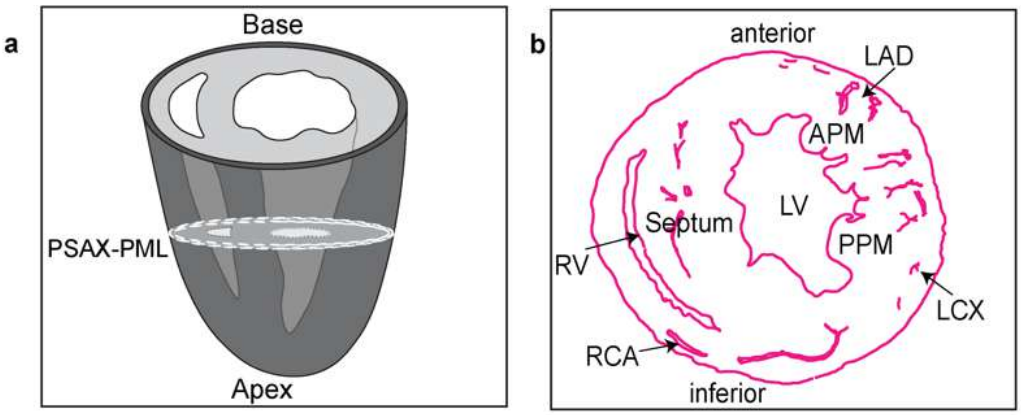

Figure 2: Reference for heart sections.
Midventricular short axis section is referred to PSAX-PML. B. Major papillary muscle and blood vessel locations w.r.t short axis sections are marked. PPM-Papillary Muscle, LAD- left anterior descending, LCX- left circumflex artery, RCX- right circumflex artery, RCA- right coronary artery, RV-Right ventricle, LV- Left ventricle.

1.3 Cardiomyocytes and other cells of the heart

The heart is made up of numerous types of cells that cooperate to maintain its physiology and morphology. Every type of cell is essential to the heart's ability to pump oxygen-rich blood throughout our bodies. Cardiomyocytes (CM), endothelial cells (EC), smooth muscle cells (SMC), and fibroblasts (FB) are the four main cell types of the heart (Figure 3) (6). Endothelial cells cover every interior surface of vessels like arteries and veins; these specialized epithelial layers serve as a barrier between the blood that circulates and the tissues around it (7). They also aid in controlling local vascular tone by secreting hormones or other molecules into the bloodstream when necessary for homeostatic control. The smooth muscle cells that make up the walls of bigger vessels, such arteries, differ from cardiomyocytes because they lack ordered contractile protein machineries (7). Human studies have shown that the adult heart ventricles approximately contain 49.2% ventricular cardiomyocytes, 21.2% mural cells (pericytes and SMCs), 15.5% FBs, 7.8% Ecs and 5.3% immune cells (myeloid and lymphoid) (6).

Cardiomyocytes are elongated cells with pseudo-cylindrical structure shapes (8). There have been many studies on understanding the 3D geometry of cells based on isolated cardiomyocytes from left ventricular walls (9–11). These cells are adhered to each other by gap junction proteins, desmosomes and adhesins via both end-to-end and lateral connections (12). Most of the myocardium, or muscular layer, in heart, is made up of cardiomyocytes. Cardiomyocytes are aligned end-on-end in their long axis direction to form myofibers (13). During each heartbeat cycle the cardiomyocytes are stimulated

rhythmically to contract and relax, which combinedly generates enough force to pump the blood throughout our bodies. They have contractile protein assemblies called ‘sarcomeres’ that enable heart contraction (14). Sarcomeres are arranged repeatedly along the length of the muscle fibers. Each sarcomere consists of two types of thick and thin filaments, composed of myosin and actin proteins respectively. When a muscle is stimulated to contract, the thick, thin fibers contract around each other, shortening the sarcomere and causing the muscle fibers to contract Sarcomeres are highly organized structures, each feeding specific role in attraction. The thick filaments are arranged at the center of the sarcomere, while the thin filaments are arranged around the periphery. The thin filaments are anchored by two structures called Z-discs at the end of the sarcomere. The shortening of the sarcomeres aids the contraction of the muscle fibers.
The membrane invaginations of cardiomyocytes are called as T-tubules and they coordinate in ion transport mediated via Ryanodine Receptors (RyR) receptors (15). Cardiomyocytes are subdivided further to Purkinje cardiomyocytes and working cardiomyocytes based on their difference in function and molecular expressions (16,17). Purkinje cardiomyocytes have a role in faster conduction of electrical signal with their high number of connexin gap junctional connections (18). The working cardiomyocytes on the other hand has more role in contraction with a very defined t-tubular arrangements along with the sarcomere patterning (10). Malformations of myofibers can lead to pathological conditions of the heart, including cardiomyopathies, myocardial infarction and disorders related to electrical conduction (19–21)

1.4 Mechanism of muscle contraction in heart

An electrical signal known as an action potential causes the cardiac muscle fibres to contract and spreads throughout the heart muscle to start the heartbeat (22–24) . The following sequence of events can be used to describe action potentials during heart contraction (25):

1. In the sinoatrial (SA) node, which is found in the right atrium of the heart, pacemaker cells produce an action potential. The atria constrict as the signal travels through them.
2. Following that, the action potential travels to the atrioventricular (AV) node, which is situated at the intersection of the atria and ventricles. Now that the signal has been delayed, the atria can fully contract and dump their contents into the ventricles.

3. After there, the signal travels through the bundle of His and enters the Purkinje fibers, specialised conducting fibers that run throughout the ventricles.
4. The ventricular muscle fibers contract simultaneously as the action potential passes quickly through them via gap junctions.
5. The release of calcium ions from the sarcoplasmic reticulum is caused by the action potential when it passes through the ventricular muscle fibers and activates the calcium channels in the T-tubules.
6. Muscle contraction starts when the calcium ions interact with the troponin complex and myosin heads are able to bind to actin filaments.

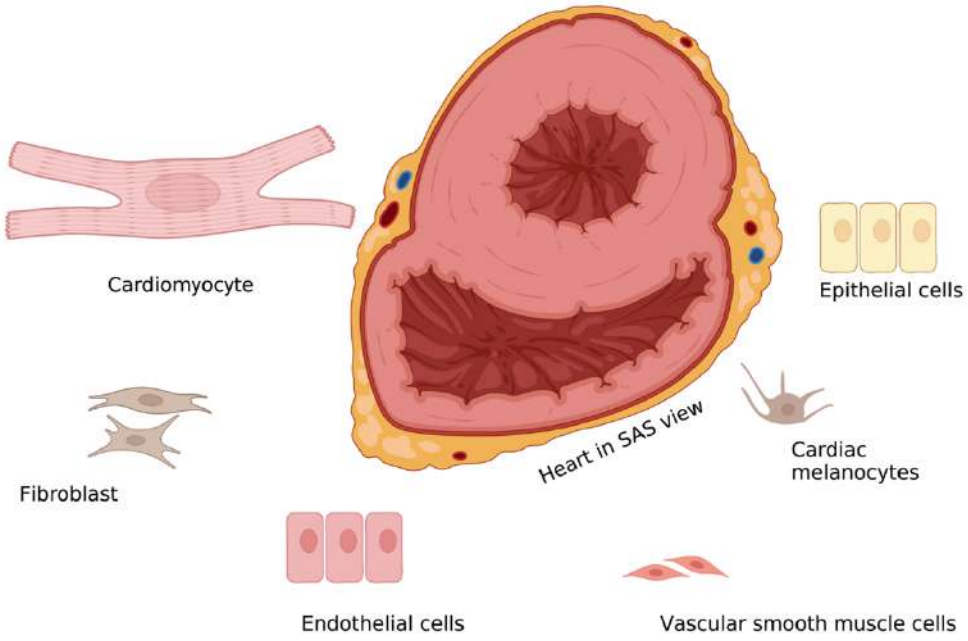

Figure 3: Graphical representation of various types of cells in heart. Heart contains Cardiomyocytes, epithelial cells, fibroblasts, endothelial cells, cardiac melanocytes and vascular smooth muscle cells (Created with BioRender.com.)

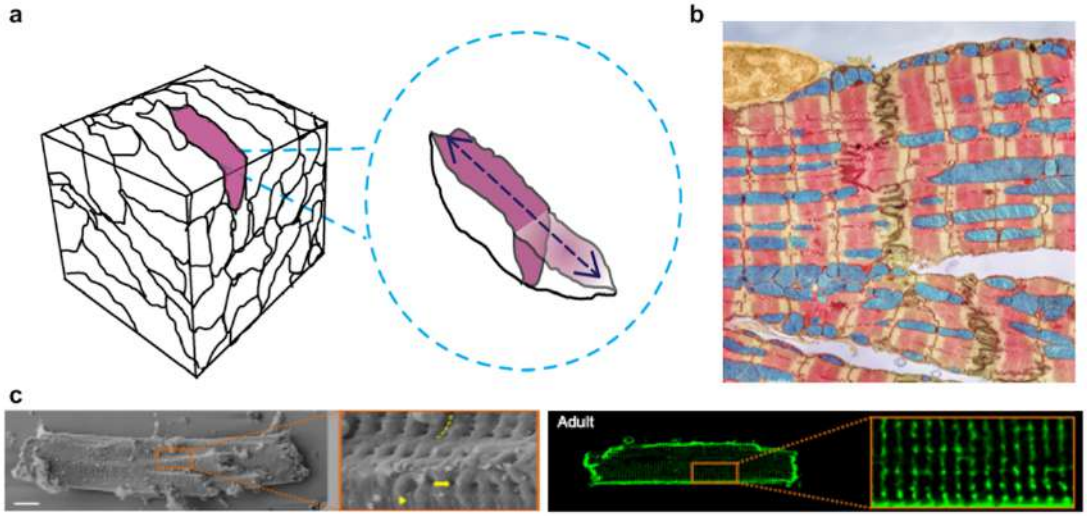

Figure 4: Representation of cardiomyocyte morphology from a stack of cells
Representation of cardiomyocyte morphology from a stack of cells. **a.** Graphical representation of a volume of tissue section; a typical cardiomyocyte cross-sectional geometry is shown side by side. **b.** Pseudo colored TEM image of heart tissue highlighting sarcomere band (pink) mitochondria (blue) and intercalated disk region (brown) (Courtesy: Science photo library) **c.** Topology of an isolated adult rat ventricular cardiomyocyte SEM image(grey) and stained with WGA (green) (Adapted from-Lipsett et al., 2019)

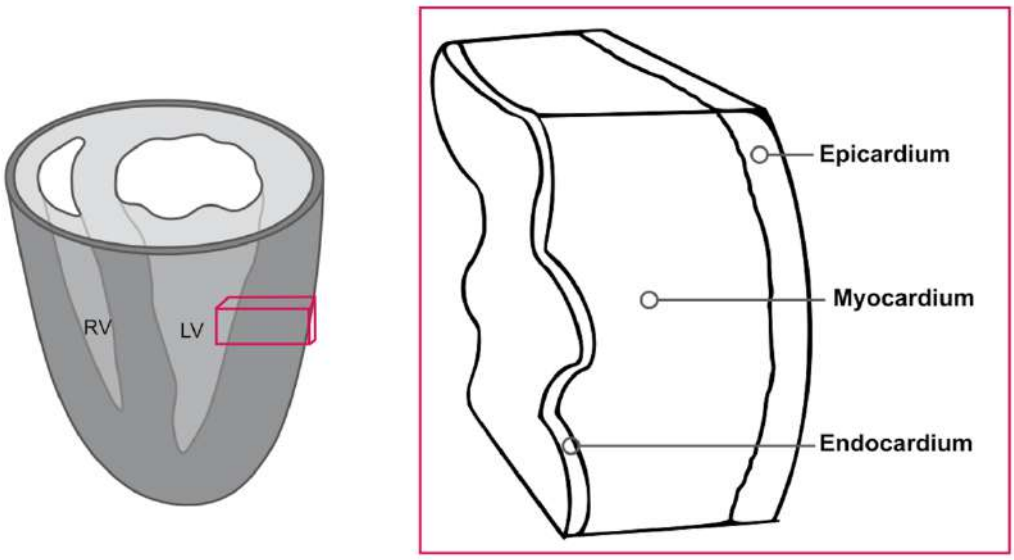

Figure 5: Graphical representation of heart wall- three-layer system.
Ventricular heart wall consists of outer-epicardium, middle- myocardium and inner-endocardium layers. The geometry of the heart wall is designed to maximize its pumping efficiency. The heart's chambers and valves are specifically shaped to allow blood to flow in one direction and to prevent backflow. In contrast, the walls of the chambers and blood vessels are thickened and strengthened in the areas that experience the most pressure and stress.

1.6 Models of myofibril arrangement

At a gross level, the myofiber organization in the heart has been described as a helical continuum that wraps around the heart walls (29,30). Several competing models that detail myofiber organization in the heart wall have been described (28–30). The current geometric descriptions include the nested toroid and pretzel models, the helical and ventricular myocardial band (HVMB) model, the simple myolaminae model and the three-layered myocardium model (28). The nested toroid and pretzel models propose that myofiber orientation varies throughout the myocardium, twisting and wrapping around different ventricular regions (28). The HVMB model suggests that the myofibers surrounding the heart chambers can be unwrapped into a single helical band (28). In the simple myolaminae model, the myofibers are stacked in sheets intercalated with connective tissue comprised of collagen.

Several of the above models have been derived from diffusion-tensor magnetic resonance imaging (DT-MRI), where the local orientation of myofibers is associated with the dominant direction of water diffusion at a millimeter scale (31). A second moment matrix that records the distribution of a gradient locally can utilize its eigenvectors and eigenvalues to estimate orientation by computing the structure tensors in DT-MRI, which employs diffusion of water molecules as a proxy for orientation (32). The helix angle between this local dominant orientation and the long axis direction has been widely used to characterize fiber geometry and build atlases of myofibers spanning the entire heart. Along these lines, Savadjiev et al. have demonstrated that the volumetric geometry throughout the ventricular heart wall is characterized by a generalized helicoid, with a degree of transmural rotation that is conserved across different four-chambered hearts (30). This helicoidal geometry minimizes potentially harmful stochastic biases in the wave conduction as it propagates in the heart wall(30). It also supports findings that this conduction is faster along the long-axis direction of myofibers than across the heart walls.

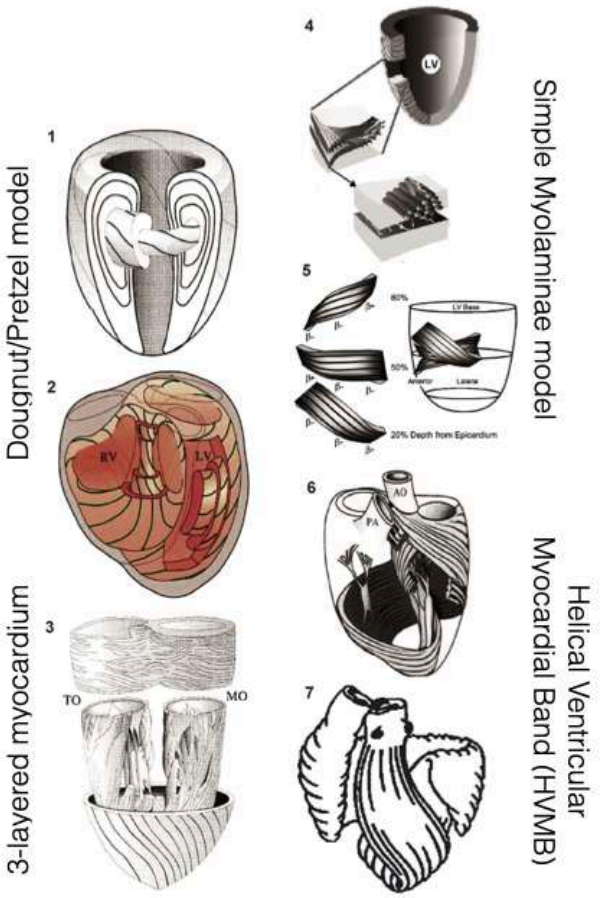

Figure 6: Prevailing heart wall models.
1,2. Doughnut/Pretzel model. 3. 3-Layered myocardium. 4,5. Simple myolaminae model. 6,7. Helical Ventricular myocardial Band. Reference:(28)

While there is progress in modeling myofiber geometry through diffusion imaging, analyses based on DT-MRI suffer from severe limitations in spatial resolution. A typical DT-MRI based reconstruction is at the scale of about a millimeter to one-third of a millimeter in dimension (32), at which several hundred cardiomyocytes can be placed in each voxel. Recovering myofiber geometry at the scale of individual cardiomyocytes is only possible using higher-resolution light microscopy.

1.7 Development of murine heart

The cardiac progenitor cells form the four heart chambers, as well as other vital components like valves and arteries, during the development of the murine heart (33). These cells go through several complex processes to develop into mature cardiomyocytes, or heart muscle cells. Mesoderm induction marks the start of heart development at embryonic day E7.5, while looping morphogenesis marks its conclusion

at E10.5 in mouse (34). Throughout this time, many different factors interact to ensure optimal growth and function.

Mesoderm induction, the first stage of murine heart development, is triggered by signals from neighboring tissues and results in the differentiation of some precursor cells into cardiac progenitors that express particular markers involved in the formation of the cardiovascular system (33,34). From here, these precursors multiply quickly while further differentiating into specific cell types, such as endocardial cushion tissue (ECT) or myocardium (MC) (34). To promote communication between these various cell types at later phases of maturation, other components such as extracellular matrix proteins (ECM) and cytokines produced by nearby tissues must also be present (34).

Finally, looping morphogenesis occurs when ECT forms spindle-shaped structures around MCs called trabeculae carneae; later, these two components interact via ECM molecules to let them move relative to one another, eventually forming loops within ventricles and atria walls, giving rise to the four-chamber structure seen in adult hearts today (34). Proliferation, migration, apoptosis, adhesion remodeling, and other cellular processes must be precisely coordinated during this period. These processes are all controlled by biochemical signaling pathways that involve several hormones, receptors, enzymes, and other molecules. Successful completion ultimately yields a fully working organ capable of effectively pumping blood throughout the body.

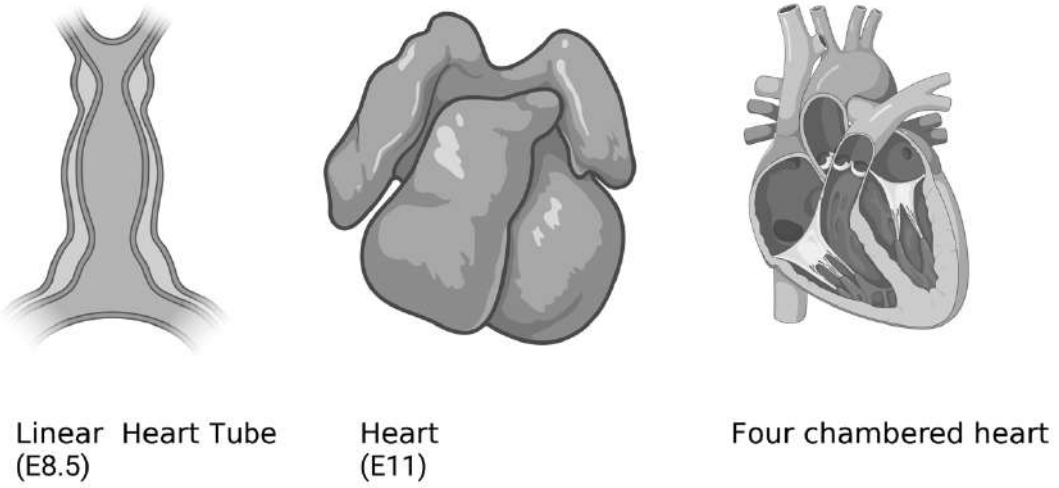

Figure 7: Graphical representations for development of murine heart.
In mouse, a linear heart tube at E8.5 can undergo multiple looping events resulting a looped heart at E11. The four chambered heart is formed post septation event. (Created with BioRender.com.)

1.11 Heart diseases and the importance of conserved myofiber organization

Heart diseases can arise from numerous reasons starting from inherited genetic mutations, developmental disorders and even based on lifestyle conditions. Defects at any stage of development like looping, or morphogenesis, or electrical conduction system, or signaling molecules can give rise to many congenital or late onset cardiac diseases. Cardiomyopathies are diseases related to heart muscle deformities (35). Hypertrophic cardiomyopathy (HCM) is associated with the thickening of the heart muscle, most commonly at the septum between the ventricles below the aortic valve. The current prevalence of HCM is 1:500 (36) . HCM is characterized by left ventricular hypertrophy unexplained by secondary causes and a nondilated left ventricle with preserved or increased ejection fraction. The structural changes associated with HCM are commonly asymmetrical with a Left ventricular outflow tract obstruction in one third of patients. Myocyte hypertrophy and disarray, as well as interstitial fibrosis are typical histological observations of HCM heart biopsies. Genes encoding sarcomere-associated proteins like MYH7 and MYBPC3, encoding β-myosin heavy chain and myosin-binding protein C, respectively, are the two most common genes involved in causing HCM (37). Dilated cardiomyopathy (DCM) is the most common type of heart disease, occurring primarily in adults aged 20 to 60, where the heart's left ventricle becomes dilated (38,39). Majority of DCM are originated due to idiopathic etiology or myocardial insults (38). Generally, there will be a progressive dilation of ventricles leading to tricuspid/mitral valve insufficiency and geometric remodeling of the ventricles during DCM (39). Nonspecific changes of fibrosis and hypertrophy is observed during histological examination of DCM hearts (39).

Genetic mutations affecting genes encoding cytoskeletal proteins, proteins involved in contraction and the nuclear lamins A and C cause DCM (38,40,41). Myocardial infarction (MI) occurs when blood flow decreases or stops in a part of the heart, causing damage to the heart muscle (42). Understanding the myofiber organization will help us address the different heart muscle pathologies, including but not limited to cardiomyopathies.

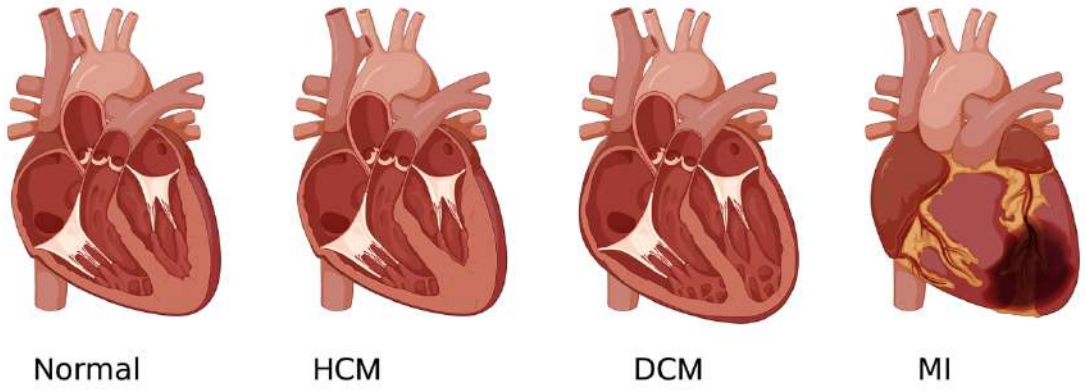

Figure 8: Graphical representations for diseased states of heart.
HCM- Hypertrophic cardiomyopathy. DCM- Dilated cardiomyopathy. MI- Myocardial Infarction. (Created with BioRender.com.)

1.11 High-resolution light microscopy studies of heart tissue

Recovering myofiber geometry at the scale of individual cardiomyocytes is only possible using higher-resolution light microscopy. Studies in this direction have focused on small sections of heart tissue (43,44), 3D stacks of heart tissue to image blood vessels (45), or light sheet microscopy using auto-fluorescence (46). These attempts to image heart tissue samples have neither recovered myofiber nor cardiomyocyte orientation. Similarly, studies based on histology have not always catalogued the region of the heart under investigation in a systematic way, and are often been limited to two-dimensional samples (47,48). Thus, inferring myofiber geometry across the full extent of the heart wall from histological analyses remains challenging.

Other high-resolution imaging methods, such as synchrotron radiation imaging of rat hearts at 3 μm voxel resolution, have revealed ultrastructural properties of heart tissue, including its cellular and extracellular features (49). However, due to a lack of cellular boundary information in such images, the geometric arrangements of cardiomyocytes cannot easily be recovered.

1.10 Challenges of 3D-imaging at micron scale resolution

Imaging biological samples in 3D at the micron scale is hard because of the physical limitations of the samples themselves. Biological tissues do not let visible light pass through, which is used in traditional microscopy techniques, making some parts of the sample impossible to image. The inherent property of biological samples with non-

uniform refractive indexes causes lot of scattering of light in the deeper layers and cause degraded image quality at depth along with pigmentation (50).

In addition to this, there are possibilities of spherical aberrations caused by the lens. Moreover, there is also a trade-off between resolution level and tissue penetration depth because higher resolutions typically call for more intense illumination intensities that are impacted by scattering effects from deeper depths within tissue structures. This is another barrier to resolution capabilities despite the fact that modern technologies enable to access deeper layers than ever before. Finally, problems with data analysis arise up as well; because each layer has properties that are different, appropriately determining the cellular orientations from all three dimensions requires sophisticated algorithms that can precisely distinguish between various cell types found in an image.

1.11 Requirements for 3D-imaging biological tissue samples

Due to their natural opacity, biological tissues can be challenging to image deeply in 3D, especially complex tissues like the heart. A common approach is to combine traditional histological sectioning with computational 3D reconstruction. However, this approach has limitations, such as tissue distortion, destruction of cell connections, and low spatial resolution. Modern fluorescent microscopy platforms, such as confocal scanning microscopy, have high spatial resolution but limited penetration depth due to tissue opaqueness.

The recent advancements in tissue clearing method have opened the door for more possibilities of 3D imaging with better light penetration into deeper parts of the tissue. It enables efficient fluorescent labeling and rapid 3D volumetric imaging of intact tissues and organs (50,51). By making tissues transparent, tissue clearing reduces attenuation of light by the tissue sample, allowing deeper imaging. These techniques involve the removal of light-scattering and light-absorbing components from the tissue, as well as equalizing the refractive index between the tissue and the imaging medium (52). Each of tissue clearing methods available have its own advantages and disadvantages. The best method to use will depend on the specific tissue and the desired imaging results.

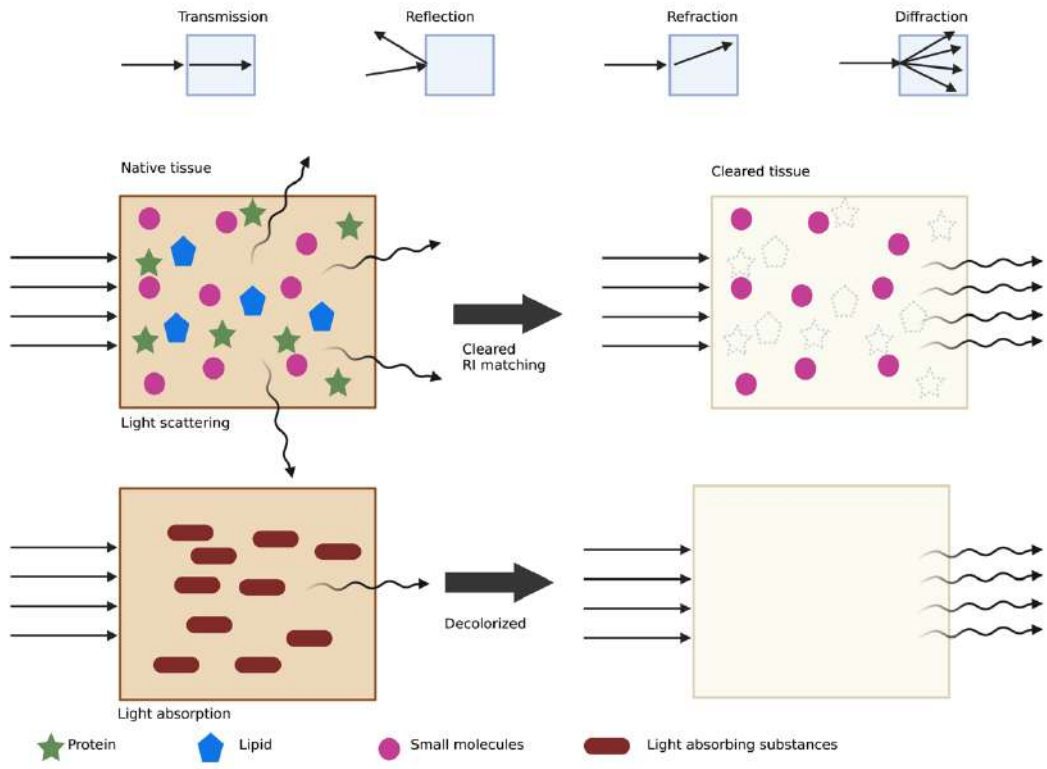

Figure 9: Graphical representation for matter interaction with light before and after clearing.
The two main factors that contribute to tissue opacity, which prevents light from propagating, are light scattering and light absorption. Heterogeneous components, such lipids and proteins scatter light and endogenous light-absorbing substances like melanin and haemoglobin absorbs light. Utilizing the tissue clearing process, tissue is made optically transparent by reducing light scattering and light absorption. (adapted from (50)) (Created with BioRender.com.)

Tissue clearing methods are principally divided into three categories:

1.Solvent-based methods:

Solvent clearing uses organic solvents to make tissues transparent quickly. One example is the 3D imaging of solvent-cleared organs (3DISCO) method, which can clear a whole mouse brain in two days (53). However, 3DISCO pretreatment can damage or remove epitopes for antibody staining.

2.Aqueous-based methods:

Aqueous-based clearing is more biocompatible and biosafe than solvent based clearing, but it does not clear tissues as well (54). During aqueous-based clearing, hydrogen bonds form between the clearing reagents and tissue components, which protects the structure of specimens and fluorescent proteins. CUBIC is a typical hydrophilic clearing method (55). It has been used to clear and image 3D structures with immunohistochemistry in adult mouse brains, hearts, lungs, stomachs, and intestines.

3.Hydrogel-based methods:

The most common hydrogel-based clearing method is called CLARITY (56–58). CLARITY forms hydrogels by covalent links, which uniformly removes lipids with fewer structural damages and biomolecular losses (59). This method preserves the tissue protein-architecture and removes lipid molecules the major contributor to optical hindrance with minimal tissue damage. However, CLARITY passive clearing is time-consuming compared to other methods.

Heart tissue is challenging to clear because it is rich in densely packed cells and connective tissues. Goodyer et al. (2019) used the iDISCO tissue clearing method to reconstruct the conduction system of the mouse heart (60). However, iDISCO poorly preserves GFP fluorescence. Heart clearing by CUBIC method can enhance the transparency of heart tissue and remove autofluorescence, allowing for detailed observation and imaging of the entire organ (51,55). CLARITY is a powerful tool for studying heart tissue aswell. It has many advantages over other tissue clearing methods, including excellent structural preservation, non-corrosive nature of reagents used, compatibility with immunostaining, the ability to clear large samples, and relative ease of use.

To reduce autofluorescence background, the heart must first be perfused to remove blood. Then, heart tissue can be cleared using a tissue clearing followed by fluorescence labelling and volumetric imaging.

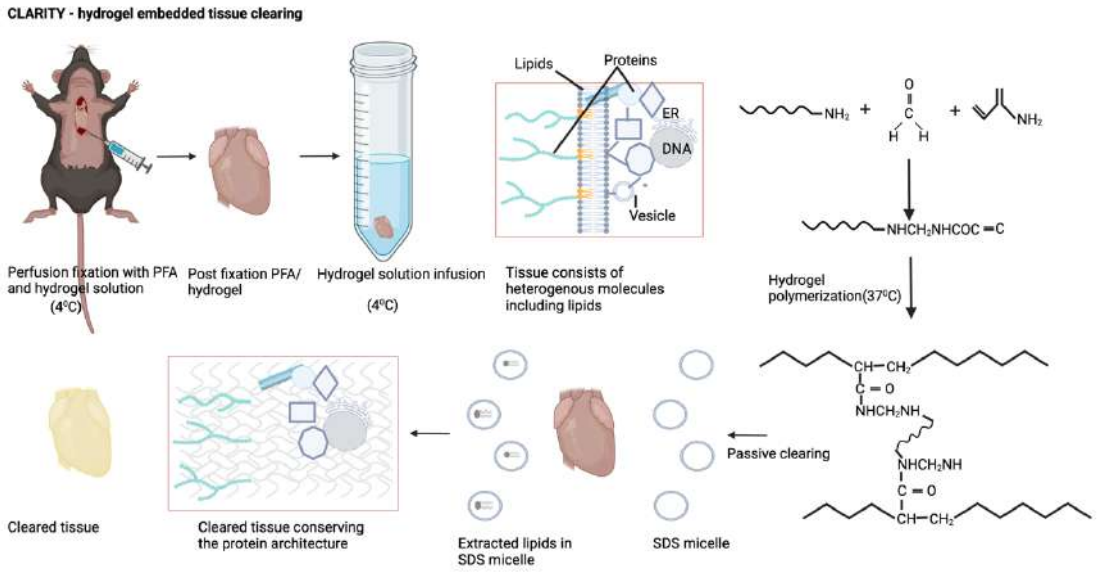

Figure 10: Graphical representation for CLARITY pipeline and chemistry behind the protocol.

Procedures of CLARITY: Covalent bonds between the natural molecules and the monomers are created when tissues are treated with formaldehyde and acrylamide. Then, with thermal initiation, acrylamide monomers polymerize to form a nanoporous hydrogel mesh. Tissue lipids are removed using an SDS detergent containing buffer with light shaking at 37°C. Biomolecules and tissue structure are still present. Different labels may be stained on cleared tissues. Labeled tissues are incubated in RI-matching solutions to achieve homogeneity. Tissues of interest become optically transparent and enable examination with microscopes. (Adapted from (57); Created with BioRender.com.)

1.12 Structure tensors for orientation estimation

Structure tensor is a mathematical tool used to analyse the local structure of an image. It represents an image's distribution of intensity gradients and it is used to identify edges and corners (61). An intensity gradient is a measure of how the intensity of an image changes over a small distance. It is calculated by taking the derivative of the intensity function at each point in the image.

The structure tensor is calculated by taking the outer product of the gradient vector at each point in the image. The outer product is a matrix formed by taking the product of each element of the gradient vector with itself. The structure tensor encodes the relationships between an image's gradient directions and magnitudes. The dominant orientation of the image at each point can be calculated by taking the eigenvectors of the structure tensor. The eigenvectors are vectors that produce a scaled version of themselves when multiplied by the structure tensor. The eigenvectors of the structure tensor correspond to the directions in which the intensity gradients are most pronounced. By identifying the dominant orientations of the intensity gradients in an image, the structure tensor can be used to identify edges and corners.

In DT-MRI (diffusion tensor magnetic resonance imaging), the diffusion of water molecules is measured to understand the underlying tissue orientation (32). The biological tissue can create the anisotropic diffusion of water molecules wherever heterogeneity occurs. For example, in the white matter of the brain, diffusion anisotropy is primarily caused by cellular membranes in addition to the minor contribution of myelination and the packing of the axons (32).

Our goal is to estimate the large-scale orientation of the myocytes over the entire intact, thick sections of a mouse heart using computer vision techniques. To estimate the orientation at each voxel, one can calculate the structure tensor of the intensity image data. Eigenvector decomposition of the estimated structure tensors can then be used to estimate the local orientation of cardiomyocytes. To get a visual understanding of the

structure tensor, it is useful to use an ellipsoid. Figure 11 (left) shows that an isotropic ellipsoid (a sphere) represents a tensor with no preferential orientation. Such a tensor indicates a region with almost constant intensity. In a region where the intensity varies along one dominant direction, the tensor may be represented in Figure 11 (middle). In contrast, a region with an intensity that varies in a plane but is constant along the third axis may be represented as a plate-like tensor, as in Figure 11 (right). Recovering cardiomyocyte geometry at the cellular scale is of fundamental interest, given the role this organization plays in driving heart wall electrical conduction and mechanics. Our method combining confocal microscopy with computer vision techniques allow micrometer-scale reconstruction of cardiomyocyte orientation

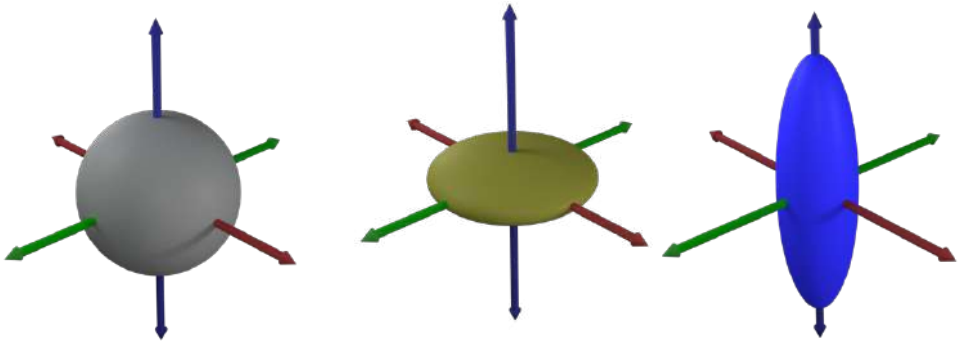

Figure 11: Graphical representation for different structure tensors.
Left: an isotropic tensor (no preferred local orientation). Middle: a plate-like structure (this could occur at a branching or crossing region. Right: an elongated tensor (the preferred orientation is in the direction of elongation).

CHAPTER – 2
OBJECTIVES

To comprehend the functioning of the heart, characterization of cellular features is necessary from whole heart imaging. However, the current high-resolution imaging of heart samples is either focused on cellular or subcellular architecture spanning an area of submillimeter size, and the volumetric information of cellular arrangement with respect to whole heart organ is lacking. On the other hand, the volumetric imaging of heart using DT-MRI or micro-CT and echocardiograms yield low-resolution models that cannot infer cardiomyocyte arrangement. Recent development in optical imaging techniques and chemical tissue clearing allows volumetric imaging, however automated methods for their quantitative analysis and visualization in 3D are still absent.

This gap in our understanding of the heart's 3D cellular architecture limits our ability to study the mechanisms of heart disease and develop new treatments. The micron-scale inspection of mammalian heart can answer many of the open questions in the field as noted below:

1. How are cardiomyocytes organized across heart walls?
2. Can we identify myofibril organization principle from high resolution imaging studies?
3. What alteration in the myofibril organization can cause diseased state of heart?
or can a diseased state of heart develop myofibril arrangement alterations?

The contraction of cardiomyocytes is caused by the active sarcomere units stretching along the thin and thick filament structures aligned in the long axis direction of the cell. This means that the cellular orientation can control the muscle stretching direction. Recent advances in DT-MRI and mathematical modelling have led to the proposal that myofibrils follow a generalized helicoid geometry. In this study, we use fluorescence imaging of intact cardiac tissues to investigate the micron-scale architecture of the cardiomyocyte and myofibril. This will help us to understand the basis of the helicoidal geometry observed in low-resolution imaging methods if any and may lead to new insights into the development of heart disease.

Primary Objective:

The primary objective of this thesis is to elucidate the 3D architecture of cardiomyocyte orientation from an intact ventricular heart tissue at a micron scale resolution. The output from this work will enable us to put forward a blueprint for the cellular architecture i.e., cardiomyocyte arrangement across normal or physiologically

functioning heart wall. This can be applied to understand the modifications in cardiomyocyte orientation induced by diseased states such as cardiomyopathies.

Specific objectives:

The specific objectives of this study are detailed below.

1. Establish a pipeline for tissue preparation and deep imaging using confocal microscopy.

To extract the cardiomyocyte arrangements across heart tissue, first I aim to establish tissue preparation and imaging methods. Here I will adopt the CLARITY protocol for optical clearing of the heart specimens that will enable deep tissue imaging. Post-clearing, I will optimize the fluorescent dyes and stains for imaging the cardiomyocytes from intact heart tissue. Next, I plan to use confocal microscopy, which is easily accessible and amenable for deep and wide tissue imaging of cleared hearts. By analyzing the cell membrane distribution based on the acquisition of fluorescence data from using the mouse heart as a model, we aim to infer and define the underlying structural network of cardiomyocytes in unprecedented depth.

2. Integrative approaches for deep tissue image analysis and estimation of myofiber orientation.

In order to computationally extract spatial and cellular information from large-scale fluorescence microscopy imaging data sets, we will establish a computational pipeline. The acquired 3D volumetric datasets can be improved with the use of deconvolution and denoising algorithms. By employing the direct methods for fiber orientation mapping based on the intensity gradient or the second-order derivative information, we will virtualize the pre-processed data and the obtained field data representation. The estimated cardiomyocyte orientations will be analyzed and plotted using standard angular definitions used in defining heart myofiber geometry.

3. 3D reconstruction of myofiber orientation using tractography at cellular/micron scale.

In this project, we will adapt a visualization method inspired by work in the DT-MRI field to produce whole-ventricular heart reconstructions of global and regional orientation of cardiomyocytes with high-resolution information. This technique creates 3D tractographic representations that allows for quick, multiscale analysis and visualization of vast volumes of complex biological data, which could otherwise be

challenging to decode and display. This is done due to the intrinsic capabilities of tensors to characterize and identify various structural information.

We believe that this approach, when implemented on the large-scale datasets currently available, may reveal previously unseen findings at many levels of the biological scale. It could also be seamlessly applied to other organ data types with cellular details.

CHAPTER - 3

MATERIALS AND METHODS

3.1 Animal model and ethical statement

The animal preparation and image work were conducted at the NCBS/inStem Animal Care and Resource Centre and was approved by the inStem Institutional Animal Ethics Committee, following the norms specified by the Committee (Approval Numbers: INS-IAE-2018/03(E), INS-IAE-2020/12(N), NCBS-IAE-2012/05 (R1) SC-5/2009 SC-5/2012 and the CPCSEA registration no. is 109/GO/bc/99/CPCSEA) for control and supervision of experiments on animals (Government of India). We used the C57BL/6 strain of female mice and the Wistar strain of male rat; these were housed in the institute animal house and were maintained in a 12 h light/dark cycle. The animals used in our studies were 6-8 weeks in age.

3.2 Preparation of heart tissue for CLARITY

All the heart samples used in this study were collected from animals scheduled for culling by the NCBS/inStem Animal Care and Resource Centre facility. In this study we used wild-type C57BL/6 strain of female mice aged between six to eight weeks. Following anaesthesia, a transcardial perfusion method was employed before tissue collection. To minimize pain and distress, deep anaesthesia was confirmed before proceeding. Once an animal was sacrificed after, we immediately performed perfusion to remove blood and clots from the heart tissue. We began by cutting the abdominal cavity of the mouse to access the heart gently. A small incision was made in the right atrium to facilitate fast perfusion of the heart chambers. The perfusion was carried out manually using a 26 Gauge syringe needle inserted at an inclined angle at the apex region of the right ventricle. We injected 10X phosphate-buffered saline solution (PBS) with a stock solution containing 1.37 M NaCl, 27 mM KCl, 100 mM Na2HP04, and 18 mM KH2P04, with the pH adjusted to 7.4. Initially, ice-cold heparinized 1X PBS was passed through the syringe, followed by ice-cold 4% paraformaldehyde (PFA). Subsequently, a hydrogel monomer solution consisting of 4% acrylamide, 4% PFA, 0.5% Bisacrylamide and 0.25s% photo-initiator 2, 20-Azobis[2-(2-imidazolin-2-yl) propane] dihydrochloride (VA-044, Wako Chemicals USA) in PBS was perfused through the heart, as described previously for CLARITY based clearing of brain tissue (62). The fixed mouse heart sample was transferred into a 50ml tube and incubated at 4°C for seven days in the hydrogel monomer solution. The fixed heart tissues were degassed for 10 minutes using a vacuum chamber at room temperature. To initiate

tissue-hydrogel hybridization and polymerization, the processed heart tissues were then incubated for 3 hours at 37°C. After polymerization, excess gel material was carefully removed by gently rubbing the tissue with soft tissue wipes. The tissue was transferred to 50 ml tubes for 1X PBS washes, which were carried out three times for 10 minutes each time. The tissue was further incubated with a clearing buffer (8% SDS and 4% boric acid in 1X PBS (pH 8.5)) for 20-30 days at 37°C in a shaking incubator (180 rpm) with a buffer exchange occurring every week. This CLARITY-based approach to the heart tissue samples resulted in transparent tissue (Figure 20 a), which enabled deep tissue imaging using a confocal microscope.

3.3 Sectioning of heart

The cleared heart tissue was affixed with superglue at either its short-axis or long-axis orientation in a specimen tube (Compresstome® VF-300 OZ, Precisionary instruments) (Figure 20 b). The specimen tube was a cylindrical holder with its outer rim fixed and the inside platform (or stage) movable. The glued heart tissue was embedded in 2.5% low-melting agarose. For a short axis view, the tissue was placed so that the base of the heart was touching the stage of the specimen tube. The tissue was kept in a plane on the stage for a long-axis view, allowing its four chambers to be seen. We used the Compresstome® to obtain 500µm thick tissue sections with an oscillation frequency of 7 units and a speed of 1.5mm/sec. The Compresstome® blade was kept close to the specimen tube, enabling the compression effect of sectioning to be distributed perpendicular to either the long axis or the short axis of the heart sample. The sectioned tissue was collected in 1X PBS in the chamber associated with the Compresstome®. Each section was carefully transferred to one of 24 well plates filled with 1X PBS while maintaining the sectioning order. For this study, the short axis sections were approximately 3mm away from the apex and the long axis sections were approximately 3mm from the opposing outer walls of the heart. The apex sections were cut in the short axis plane from the apical tip of the heart.

3.4 Staining of mouse heart sections

To carry out staining, 500µm processed sections were washed in 1X PBS thrice over a day and permeabilized using a buffer containing 1% Triton X-100 (H5141, Promega) in PBS (PBST) for one day in a 37°C incubator shaker. Subsequently, the tissue sections

were incubated in 150µg/ml of Alexa Fluor™ 633 conjugated wheat germ agglutinin (WGA, W21404, ThermoFisher) for one day to stain cell membranes. The samples were washed with 1X PBS (3 times for 10 minutes each) before incubating them in imaging media (RIMS). For the preparation of RIMS, 40g of Histodenz (Sigma, D2158) was dissolved in 30 ml of 0.02 M phosphate buffer with 0.01% sodium azide, pH 7.5, resulting in a final concentration of 88% w/v Histodenz. The labelled tissue samples were incubated in RIMS until the tissue became more transparent [2]. All the staining and washing steps were carried out at room temperature, with gentle shaking. The cleared tissue samples were mounted with fresh RIMS solution using spacers (IS002, SUNjin Lab, Taiwan) of 500µm such that the tissue was sandwiched between coverslips of size 60mm × 20mm (Figure 12).

3.5 Mounting the tissue sample for microscopy

For image acquisition, we used an Olympus FV3000 microscope. Images were first obtained using a lower magnification objective (Olympus PlanApo 1.25X/ air objective) to image a complete area of the heart tissue section. This low-resolution image was used to map high-resolution imaging areas of interest using the Olympus fluoViewTM software. Then, micron-scale imaging was carried out with the Olym- pus UCPLFN 20X Corr M32 85mm scale air objective (NA=0.73). We used a 640nm laser line for excitation and FV3000 high sensitivity spectral detectors (gallium arsenide phosphide (GaAsP) photomultiplier tube (PMT) for detection of emission over a range of 650 − 670nm. Each field of view covered approximately 320 × 320 pixels, with a voxel size of 1.98 × 1.98 × 1.98µm3 and a depth of ∼ 300µm. Here we under-sampled in the X and Y directions to obtain an isotropic voxel resolution equivalent to the sampling interval in the Z direction. Using the fluoviewmap function from Olympus fluoViewTM software, we ensured that the acquired 3D images were continuous and had at least 25% overlap with their respective neighboring fields of view. To minimize the laser attenuation at deeper regions of the tissue sample, the laser power was corrected (i.e., increased) with the help of the Bright Z function, with a manual judgement based on the quality of the intensity obtained at deeper layers. Each field of view was manually corrected for laser power intensity, increasing this by up to 10% with increased depth. The images were acquired following a snake pattern from row to

row. Image reconstructions were performed using computer vision algorithms using

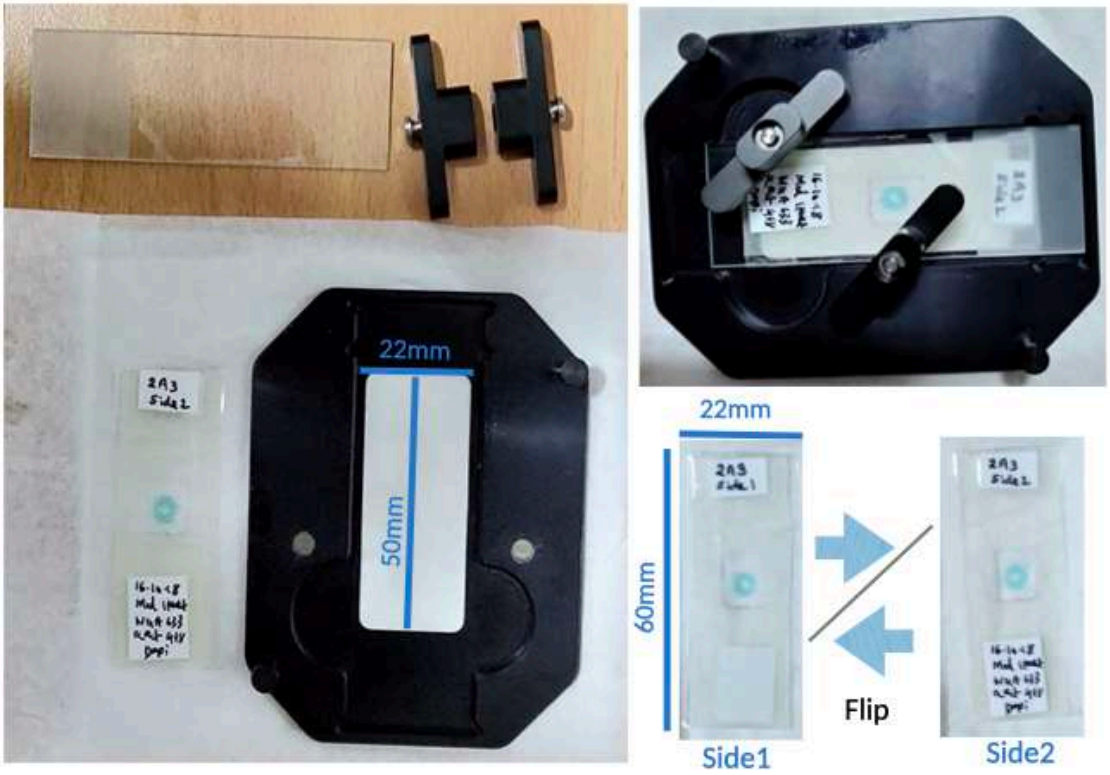

Figure 12: Sample mounting between coverslips.
Stained tissue sections are sandwiched between two coverslips of 60X22mm size along with a refractive index matching solution (RI 1.46). A spacer matching that to tissue thickness is used in between the coverslips to prevent the tissue from compression. The mounted sample was secured with magnetic clippers provided with Olympus FV3000 stage and a glass slide. The sample can be imaged from both sides by flipping.

custom-written MATLAB and C++ scripts. After imaging, the heart tissue samples were stored in RIMS at room temperature and protected from exposure to light. In order to observe other cell types or Z-disc arrangement (α-actinin), as shown in Appendix Figure 3, a 60X magnified imaging of cleared tissue was carried out using PlanApo N 60X oil objective (NA=1.42) with a scan size of 320 × 320 pixels, with a voxel size of $0.66 \times 0.66 \times 0.79 \mu m^3$.

3.6 Image acquisition of tissue sections in 3D

For image acquisition, we used an Olympus FV3000 microscope. Images were first obtained using a lower magnification objective (Olympus PlanApo 1.25X/ air objective) to image a complete area of the heart tissue section. This low-resolution image was used to map high-resolution imaging areas of interest using the Olympus fluoViewTM software. Then, micron-scale imaging was carried out with the Olympus

UCPLFN 20X Corr M32 85mm scale air objective (NA=0.73). We used a 640nm laser line for excitation and FV3000 high sensitivity spectral detectors (gallium arsenide phosphide (GaAsP) photomultiplier tube (PMT)) for detection of emission over a range of 650 − 670nm. Each field of view covered approximately 320 × 320 pixels, with a voxel size of 1.98 × 1.98 × 1.98μm^3 and a depth of ~ 300μm. Here we under-sampled in the X and Y directions to obtain an isotropic voxel resolution equivalent to the sampling interval in the Z direction. Using the fluoviewmap function, we ensured that the acquired 3D images were continuous and had at least 25% overlap with their respective neighboring fields of view. To minimize the laser attenuation at deeper regions of the tissue sample, the laser power was corrected (i.e., increased) with the help of the Bright Z function, with a manual judgement based on the quality of the intensity obtained at deeper layers. Each field of view was manually corrected for laser power intensity, increasing this by up to 10% with increased depth. The images were acquired following a snake pattern from row to row. Image reconstructions were performed using computer vision algorithms (using custom-written MATLAB and C++ scripts). After imaging, the heart tissue samples were stored in RIMS at room temperature and protected from exposure to light. In order to observe other cell types or Z-disc arrangement (α-actinin), as shown in Figure 43 and Appendix Figure 3, a 60X magnified imaging of cleared tissue was carried out using PlanApo N 60X oil objective (NA=1.42) with a scan size of 320 × 320 pixels, with a voxel size of 0.66 × 0.66 × 0.79μm^3.

3.7 Alignment of different short-axis sections

We aligned the short-axis datasets to ensure uniformity across different short-axis sections, using the AHA classification and the capillary vessel description for the PSAX-PML level used in echocardiogram studies. We used the SAS3 dataset (Appendix. Table 1) as a reference. First, we aligned the posterior and anterior papillary muscles to the positions of the anterior and inferior regions globally. All other datasets were aligned using the outer wall and papillary muscle morphology to the SAS3 dataset with the help of a MATLAB script and the ImageJ package. To obtain consistency between section alignments at a coarser scale, some datasets were flipped (horizontally or vertically) when needed, using ImageJ. The MATLAB script takes the SAS3 dataset as a reference and shows it as a transparent layer. This transparent layer can be rotated

by an angular value to allow fine alignment changes. Once the angular value for in-plane rotation had been determined, the short-axis datasets were rotated in-plane and saved using ImageJ. The SAS3 and SAS4 had similar morphology. The SAS1 dataset required a −10° in-plane rotation, and the SAS2 dataset required a −7° in-plane rotation. The SAS5 dataset was manually rotated by 180° in-plane. At the end of this process, all the short-axis datasets had a consistent alignment according to the AHA classification, including the positioning of major blood vessels.

3.8 Analysis of short-axis sections from uncleared mouse and rat hearts

We analyzed uncleared hearts from a mouse (SAS7) of 1.5 months old and a different species, a wild-type Wistar strain of a male rat (RSAS1), approximately eight weeks in age, which had been scheduled for culling in the NCBS/inStem animal facility. Once the mouse/rat had been sacrificed, we performed a similar procedure described in section 1.1. Once the perfusion was completed, the heart was excised and stored in 4% PFA at 4◦C. The fixed heart was incubated in 30% sucrose for 5hrs before sectioning to enable the tissue to withstand freezing temperatures. The mouse/rat heart was cut into two thick blocks perpendicular to the long axis of the heart (i.e., short-axis views). The resulting mid-ventricular region was suitable for cryo-sectioning. On the sectioning day, the mouse/rat heart was inserted in a mold containing tissue freezing medium and allowed to solidify at −20°C. The frozen sample was attached to a holder for cryostat (slee mev+), where the heart specimen was placed perpendicular to the long axis of the heart and sectioned into 100μm slices from the midventricular region. The sections were carefully transferred to 24 well plates containing 1X PBS and were then washed (3 times for 10 minutes each) to remove freezing media. Afterward, the tissue sections were incubated in 150 μg/ml of Alexa Fluor™ 633 conjugated wheat germ agglutinin (WGA, W21404, ThermoFisher) for one day to stain the cell membrane. For α-actinin staining of uncleared or cleared mouse tissue, the tissue was blocked with 2.5% BSA + 2.5% neonatal goat serum in 1X PBST (1% Triton X) for 2 hours. 1:200 dilution of primary antibody (Monoclonal anti-α-actinin rabbit antibody, Cell Signalling, D6F6, 6487) and 1:400 dilution of secondary antibody (Anti Rabbit Alexa-647 Goat antibody, Life technologies, A21245) were used sequentially with incubation of a day at room temperature. The samples were washed with 1X PBS (3 times for 10 minutes each) and incubated in RIMS subsequently for another day. We used a positively charged glass

slide for mounting the uncleared mouse/rat heart tissue sections and custom-made 100µm spacers (100µm plastic sheets).

The stained heart sections were placed in this glass slide set up with RIMS and sealed with a cover glass in preparation for imaging. We used an Olympus FV3000 microscope and a lower magnification objective (Olympus PlanApo 1.25X/ air objective) to image the complete area of the tissue section to determine the best plane of view. This low-resolution image was used to map the high-resolution imaging area of interest using the Olympus fluoView software. The micron-scale imaging was done with the Olympus UCPLFN 20X Corr M32 85mm scale air objective (NA=0.73). Each field of view consisted of 320×320 voxels per slice, with a voxel size of 1.98×1.98×1.98µm^3, over a depth of 10µm and 50µm for mouse and rat, respectively. As with the cleared mouse hearts, we under-sampled in the X and Y directions to obtain isotropic pixels at the resolution of the sampling in the Z direction. We used automatic tile acquisition via the fluoView software platform. Using the fluoviewmap function, we ensured that the acquired 3D images were continuous with an overlap of 25 % with their neighbouring tiles, regulated by a motorized microscope stage. The fields of view were obtained row by row, following a snake pattern, and were then stitched using custom-built software.

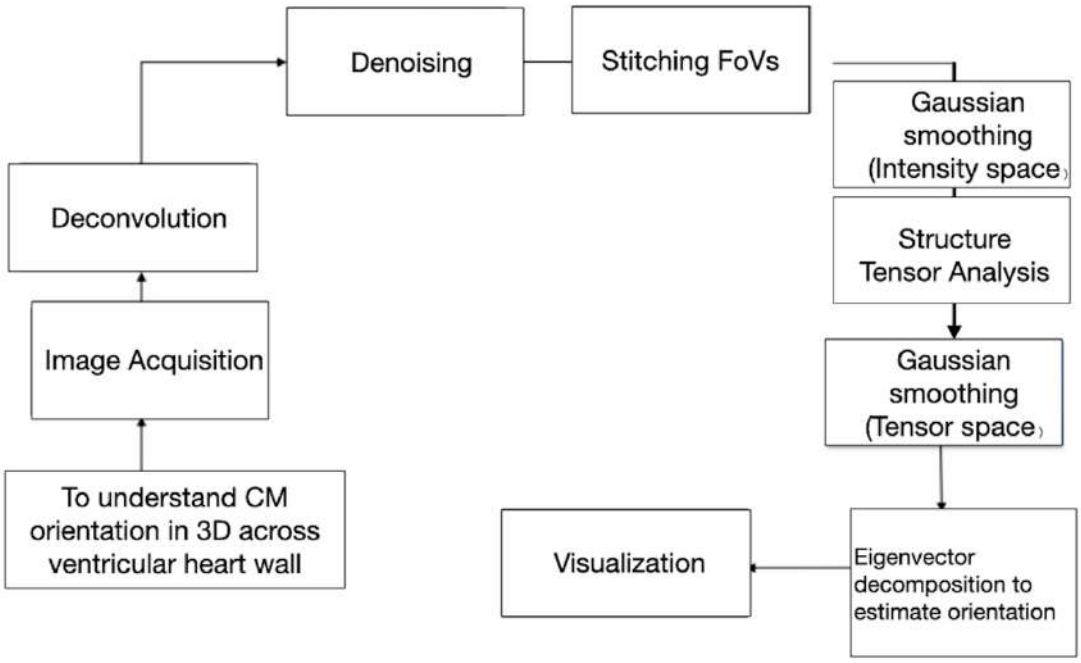

Figure 13: Flowchart for computational pipeline.
The images as acquired by a tiled scan using a confocal microscope to cover the whole tissue area. Each field of view is applied by preprocessing steps i.e deconvolution and denoising. The processed fields of view are stitched before applying a Gaussian smoothing in order to define the intensity range. The structure tensor analysis is applied

later on followed by a gaussian smoothing in the tensor space. The estimated orientations are visualized applying an eigenvector decomposition. CM- Cardiomyocyte, FoV- Field of view.

3.9 Pre-processing of acquired images

The decrease of image quality at greater depths due to light scattering, absorption, and optical variables poses a substantial difficulty for quantitatively analyzing confocal images of thick tissues. We created an image restoration pipeline to reduce the effects of noise and other degrading artifacts in images taken hundreds of microns below the surface of undamaged tissues. Deeper layers of thick biological tissue samples frequently produce imaging data that is poorly resolved because of poor light permeability. Additionally, optical elements like light scattering and lens aberrations reduce the quality of the image. One technique to counteract such effects is to utilize optical clearing to lessen the influence of the various refractive indices of diverse biological tissue types. The tissue samples and materials with comparable refractive indices have decreased scattering and absorption, enhancing optical signal penetration. However, deeper layers in optically cleaned tissue can still experience blurring and image degradation effects when imaging using a traditional confocal microscope.

a. Deconvolution

It is feasible to sharpen these images using a deconvolution method if we are aware of the point spread function of the microscope's objective. However, the consequences of depth degradation are still present. The point spread function (PSF) of the microscope's objective lens was used to obtain the confocal images, which were blurred due to the thick tissue sections being imaged in three dimensions. Figure 14 displays a PSF pseudo-color image that was created using the parameters of our microscope. In order to lessen the effects of this blur, we deconvolved each tile using the Richardson-Lucy (RL) deconvolution technique (63).

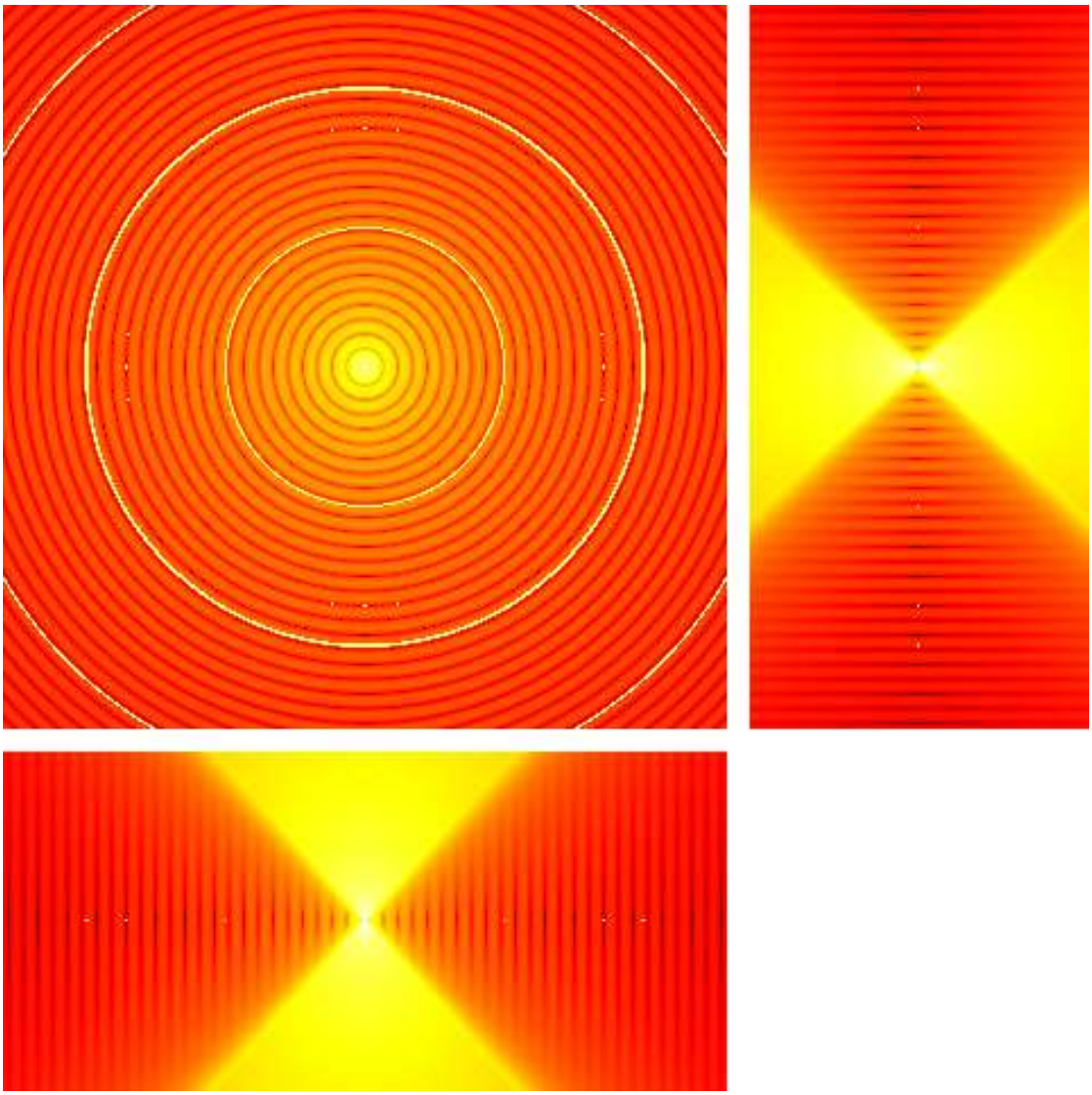

Figure 14: Point spread function.
A visualization of the middle planes of a 3D point spread function (PSF) along the XY (top left), XZ (bottom left) and YZ (top right) directions, shown in log intensity scale (increasing from black through yellow and red to white).

b. Denoising

We used a dictionary learning based algorithm to recreate clear images from depth-damaged data (Figure 15). The basic concept is to use the texture and intensity pattern of the shallow layers as a proxy for what clean images from deeper levels should appear, presuming that the tissue is self-similar (64). Then, a deep tissue image is modified while maintaining the image's isophote geometry to match the lower layers' statistics. The dictionary was extracted from the shallow layers of image stacks under the assumption that the deeper and shallow layers contained common substructure elements of cells. This set of learned dictionary patches (a sparse 256 element 2D dictionary of patches of size 16×16, shown in Figure 15. The algorithm obtains a bi-directional

mapping between the shallow and deep layers so that the cleaned/restored deep layers resemble the shallow ones improving quality.

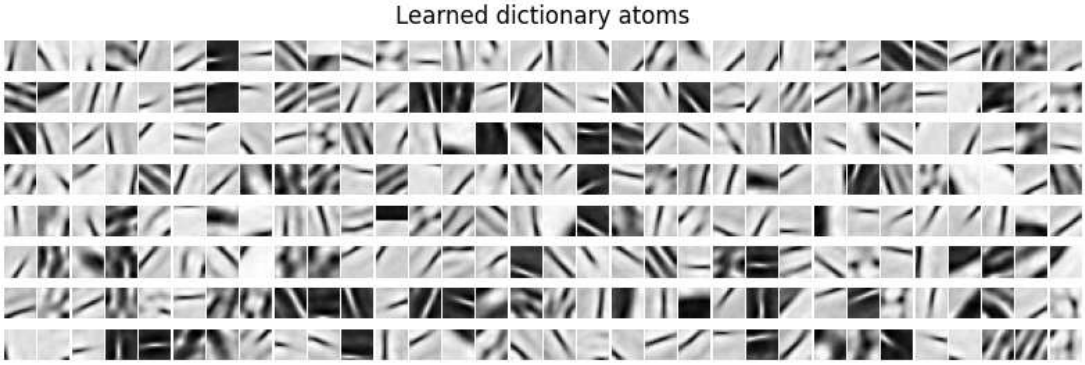

Figure 15: A visualization of the dictionary atoms learned for the mouse cardiac tissue microscopy image dataset SAS1.

3.10 Stitching of fields of view

Each tissue section was too large to be imaged at once, so we imaged multiple square-shaped fields of view (tiles) of 320 × 320 isotropic voxels of length 1.98μm in each dimension in the regions containing tissue samples. Adjacent tiles were set to overlap at 12.5% in every direction. We used the image registration method described in (65) for regions with valid data. The method involved a two-stage registration process, with a local pairwise registration followed by a global registration. In the first local registration stage, we started with an initial guess for the location of each tile, derived from the microscope stage settings, and assumed a 40 voxel (12.5%) overlap value. For every pair of adjacent tiles (a, b), we used the maximum phase correlation based registration to estimate the relative shift between the pair. For every imaged tile, a shift was computed with each of its 4-neighbors in the 2D imaging plane. This local pairwise registration process resulted in a refined list of pairwise relative shift values. Figure 27 b illustrate the stitching process for a short-axis section of a mouse heart. Two sample tiles are demarcated by purple and green bounding boxes.

3.11 Analyzing cardiomyocyte orientation

Using WGA fluorescence signal that marks the membranes showed a strong signal for the boundary of myocytes and a relatively weak intensity surrounding the membrane, as seen in Figure 16. We then used the WGA signal to estimate the myocyte orientation. At each voxel, we compute the second-moment matrix for intensity gradient derivative and the structure tensor (66). The direction of the eigenvector corresponding to the

smallest magnitude eigenvalue is used to determine the orientation at each voxel (Figure 17). We infer the orientation at each voxel by calculating the structure tensor of the WGA intensity of preprocessed (both deconvolved and denoised) images. The calculated structural tensor at each voxel at the appropriate scale can then be broken down using an eigenvector.

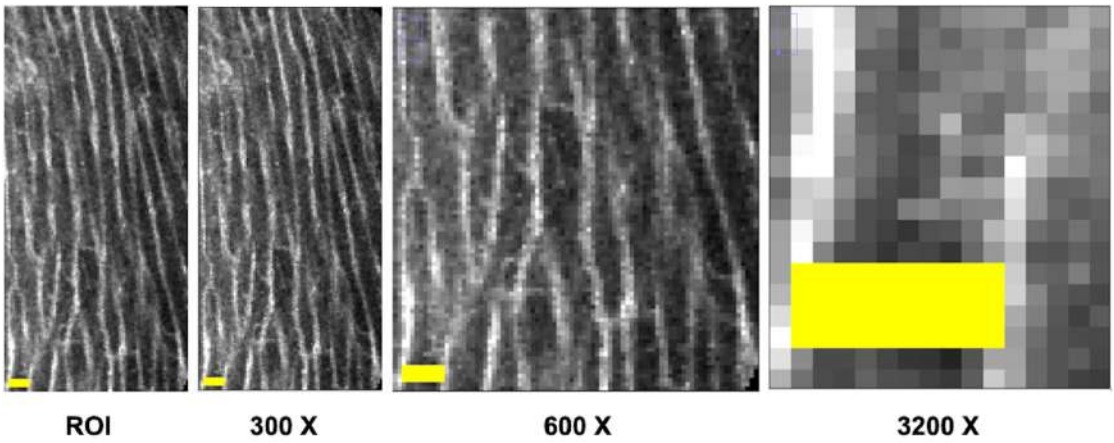

Figure 16: Intensity gradient data from WGA staining.
20X images are zoomed digitally to 300, 600 and 3200 times to show the pixel details in the image. WGA marks the cell membrane regions and the microscope captures this data in a gray scale of intensity values. Near to the boundaries of cell, the pixels with high intensity value can be found whereas near to the cytoplasmic side, low intensity pixels will be located.

a. Structure tensor method

As the first step, images were smoothed to fσ, using a Gaussian kernel kσ(x) with standard deviation σ. In our experiments, we set σ = 0.5. The choice of noise scale controls the amount of smoothing prior to the computation of gradients. This smoothing makes the gradient ignore intensity variation at scales smaller than σ. Since we use denoised data, using the dictionary denoising method, prior to orientation estimation, a minimal sigma value is chosen. The tensor T is computed at every voxel. Therefore, an intensity-valued image is converted into a tensor-valued image, where each tensor captures the orientation at a voxel instead of the intensity itself. Suppose we decompose this tensor into its eigenvectors. In that case, the eigenvector corresponding to the eigenvalue with the highest magnitude will point in the direction of the highest intensity change at that voxel, i.e., the gradient direction. This orientation is, however, based on the contrast at a single voxel and therefore is not very robust. To account for the context around a voxel, we then average these tensors, again using a Gaussian kernel with

standard deviation ρ. Unlike the earlier smoothing use σ, which averages in the intensity space, this averaging occurs in the orientation (Tensor) space.

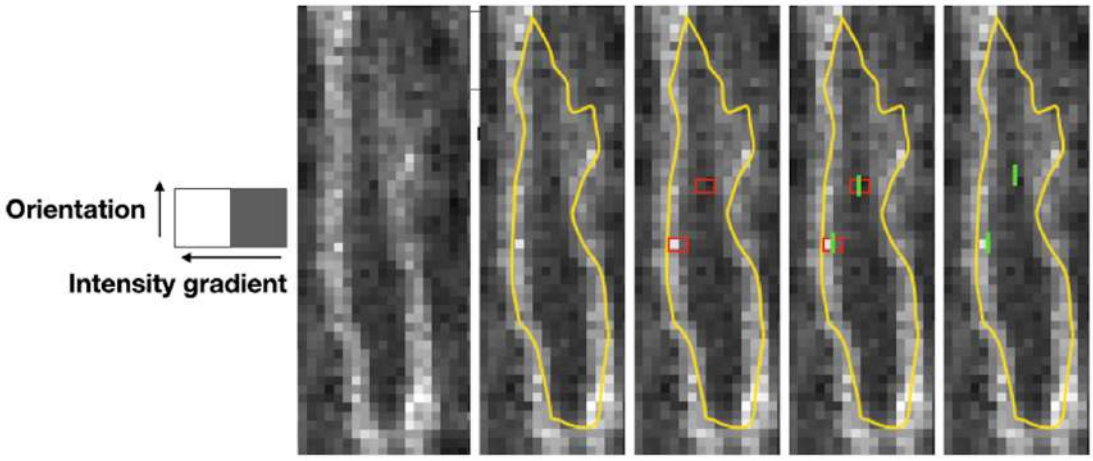

Figure 17: Example for intensity gradient derived orientation estimates.
Orientation direction is defined to the direction where intensity gradient least changes. In the images, an in-plane cardiomyocyte region from 20X imaging is showcased. The boundary of cardiomyocyte is marked by hand sketch (yellow). Few example regions for the change in intensity of pixels are selected in red boxes. The orientation is marked on top as green lines.

b. Assigning vector orientation for individual cardiomyocytes of the stitched datasets

To mitigate the effect of the reduced image quality on orientation estimation, we averaged the orientation field with respect to local neighborhoods. Although orientations are not directional, their representation using the eigenvector with the smallest eigenvalue of the structure tensor is directional. Two vectors whose components have the same magnitude but differ in signs represent the same orientation, so these direction vectors cannot be directly averaged component-wise. We averaged the orientation tensors component-wise using a local weighted average and then projected them back to the space of direction vectors. We only performed smoothing in regions within the heart tissue by setting the weight to zero in the heart sections that were missing data.

3.12 Validating orientation estimating with hand-segmented data

To verify the accuracy of the orientations estimated using the structure tensor, we hand-segmented 70 cardiomyocytes in a field of view from the dataset SAS3 by manually tracing the boundaries of individual cells across multiple slices. The myocytes were marked by labeling the cytoplasm within each cell boundary, as signaled by WGA

staining. The orientation of each hand-segmented cell was then calculated using the second-moment matrix of the interior voxels of each labeled myocyte. Each hand-segmented cell was assigned a ground truth cell orientation by using the eigenvector corresponding to the eigenvalue of the second-moment matrix with the most considerable magnitude. We then associated a structure tensor-based orientation for the cell using the average of the estimated field orientations from the raw WGA image over each interior voxel.

3.13 Angular parameters for the cell orientation

- Phi(φ) is the acute angle between the estimated cell orientation and the Z-projection
- Theta (θ) is the acute angle between the projection of the estimated cell orientation (myofiber orientation) onto the short-axis (XY) plane and the X-axis
- Helix Angle (αH) is the angle between the projection of the myofiber onto the local tangent plane to the heart wall and the Z-axis direction.

To estimate the wall-normal, we computed a single pixel-wide boundary of the heart in a short axis section and a global circular fit with the best overlap to the outer boundary of the ventricle. The direction of the heart wall normal was then associated with the inward radial vector of the circular fit. In addition, we also used a single circular fit to all outer boundary points in the heart. The Figure 19 shows the estimated normal for the heart boundary for dataset SAS3. The local helix angle αH, as illustrated in Figure 19, was calculated using the projection of the orientation onto the tangential plane defined by the heart wall normal. The angle varied from -90° to 90°, with 0° representing the in-plane circumferential fibers and $\pm 90^\circ$ representing fibers pointing out of the short axis plane in the long axis direction of the heart.

The colormaps for Φ, θ, and αH were generated using the smoothed orientation field. We calculated the Φ and θ angles at each voxel with valid data and then mapped these angles to color values using a linear scale in the parula colormap.

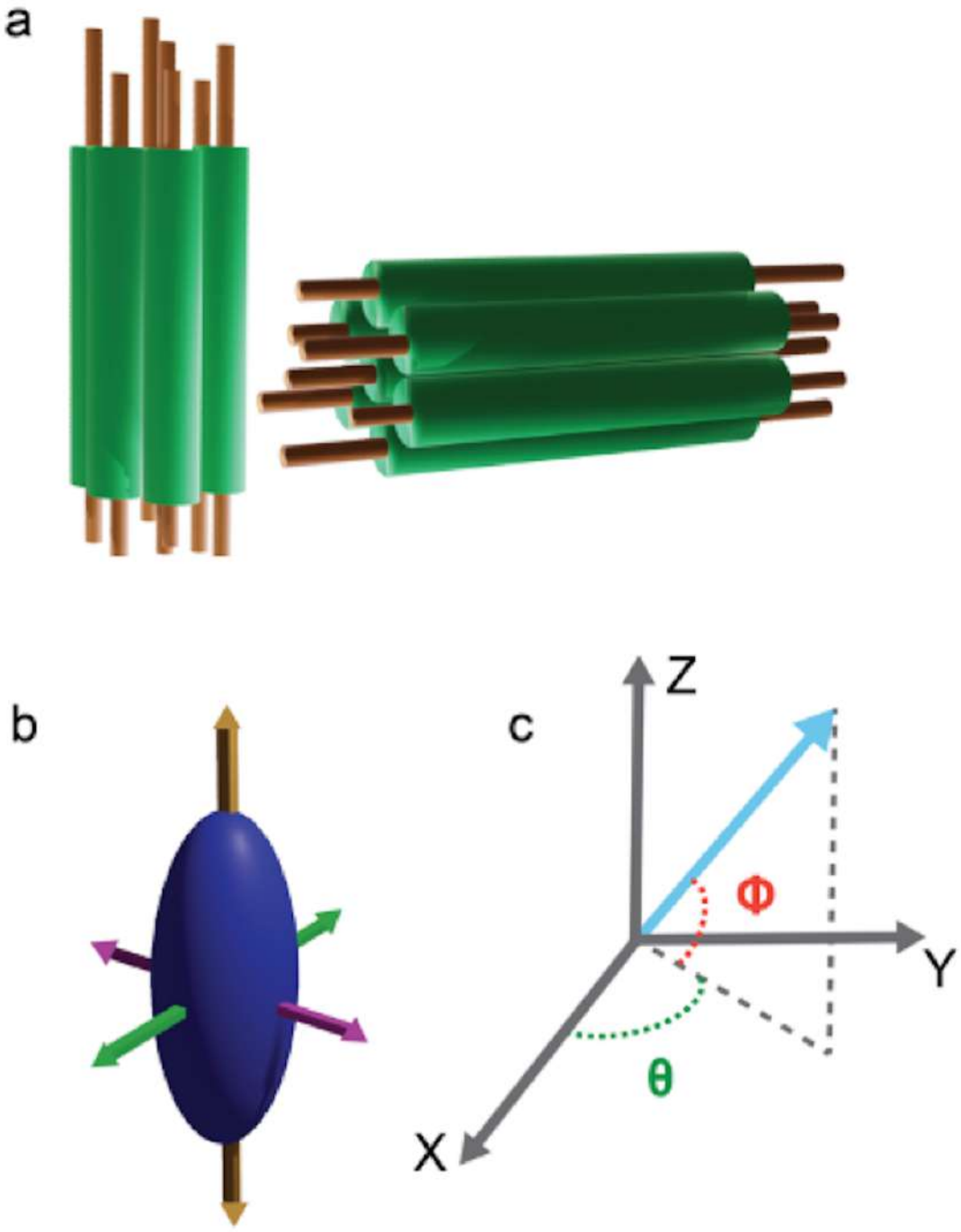

Figure 18: Graphical representation for cardiomyocyte alignment and angular parameters.
a. Illustration of cell orientation estimation using a structure tensor method (Methods). The structure tensor eigenvectors with the smallest eigenvalue (golden yellow dashed lines) align to the long-axis direction of the cardiomyocytes (green cylinders) respective to their given any spatial orientation in a 3D block of tissue. **b.** Illustration of X,Y,Z coordinate system. **c.** an elongated tensor (the preferred orientation is in the direction of elongation). **c.** An illustration of the angles measured to represent the cell orientations across the ventricular walls. The red box represents a magnified view of the ventricle wall, with the global axes and labels as indicated. The green cylinder and the blue bi-directional arrow represent the cardiomyocyte and its long-axis, i.e., the estimated cell

orientation, respectively. Φ is the angle between the global Z-axis and the estimated cell orientation. θ is the angle between the projection of the estimated cell orientation onto the XY plane and the X-axis direction. αH, the helix angle, is the angle between the projection of the cell orientation on to the plane perpendicular to the transmural penetration direction and the circumferential direction.

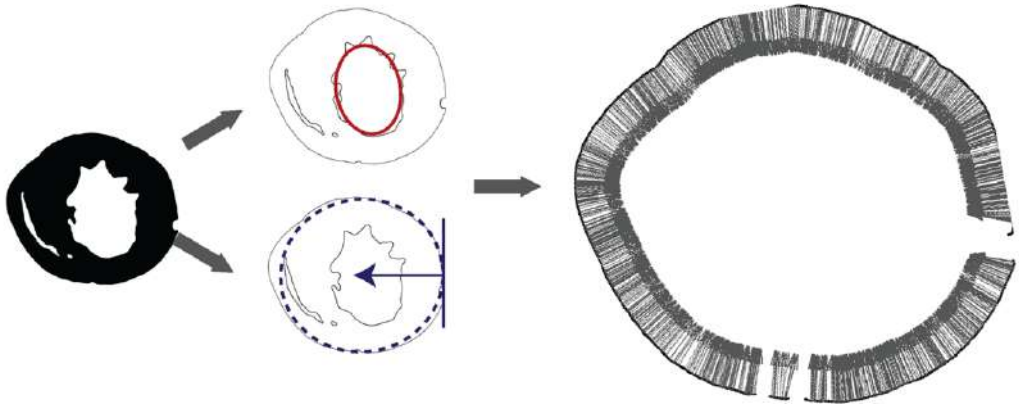

Figure 19: Representation for transmural penetration direction estimates.
Helix angle calculation: Masking followed by centroid estimation (top); Masking the short-axis section and estimating the tangent plane and normal for the penetration axis (bottom).

3.14 Cell orientation as glyphs and streamlines

DT-MRI employs the diffusion of water molecules as a proxy for orientation. DT-MRI-derived orientation estimates can effectively showcase the changes in 3D for individual voxels and their aggregates within a neighborhood through visualizations employing glyphs and streamlines (32). Therefore, we have adopted glyphs to portray local orientation changes as a function of intensity gradient for each cardiomyocyte in a 3D tissue stack and bidirectional streamlines to show aggregate (myofiber) orientation across heart walls.

We estimate the local orientation of each cardiomyocyte using the eigenvector of the structure tensor (a measure of local orientation) with the smallest absolute eigenvalue. The structure tensor is calculated by taking the dot product of the gradient of the image with itself, after filtering the image with a Gaussian filter. The orientations are then smoothed by filtering the directionless rank 1 tensor (a tensor that has only one nonzero eigenvalue) with another Gaussian filter. The smoothed orientations are then estimated using the eigenvector of the smoothed tensor with the largest eigenvalue. These smoothed orientations can be used to estimate the global orientation of the myofibers. The myofibers are traced as streamlines, which reveal that they are oriented out-of-plane in the outer region of the left ventricle and in-plane in the interior wall. We also observe a gradual twisting of the cells as we move from the outer to the inner wall.

These quantitative estimates are consistent with previous studies that used histological or DTI methods at a much coarser scale (28,30,67–69). Our method allows us to analyze cell geometry at a much finer scale than has been possible previously.

CHAPTER – 4
RESULTS

4.1 Optimizing the imaging conditions

a. CLARITY protocol enables improved in-depth imaging

The CLARITY tissue clearing method involves a hydrogel embedding of tissue followed by a series of passive buffer washes to remove lipids and other opaque components with mismatched refractive indices from the tissue (Methods; Figure 20). This increases the tissue's transparency and minimizes the influence of light scattering enabling in-depth imaging (Figure 20 a). We strategically sectioned the tissues both in short and long axis planes of heart (Figure 20 b). Figure 20 c shows the imaging quality and depth difference between the tissue that was produced with CLARITY (right panel) and the tissue that was prepared without tissue clearing (left panel) (right panel).

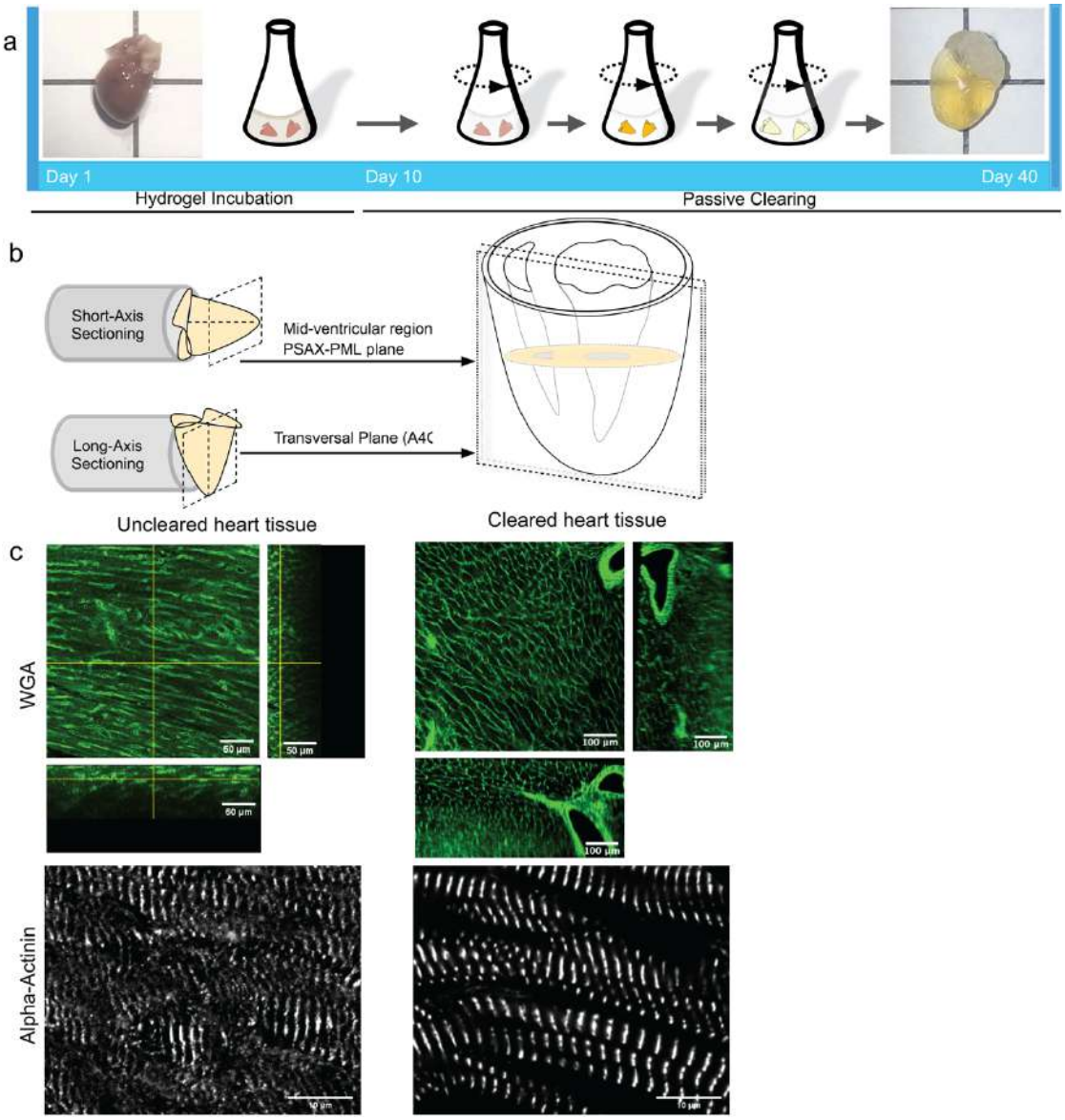

Figure 20: A comparison of cleared and uncleared mouse heart tissue by imaging.
a. A schematic illustration of the CLARITY method. The harvested heart tissues are incubated in a hydrogel/PFA mixture at 4°C for approximately nine days. Following

hydrogel incubation, the solution mixture with the heart tissues is polymerized at 37°C. The heart tissues are then excised from the polymerized hydrogel and shaken at 37°C with a clearing solution until they attain a desirable level of transparency (See Methods for details). **b.** The clarified heart is sectioned along its Short- or Long-Axis. For the short-axis, a mid-ventricular region that approximates the PSAX-PML (parasternal short-axis – papillary muscle level) plane was chosen. For the long-axis, a transversal plane that represents the A4C (apical four chambers) plane was used. **c.** A comparison of uncleared and cleared heart tissue sections stained with WGA and the alpha-actinin antibody. The scale bar is 50 microns for WGA images and 10 microns for the alpha-actinin images.

b. Selection of objective and resolution:

The WGA staining will label all cells including cardiomyocytes, fibroblasts, the epithelial lining of capillaries. Since the cardiomyocytes are elongated long cells with approximate dimensions of 100-150 micron in length and 10-20 microns in width (Figure 21), we chose a 20X objective (NA/air) and captured the images at 1.98 um^3 voxel resolution. At this resolution, we were able to resolve only the cardiomyocyte boundaries and notice staining on the capillaries, as shown in Figure 21a. Fibroblasts make up the majority of the cells in heart tissue in number, but they only occupy around 25% of the entire volume (70). They encircle and cover the limited extracellular regions of the myocytes. Even though they can be seen clearly at higher magnifications, fibroblasts cannot be detected satisfactorily at the resolution we have chosen (Figure 21).

The numerical aperture (NA) of an objective can influence the resolution and working distance (WD) of the objective. A general thumb rule is that higher the NA, higher the resolution and lower will be WD and vice versa. The axial resolution of an objective will be always poorer compared to its lateral resolution part. Therefore, imaging with a 10X magnification objective (NA/air) satisfied the required lateral resolution but suffered in axial resolution and was not suitable for 3D cardiomyocyte analysis (Figure 22). Imaging with a 60X magnification objective (NA/oil) leads to a better resolved images both axially and laterally; however, 9 FOVs are required to cover the same area of tissue section imaged by a single FOV using 20X objective. Therefore, 60X imaging was hugely time-consuming process, moreover at deeper sections of tissue the SNR was poor leading to a lower depth of coverage of the sample. A comparison of the area covered by 20X vs 60X objective demonstrates approximately nine fields of view of 60X imaging is required to equate the are covered by one field of view of 20X imaging (Figure 23).

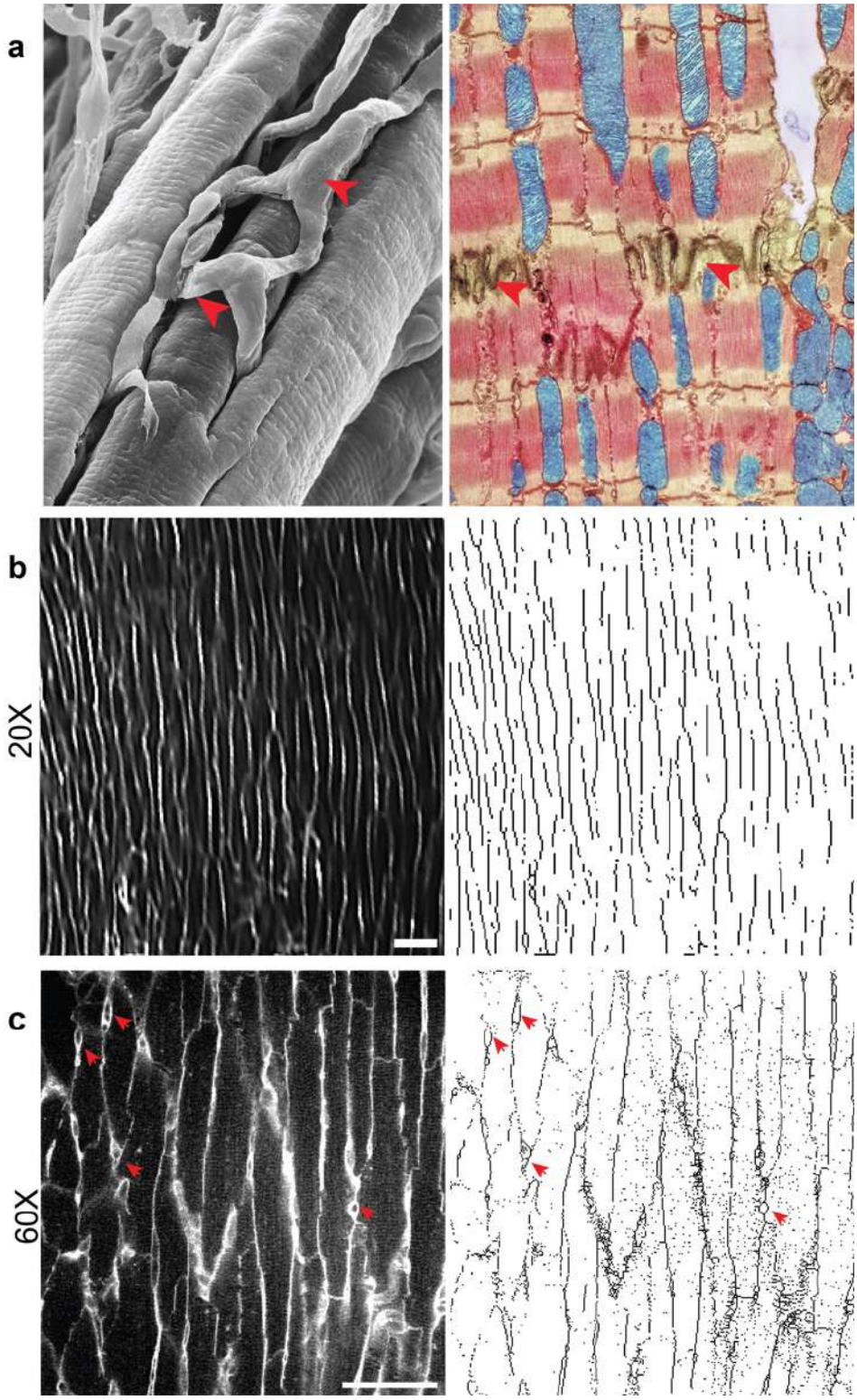

Figure 21: Resolution effects on cell boundaries.
a. SEM (left) and TEM image of cardiomyocytes. A capillary surrounding the cardiomyocyte and the intercalated disc region is marked is marked with arrow heads on SEM image and TEM image respectively. **b-c.** A comparison of 20X (2-micron isotropic resolution) and 60X (0.663 * 0.663 * 0.79 μm^3 x, y, and z resolution, respectively) cleared heart tissue sections stained with WGA. The raw and skeletonized images are shown for each magnification. The visible cell boundaries that are not of

cardiomyocytes are marked with arrow heads (red) in the 60X images. The scale bar is 50 microns.

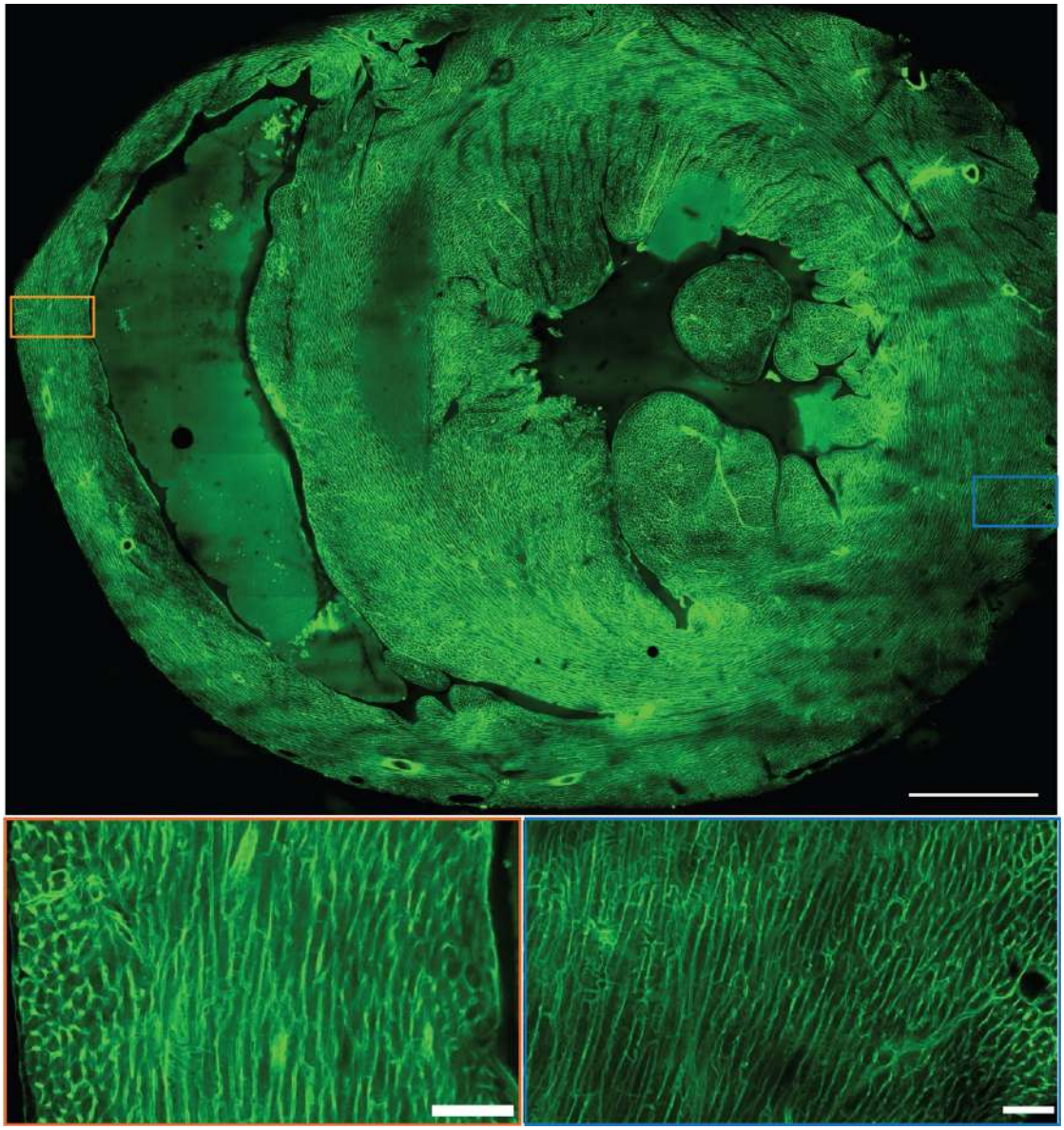

Figure 22: The overview of WGA-stained tissue section at 10X magnification.
A representative image acquired with 10X objective covering the entire area of the short axis tissue section. Staining is for the cell membrane by WGA (green). Scale bar is 1000 microns for upper panel and 100 microns for the bottom panels.

Imaging with a 20X objective led to 1.98um^3 isotropic voxel resolution, which provided sufficient information for tracing cardiomyocyte orientation at micron scale and conducive for tiled imaging to cover the entire heart section. The investigation pertaining a subcellular resolution would require a higher magnification objective (Appendix Figure 1) with a tradeoff of higher imaging time spanning areas and reduced depth of imaging. Finally, I decided to imaging with a 20X objective and undersampling

the tissue sections at 1.98um^3 isotropic voxel resolution such that no other small cell types other than cardiomyocytes can be resolved (Figure 21 b).

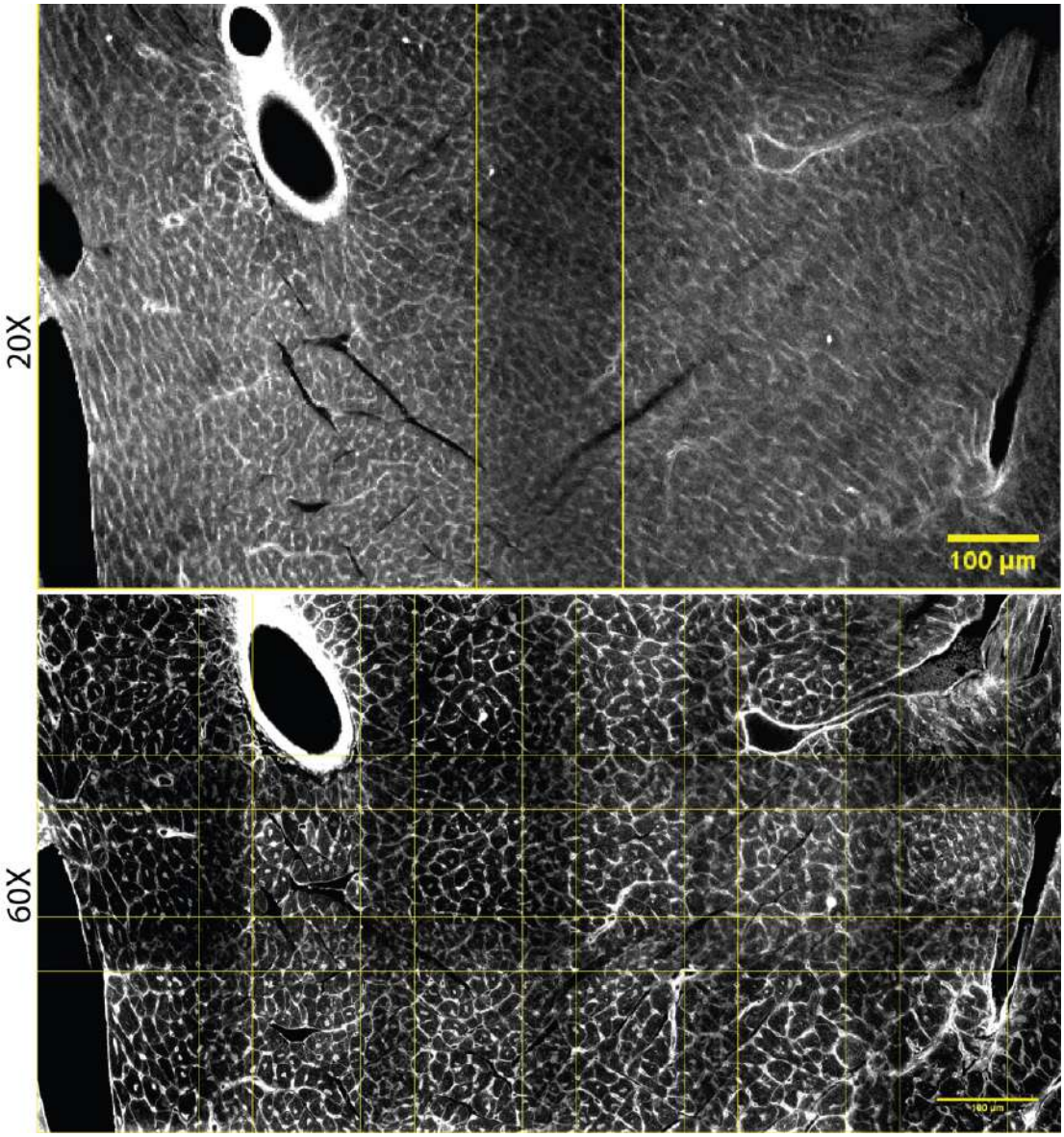

Figure 23: A comparison of 20X and 60X imaging.
Imaging using 20X (2-micron isotropic resolution) and 60X (0.663 X 0.663 X 0.79 µm^3 x, y, and z resolution, respectively) cleared heart tissue sections stained with WGA from the same tissue region. The area covered in two fields of view of 20X magnification is comparable to eighteen fields of view imaged at 60X.

c. Laser power detection and attenuation for in deep tissue imaging:

To test the laser power parameters, tissue samples were labeled with DAPI and AlexaFlour-640 tagged WGA for 405 nm and 488 or 640 nm excitation wavelengths, respectively. The signal intensity for the labeled tissue samples peaked exponentially with increasing laser power values, but the unstained tissue sample followed a linear intensity curve (Figure 24). This pattern confirmed that staining samples produced

efficient intensity measurements with a lower laser power value than unstained tissue. The unstained tissue section produced signal in both the 405 nm and 488 nm excitation wavelengths, but not in the 640 nm excitation wavelength. This is because the unstained tissue does not contain any fluorescent dyes, but shows autofluorescence in the 405 and 488nm excitation wavelengths. The 640nm excitation wavelength is suitable for signal specific from staining WGA tissue because it does not overlap with the autofluorescence wavelengths of unstained tissue.

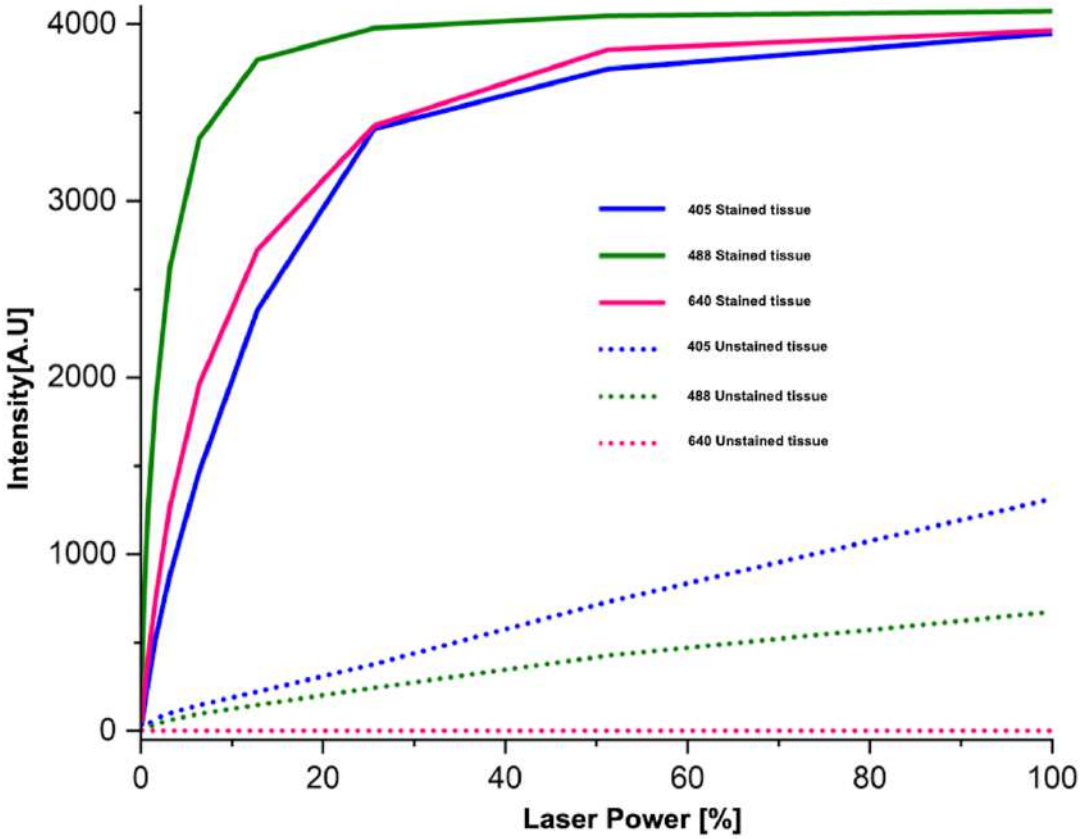

Figure 24: Laser power and signal intensity plot.
Laser power for stained and unstained tissue was increased(X-axis) and the intensity (Y-axis) was recorded in each laser power increment step. For staining DAPI, WGA-alexa flour 488/ 633 were used.

Laser power compensation can help to improve the signal-to-noise ratio (SNR) of images taken at depth. This is because the signal from deeper layers of tissue is typically weaker than the signal from shallower layers due to absorption loss. By increasing the laser power in the deeper layers, laser power compensation can help to improve the SNR and make it easier to see details in the deeper tissue. Laser power compensation can also help to reduce image artifacts caused by uneven illumination. This is because

the laser power is adjusted to compensate for the absorption loss at different depths, which helps to ensure that the illumination is more uniform throughout the image.

In addition to improving the SNR and reducing image artifacts, laser power compensation can also help to extend the depth of field of an image. This is because the laser power is adjusted to compensate for the absorption loss at different depths, which helps to ensure that all of the tissue in the image is in focus. In the Olympus FV3000 microscope settings, Bright Z™ settings for laser power compensation was applied to increase the signal as the deeper areas of the sample were imaged. This setting enables the tissue to be excited with more laser power in the deeper layers to compensate signal loss due to absorption loss (Figure 25).

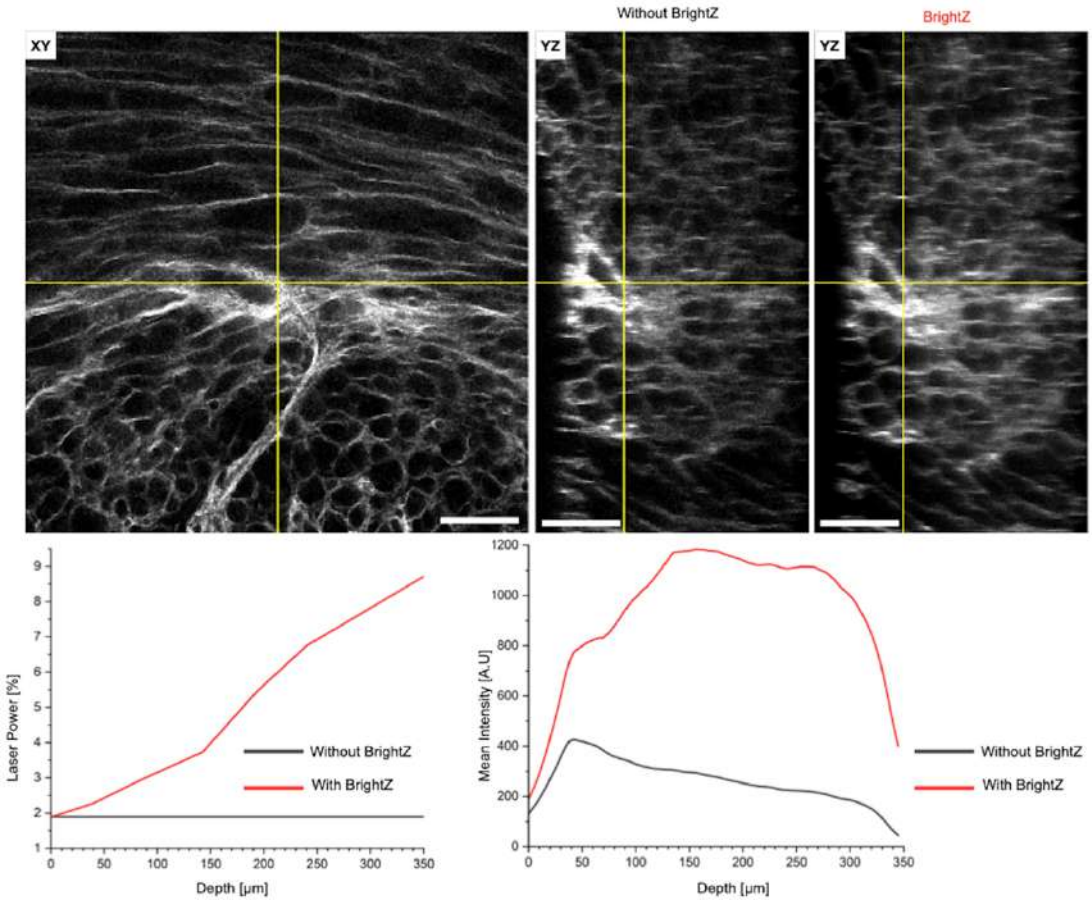

Figure 25: BrightZ correction and Z- axis profile of a field of view.
An example of how laser power compensation can be used to improve the quality of an image taken at depth is shown here. The image on the top middle panel is a confocal image of a mouse heart taken without laser power compensation or with a constant laser power. The image on the top right is the same image taken with laser power compensation. The image on the right has a much better SNR and is more uniform in illumination. The bottom left panel shows the laser power compensation values and bottom right panel shows mean intensity value over depth of imaging aka Z-axis profile. Scale bar - 100 microns.

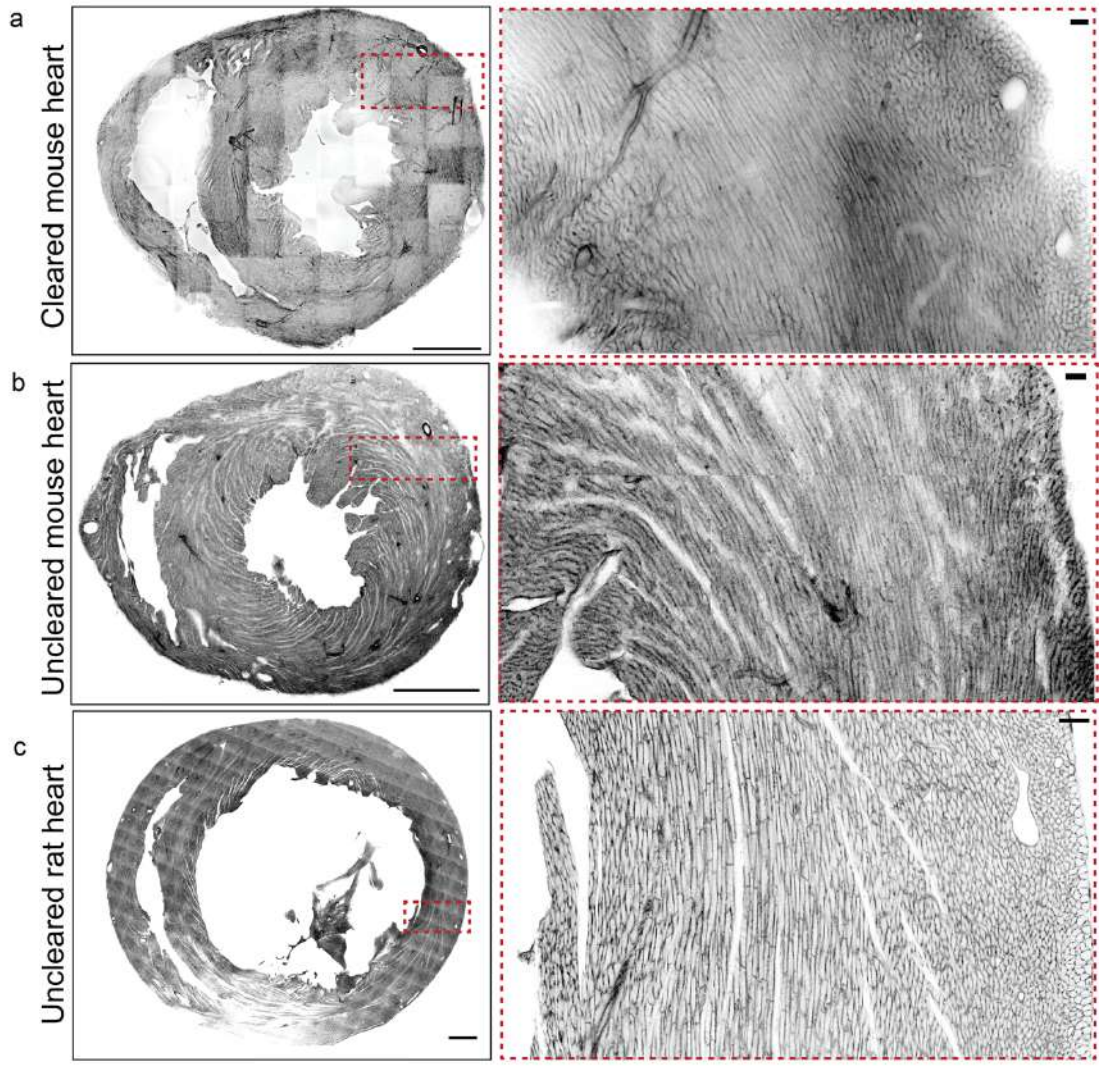

Figure 26: A comparison of cleared and uncleared heart tissue sections stained with WGA from a. cleared mouse heart b. uncleared mouse heart c. uncleared mouse heart. Scale bar is 1000 microns and 100 microns in full view and zoom in region respectively.

4.2 Reconstruction of cardiomyocyte orientation at the micron scale

Intact cleared hearts from wild-type mice were serially sectioned, stained with fluorescent wheat germ agglutinin (WGA) and subjected to confocal imaging to cover an entire section using individual fields of view (Chapter3-Methods, Figures 20 b and 27 b). The images were acquired at 2-micron isotropic resolution, such that only cardiomyocyte boundaries were captured (Figure 21 b). A comparison with uncleared heart images showed no significant alterations in the tissue due to clearing procedures (Figure 20). The images from cleared heart tissues were further processed to recover

micron scale resolution for each field of view and then stitched to obtain a full view of the entire section (Figures 27 b and 28).

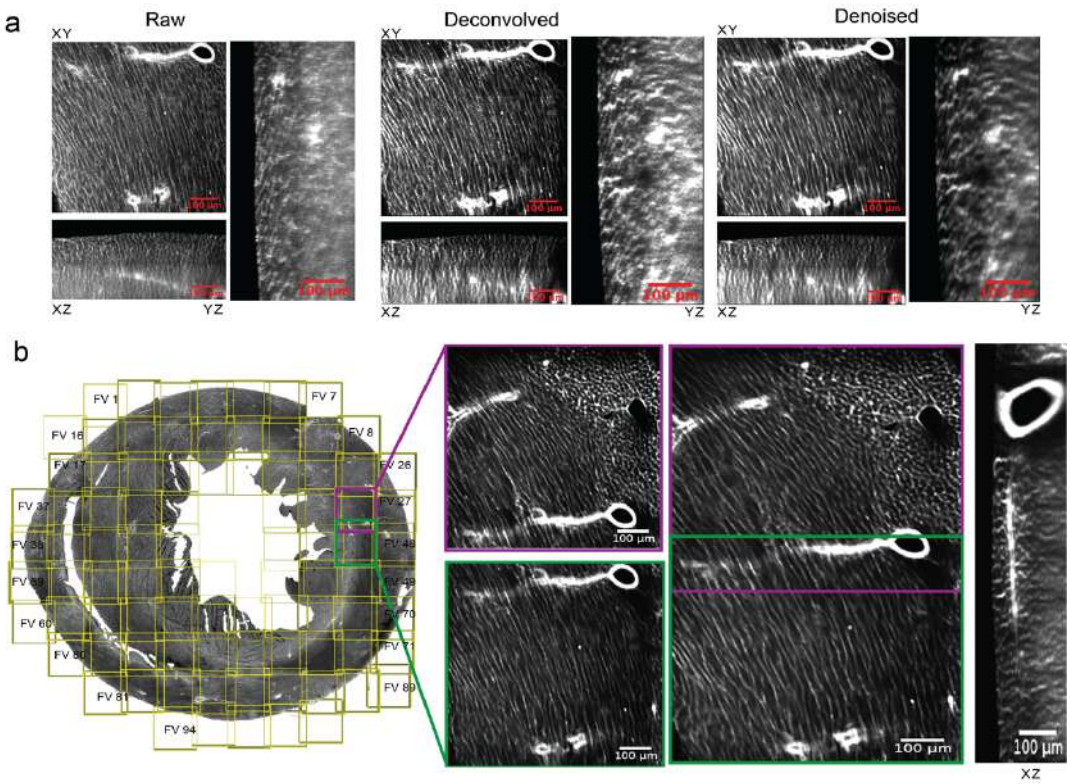

Figure 27: Preprocessing and stitching individual fields of view.
a. A representative field of view (left), followed by deconvolution (middle) and denoising (right). The orthogonal views (XZ and YZ) show an improvement in the signal to noise ratio towards the deeper Z-sections. The scale bar is 100 microns. **b.** Individual fields of view (FVs) overlayed as a grid on the reconstructed full short-axis section. The individual FVs were imaged using a snake pattern, row by row. Each FV is (320X2)microns^2 in dimension and has a 25% overlap with its neighboring FVs. **c.** Left panel; An example showing the stitching of two neighboring FVs ($_{FV}$28 and $_{FV}$47, shown in red and blue boxes, respectively). Middle panel; A zoomed in view of the stitched result, showing the alignment of features in the common region. Right panel; An XZ/YZ view of the common region. The scale bar is as indicated.

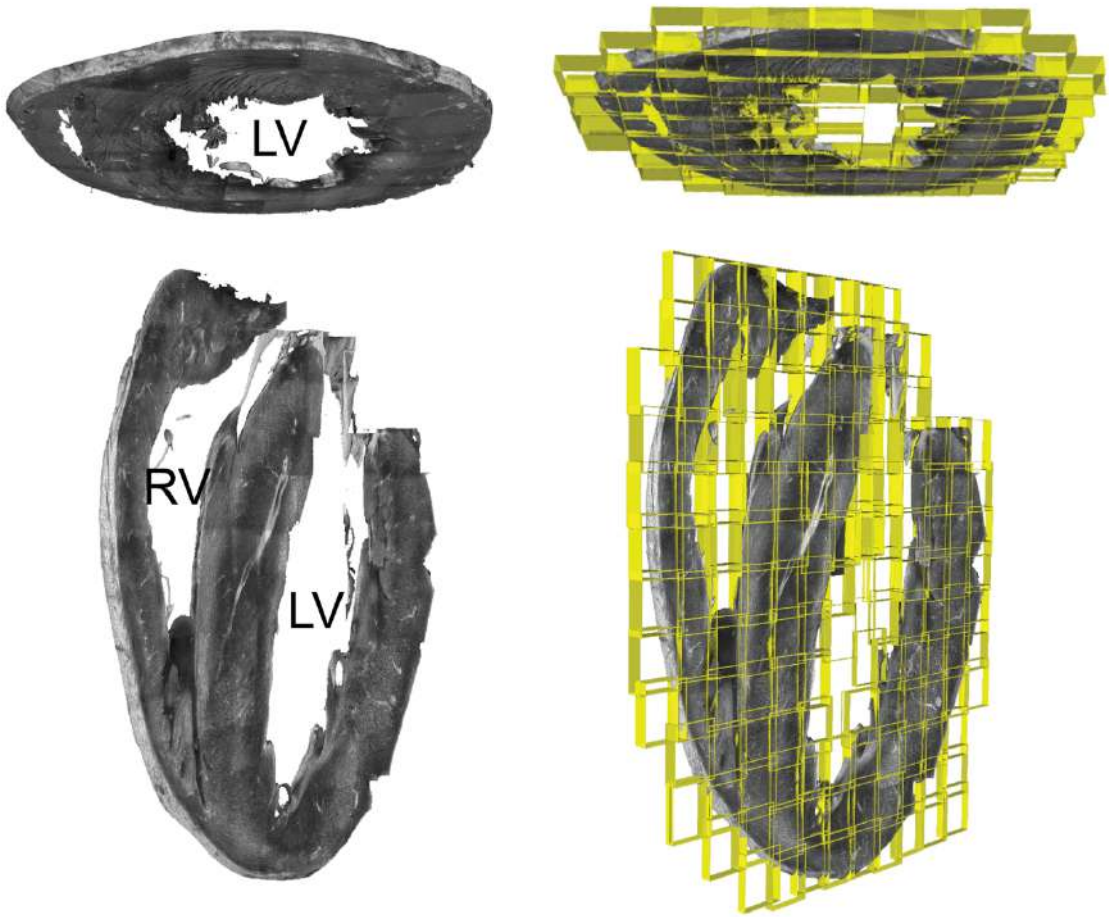

Figure 28: 3D view of tissue sections imaged (skewed).
3D-views of the stitched short-axis and long-axis sections, with the individual FVs shown in yellow in an overlayed grid pattern.

To validate our structure tensor calculations, the Fractional Anisotropy (FA) scores were calculated based on structure tensor eigenvalues, for the entire short-axis section and have found that the majority of the voxels have high FA scores. Figure 29 illustrates the confidence of our imaging method (i.e., resolving only cardiomyocyte) using a colormap and an FA distribution plot that shows that the structure tensor indeed consistently reveals an elongated cell type. To validate our automated structure-tensor orientation estimates, we compared them with hand-segmented orientation estimates and found a high degree of correlation between the two methods as a ground truth experiment (Figure 30). For validation we handpicked 70 cardiomyocytes from a randomly selected 3D image stack (field of view) here we did not bias the selection of cell types in any particular way. Cell-wise comparison revealed a close agreement between the ground truth and the structure tensor-based estimates of the orientations from the raw WGA images. For 70 hand-segmented cardiomyocytes, we observed an average difference of 5.6 degrees with a standard deviation of 2.86 degrees (Figure 30).

This allowed us to confidently describe cardiomyocyte orientation (represented as glyphs) spanning the entire section of heart tissue at a higher resolution than that provided by previous studies (Figure 31).

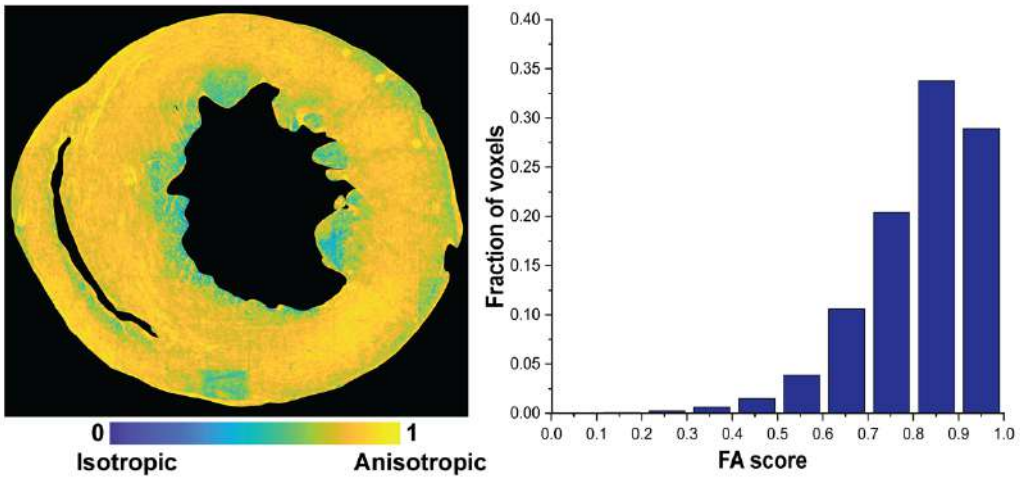

Figure 29: Fractional anisotropy analysis.
Fractional anisotropy scores are shown using a parula colormap (left) with a value in the range 0 to 1. The histogram (right) shows the fraction of pixels in each respective FA bin. The majority of the pixels have a high FA score, indicating the presence of dominant local orientations in the tissue stack. The color bar for the FA score is as indicated.

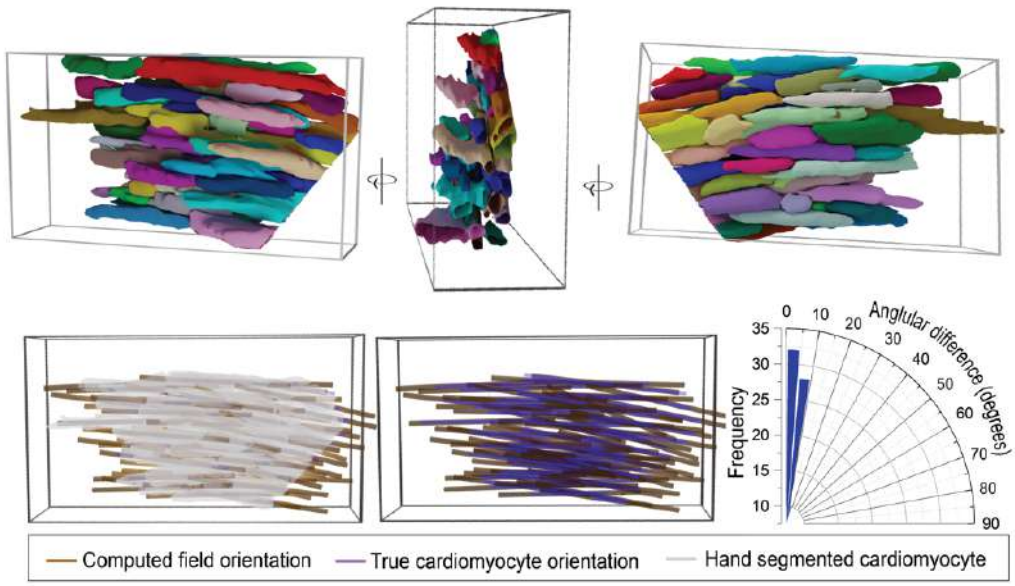

Figure 30: Ground truth experiment.
A representative 3D view of hand segmented cardiomyocytes (multicolored), ground truth orientation (purple) based on the second moment matrix for hand segmented myocytes (gray) and the estimated field orientation from the WGA image (golden

yellow) using a structure tensor approach (Methods). The mean difference between two ground truth and estimated orientations is 5.6±2.87 degrees.

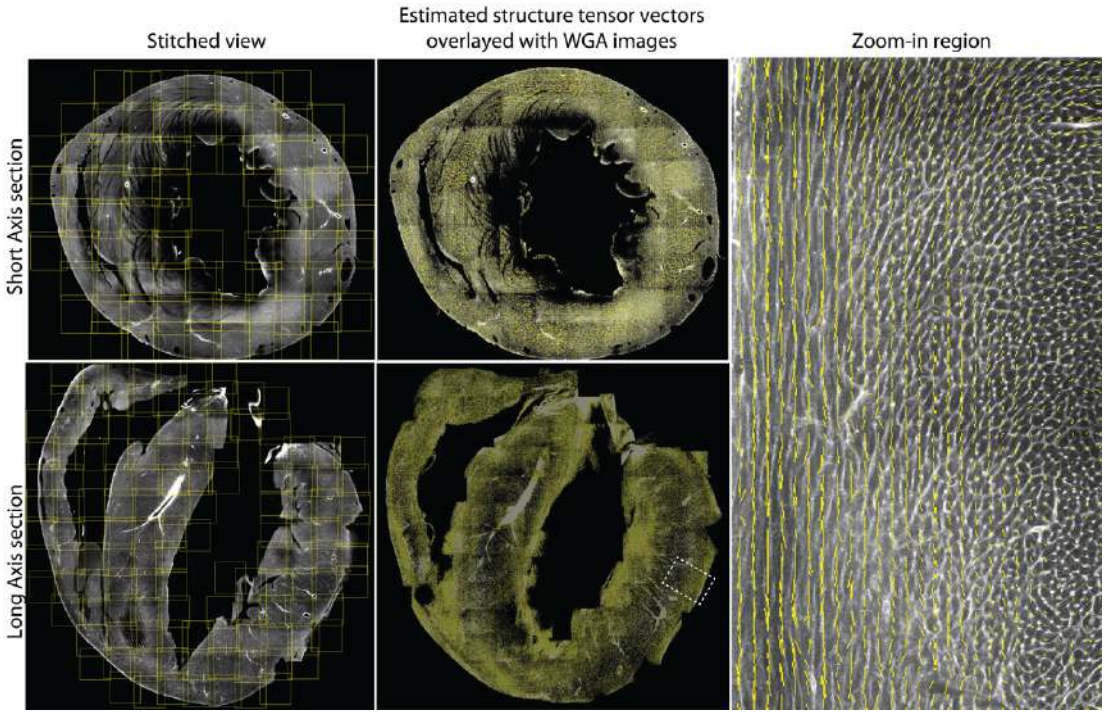

Figure 31: Overlay of structure tensor estimates on WGA.
Representative planes from both short and long axis views. Structure tensor estimates are shown in yellow and WGA shown in grey.

4.3 Regimes of discrete cell orientations across ventricular walls

A striking feature of the WGA-stained raw images is the appearance of discrete cell arrangements across the ventricular walls (Figure 27). To demarcate the boundaries between these different cell arrangements, we visualized θ, Φ (calculated in 2D, single plane representations) and αH angles (3D average values per tissue stack) defined in Figure 31 a using quantitative colormaps (Chapter 3 - Methods). The colormaps for the θ angle show that the component of the myofibers in the short-axis (XY) plane is perpendicular to the radial direction and follows a smooth continuum (Figure 31 b-d). Our findings at the micron scale are consistent with previous reports that the myofibers wind around the ventricles in a circumferential manner (20,28,30,71,72) .

In contrast to θ, the Φ colormaps reveal a discrete and significant change in cardiomyocyte orientation across the ventricular walls (Figure 31 b-d). The out-of-plane cardiomyocytes, shown in yellowish tones, form a crescent shape along the outer walls of both ventricles and an orbicular shape in the inner walls surrounding both the chambers (Figure 31 b-d). Taken together, these reconstructions show that the out-of-plane cardiomyocytes are aligned to form distinct bands of long-axis fibers in the outer

ventricular walls, that are orthogonal to the well-established circumferential myofibers. We analyzed five different datasets in short axis orientation to validate the obtained θ, the Φ colormaps keeping data set SAS3 as reference for tissue alignment (Figures 33 and 34).

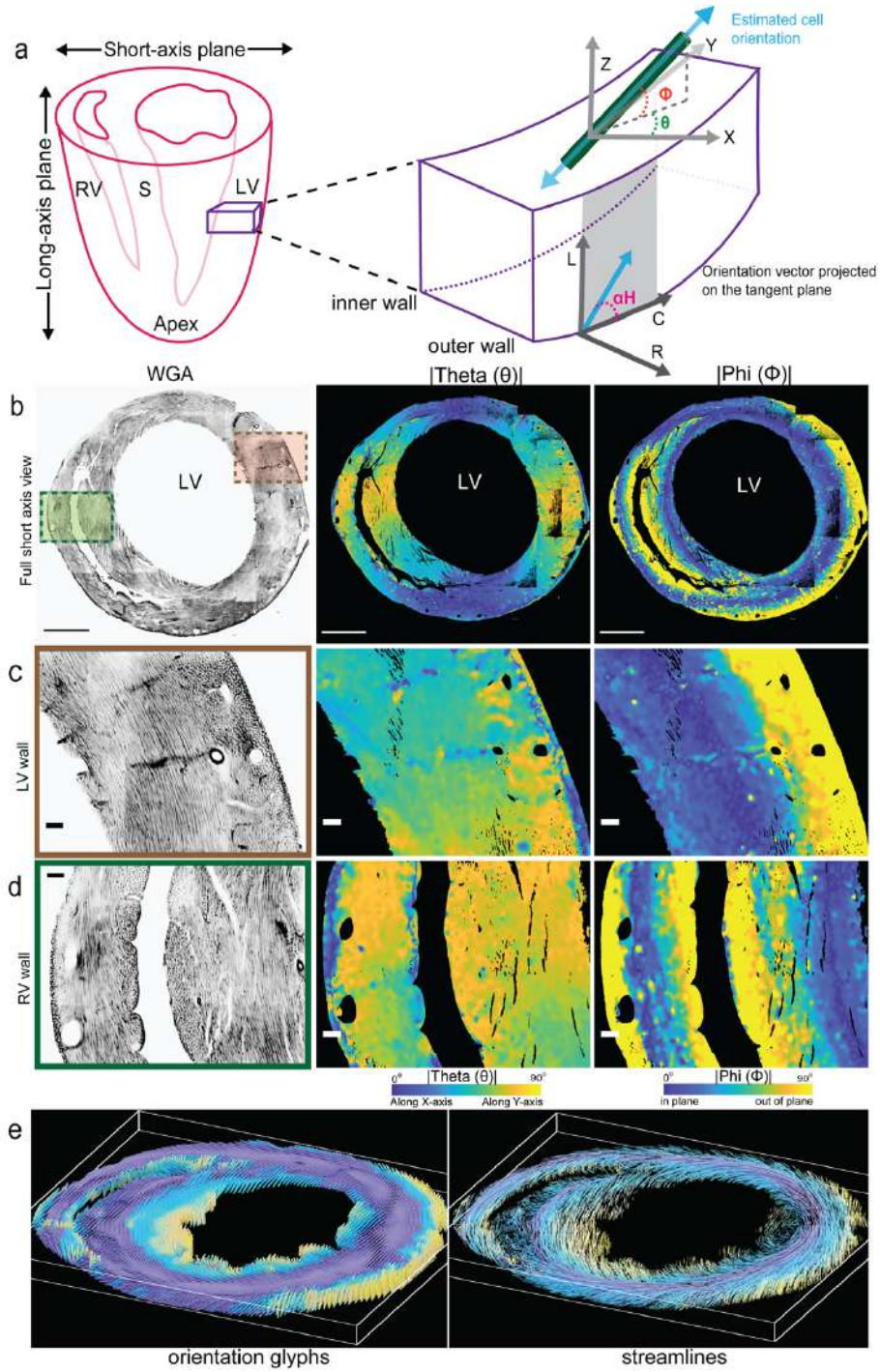

Figure 32: Cell orientation across a mid-ventricular short-axis section of the heart.
a. An illustration of the angles measured to represent the cell orientations across the ventricular walls. The red box represents a magnified view of the ventricle wall, with the global axes and labels as indicated. The green cylinder and the blue bi-directional arrow represent the cardiomyocyte and its long-axis, i.e., the estimated cell orientation,

respectively. Φ is the angle between the global Z-axis and the estimated cell orientation. θ is the angle between the projection of the estimated cell orientation onto the XY plane and the X-axis direction. αH, the helix angle, is the angle between the projection of the cell orientation on to the plane perpendicular to the transmural penetration direction and the circumferential direction. **b-d.** A magnified view of the right (green rectangle) and the left (magenta rectangle) ventricular regions for a full view of the WGA stain (middle). The θ and Φ angles for the mouse SA sections are shown using a parula colormap. The yellow tones for the θ angle represent cell orientation along the global Y-Axis, while the blue tones represent cell orientation along the X-axis**.** For Φ, the yellow and blue tones represent cells in-plane and orthogonal to the global Z-axis, respectively. The colormaps scale with the angles, as indicated. The scale bar for B is 1000 microns and for C and D is 100 microns. **e.** Structure tensor-based orientations are visualized as glyphs (middle) and streamlines (right) (Methods). The colors follow a parula colormap, where the blue and yellow tones indicate orientations that are in or out of the short-axis plane, respectively.

4.4 Sharp changes in myocyte orientation at ventricular wall boundaries

In the short-axis sections, the Φ and αH angles are related to myofiber orientation with respect to the viewing plane. αH has been widely used to capture orientation changes along a transmural penetration from the outer to the inner heart wall. We therefore computed αH at the micron scale using a ventricular outer boundary-based estimate of the radial penetration direction at each location in the left ventricular wall (Chapter 3-Methods; Figure 35). The average αH values for several pie-shaped sectors are plotted as a function of penetration depth (Figure 35). The patterns of αH values appear to be very similar at fixed angular distances away from the lateral regions (Figures 35, 36 and 37). Sectors in the vicinity of the antero/infero lateral regions on the short-axis section reveal a sharp drop of about 20 degrees within the first 50 microns near the circumference of the outer wall. Immediately after this sharp decline, αH undergoes a gradual increase of about 180 degrees for the remainder of the left ventricular wall, in a manner that is linearly proportional to penetration depth (Figure 35 b). This latter smooth transition of αH through the myocardium (middle wall) until the endocardium (inner wall) is consistent with earlier findings (68,73–78). However, the initial sharp transition of an approximately 20 degrees change in αH, in the outer wall, is an entirely new discovery (Figure 35 b). We hypothesize that earlier studies lacked the required spatial resolution to identify this sharp transition in αH.

To test this, we averaged the structure tensor, estimated at the micron scale, to a coarser spatial resolution, resulting in a pseudo-low-resolution estimate of myofiber orientation

(Figure 35 b). This orientation estimate is qualitatively equivalent to the millimeter or sub-millimeter scale of DT-MRI studies. A comparison of our micron scale and pseudo low-resolution αH angle estimates indeed shows the disappearance of the sharp change near the outermost layer, at the simulated coarser resolution (Figure 35 b). The long-axis myofiber layer we have discovered in the outer ventricular wall might have remained obscure in past studies due to its narrow width of only approximately 50 microns. As such, in our simulated sub-millimeter scale coarse voxel analysis, it disappears in the orientation plots (Figure 35 b). All the αH plots of similar regions show similar trends, as determined by both the colormaps and more detailed orientation plots, across successive short-axis sections taken near the mid-cavity region and as well as across a different mouse heart (Figure 36 and 37). In addition, our pre-processing pipeline (deconvolution and denoising) helped to improve SNR at the deeper layers, as evident from the raw versus pre-processed comparisons shown in Figure 38 a. The rate of change of the Helix angle in Figure 38 b-c, along with the transmural penetration, highlights the sharp change in orientation near the outer boundary of the LV. A similar sharp change of αH values can be observed at outer RV wall (Figure 39). Our reconstructions also demonstrate the presence of narrow long-axis myofiber layers in the inner ventricular chamber and septum walls, that have been described in previous studies involving histological sections (30,75,79–81).

These additional examinations provide conclusive evidence that the outer and inner walls of both the left and right ventricles and the septum contain a thin layer of orthogonal myofibers, i.e., ones that run in a direction that is perpendicular to the short axis plane.

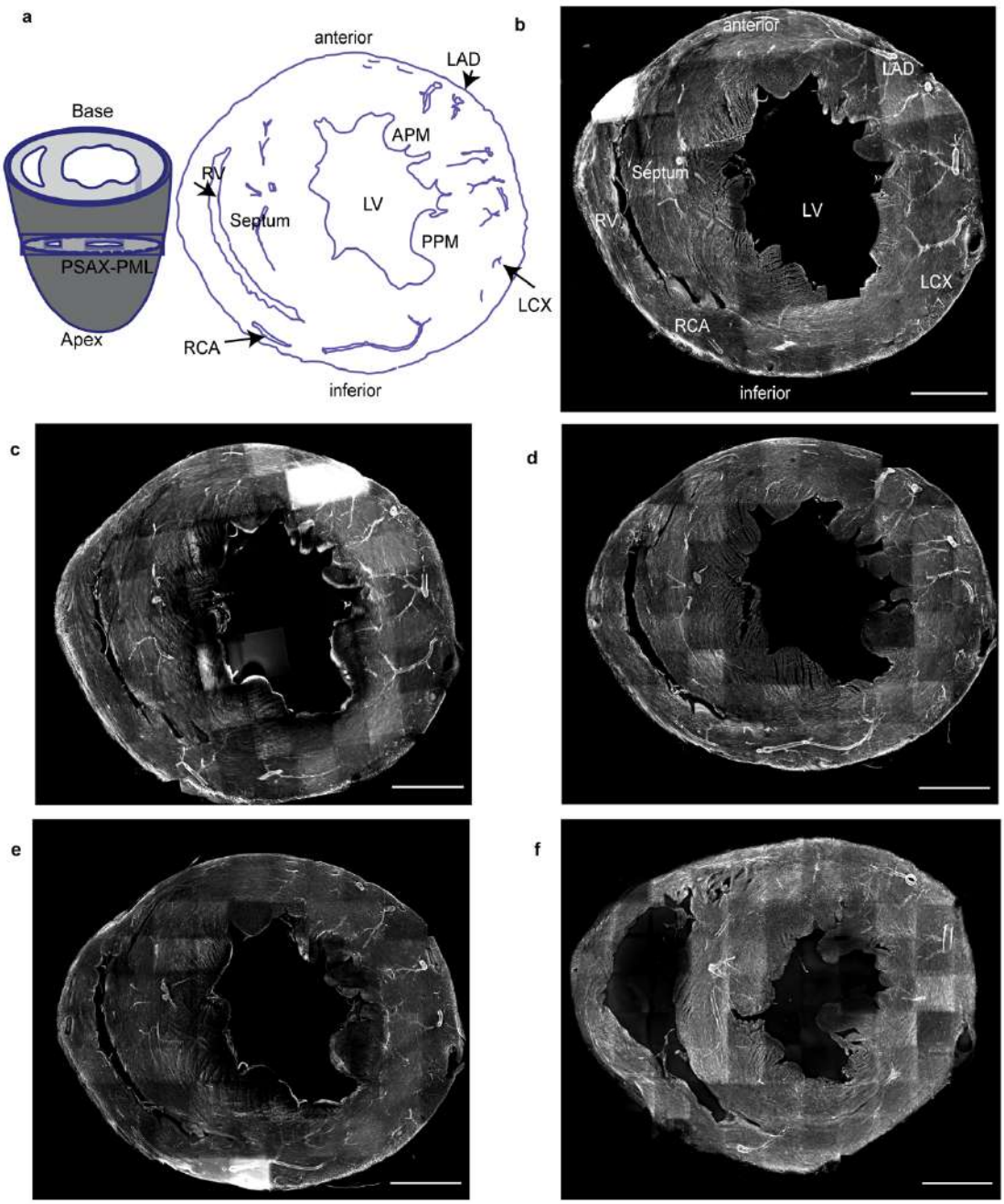

Figure 33: AHA segmentation and tissue alignment.
a. Boundaries of the short-axis sections (PSAX-PML section) from a WGA maximum intensity Z-projection, with labels as illustrated. Using the major arteries, blood vessels and papillary muscles in the LV chamber, the anterior and inferior orientations were aligned for the different short-axis sections. RCA- Right Coronary Artery, LCX- Left Circumflex Artery, LAD- Left Anterior Descending Artery, APM- Anterior Papillary Muscle, PPM-Posterior Papillary Muscle, RV-Right ventricle, LV-Left Ventricle. **b-f**. The aligned datasets are shown as maximum intensity projections of the WGA stain images. The scale bar is 1000 microns.

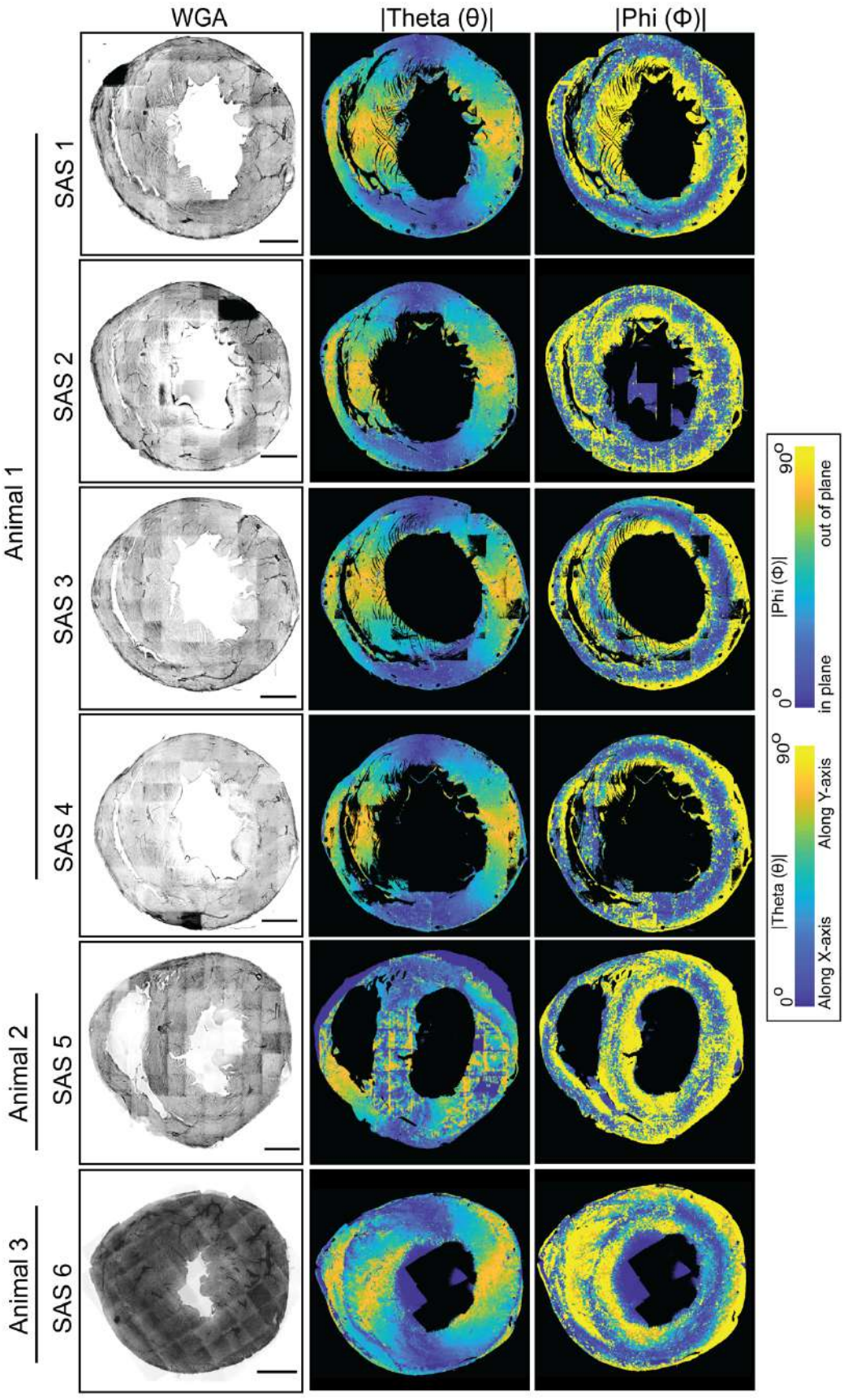

Figure 34: WGA staining and angular colormaps of different short-axis sections.
A maximum intensity Z-projection of the WGA-stained short-axis section from different mouse hearts as indicated, shown in grayscale, with the Φ and θ angles for cell

orientations shown using parula colormaps, with the color bars as indicated. The scale bar is 1000 micron.

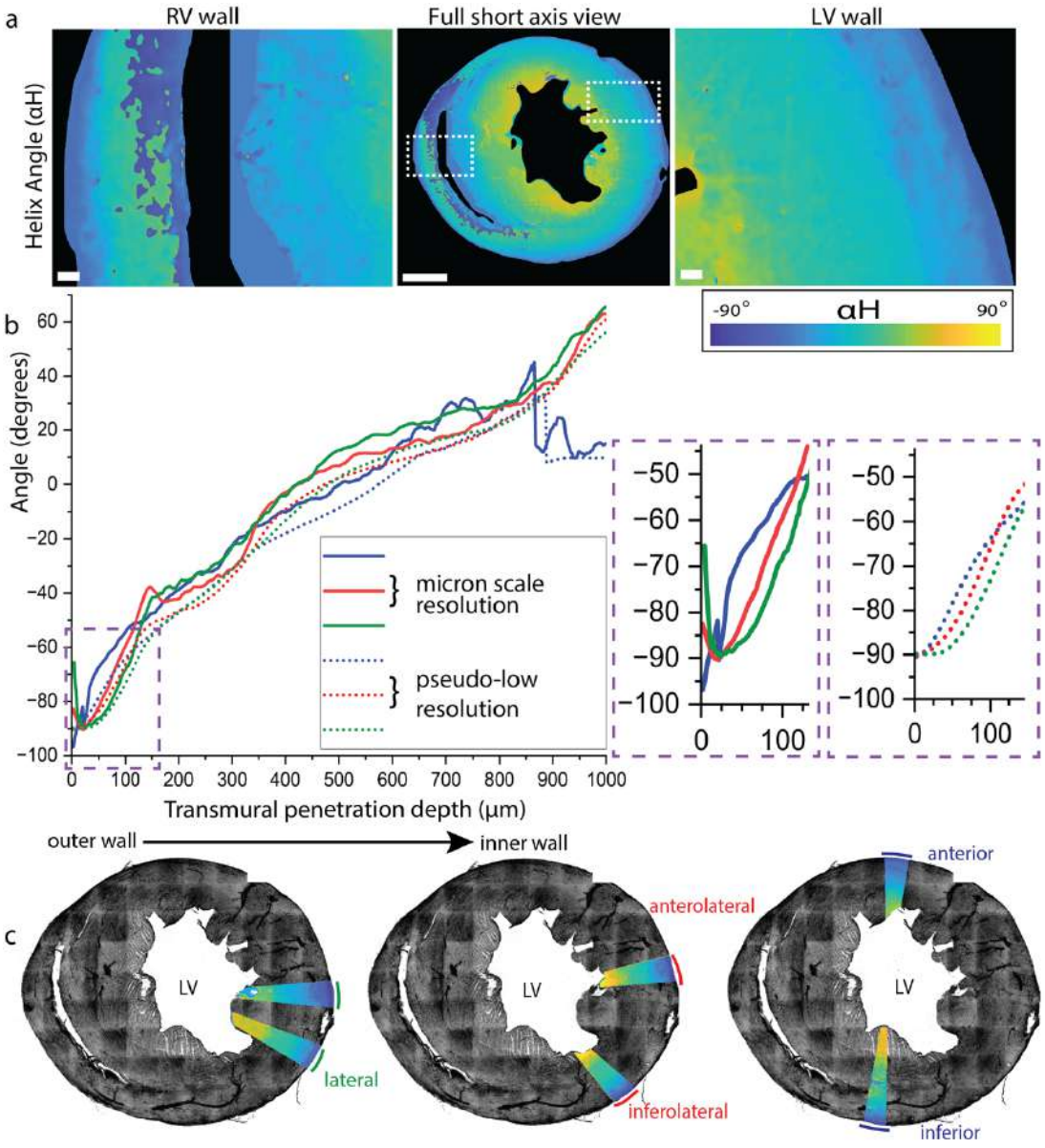

Figure 35: Helix angle changes across ventricular walls.
A magnified view of the right (RV wall) and the left (LV wall) ventricular regions for a full view of the HA map (middle). The individual 10° pie shaped sectors were combined into three groups; anterior/inferior, lateral, anterolateral and inferolateral, The pie-sectors average αH values were plotted are highlighted as αH colormaps on a maximum intensity Z-projection of the WGA-stained short-axis section in grayscale. **f.** The average αH values* from micron-scale and pseudo-resolution analyses of the selected pie-shaped sectors of the LV region from one representative data set of a short-axis section (SAS3) is shown to the right. The αH values are plotted as a function of the penetration depth, depicted as distance in microns along the X-axis from the outer to the inner walls.
* The values plotted here derive from combining two sectors, spanning 10 degrees in each sector selected from a representative data, as illustrated.

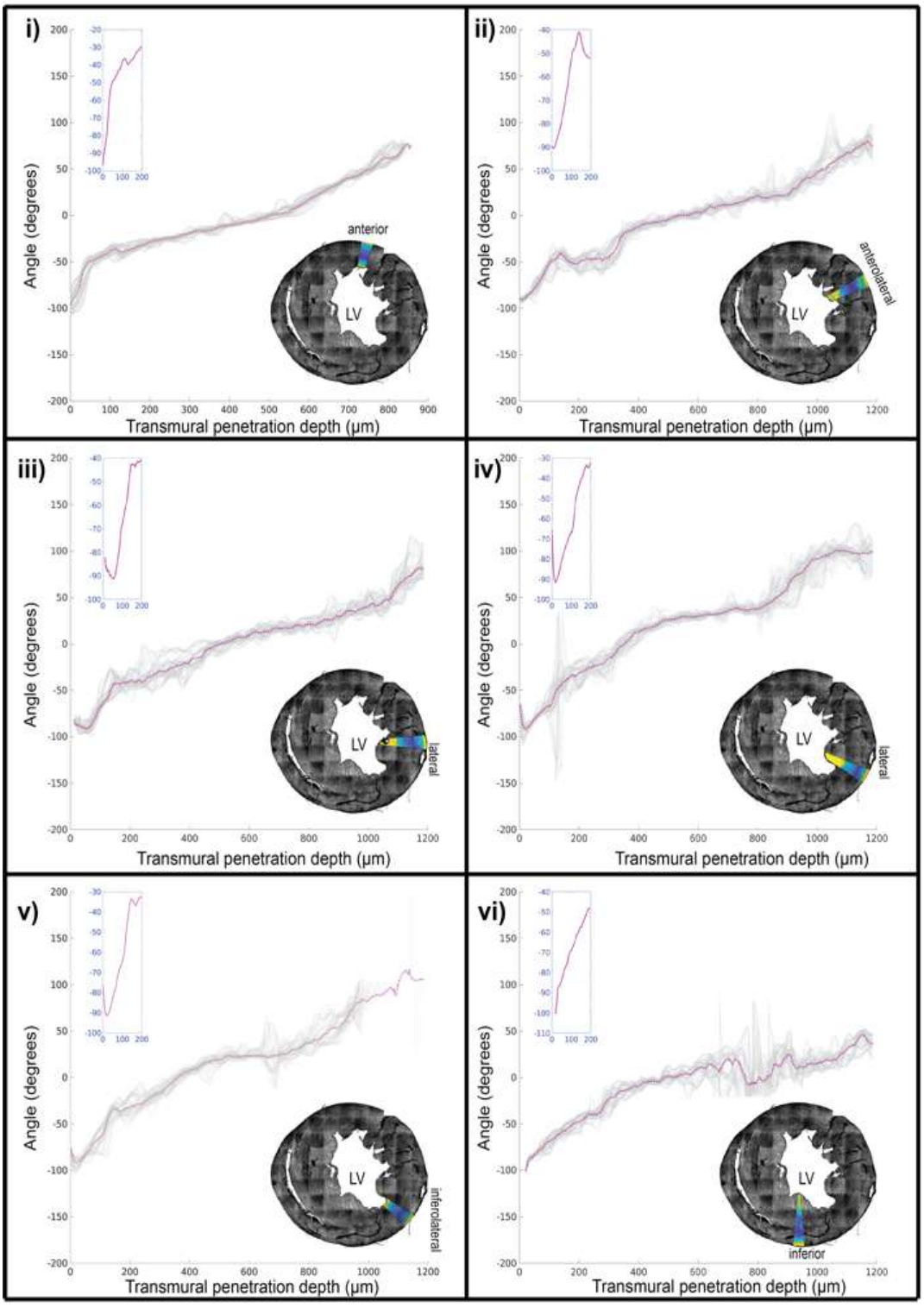

Figure 36: Variation of αH from the outer to the inner ventricular walls.
An examination of αH in a short-axis view of a mouse heart ventricle, sectioned at the PSAX-PML (parasternal short-axis – papillary muscle level (lower right of each panel). The αHvalues of selected pie-shaped sectors* of the LV region from one representative data set of heart sections (SAS3) are plotted as a function of the penetration depth from the outer to the inner walls. Penetration depth is depicted as distance along the X-axis. The mean αH is plotted as a dotted magenta line and the αH measurements along

distinct penetrations are shown in gray. *The values plotted here derive from sectors spanning 10 degrees each, as illustrated.

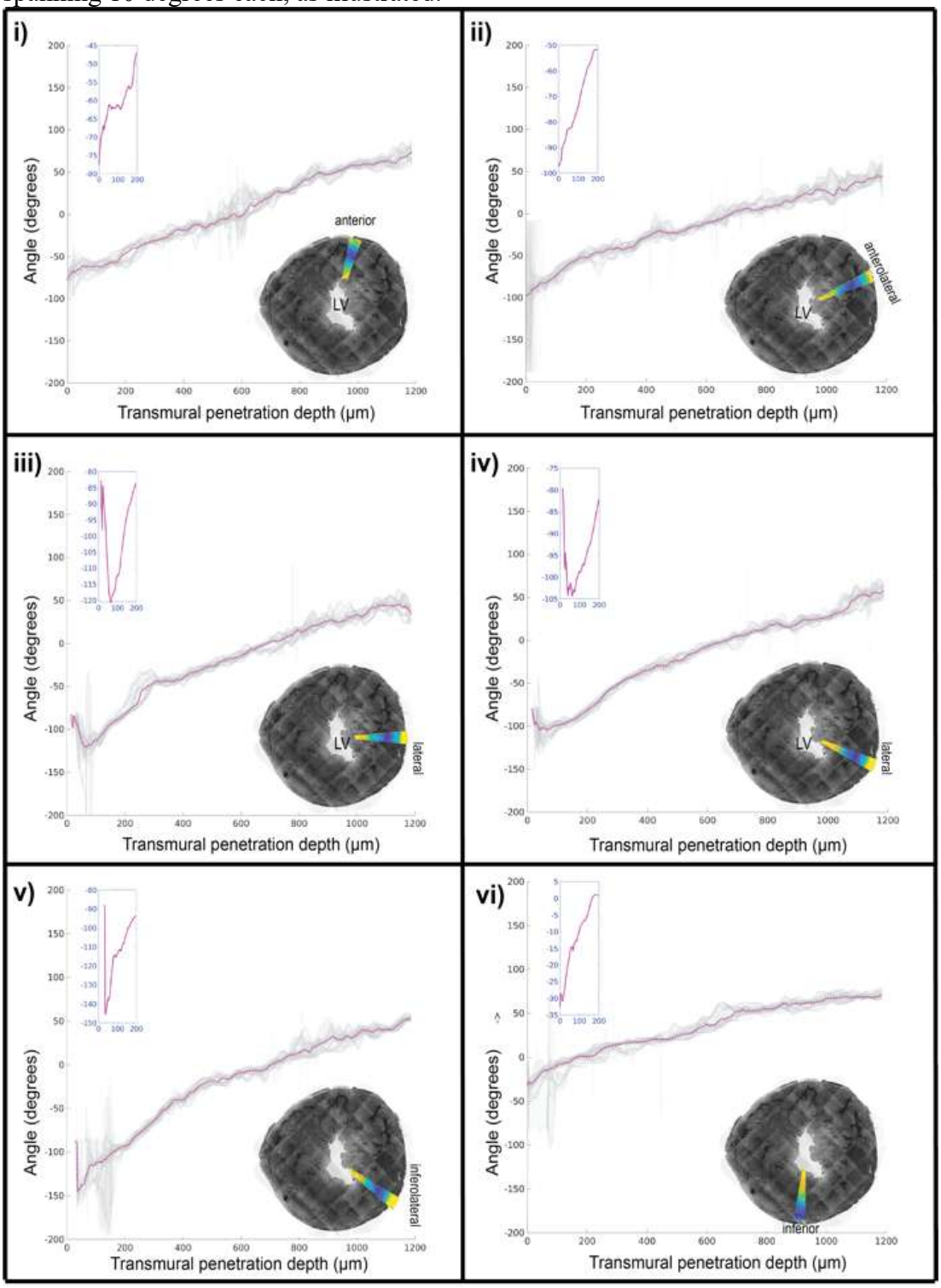

Figure 37: αH plots from the subsequent section, dataset SAS5.
Custom pie-shaped sectors of the ventricular walls are selected. Each sector spans 10 degrees and is overlayed as a magenta wedge on a maximum intensity Z-projection of the WGA stain at the bottom right of each panel. The αH values are plotted along the penetration from the outer to inner walls, depicted using distance in microns along the X-axis. The mean is highlighted as a magenta curve in the plots and a zoomed in version of the outer-ventricular region is provided at the top left of each panel.

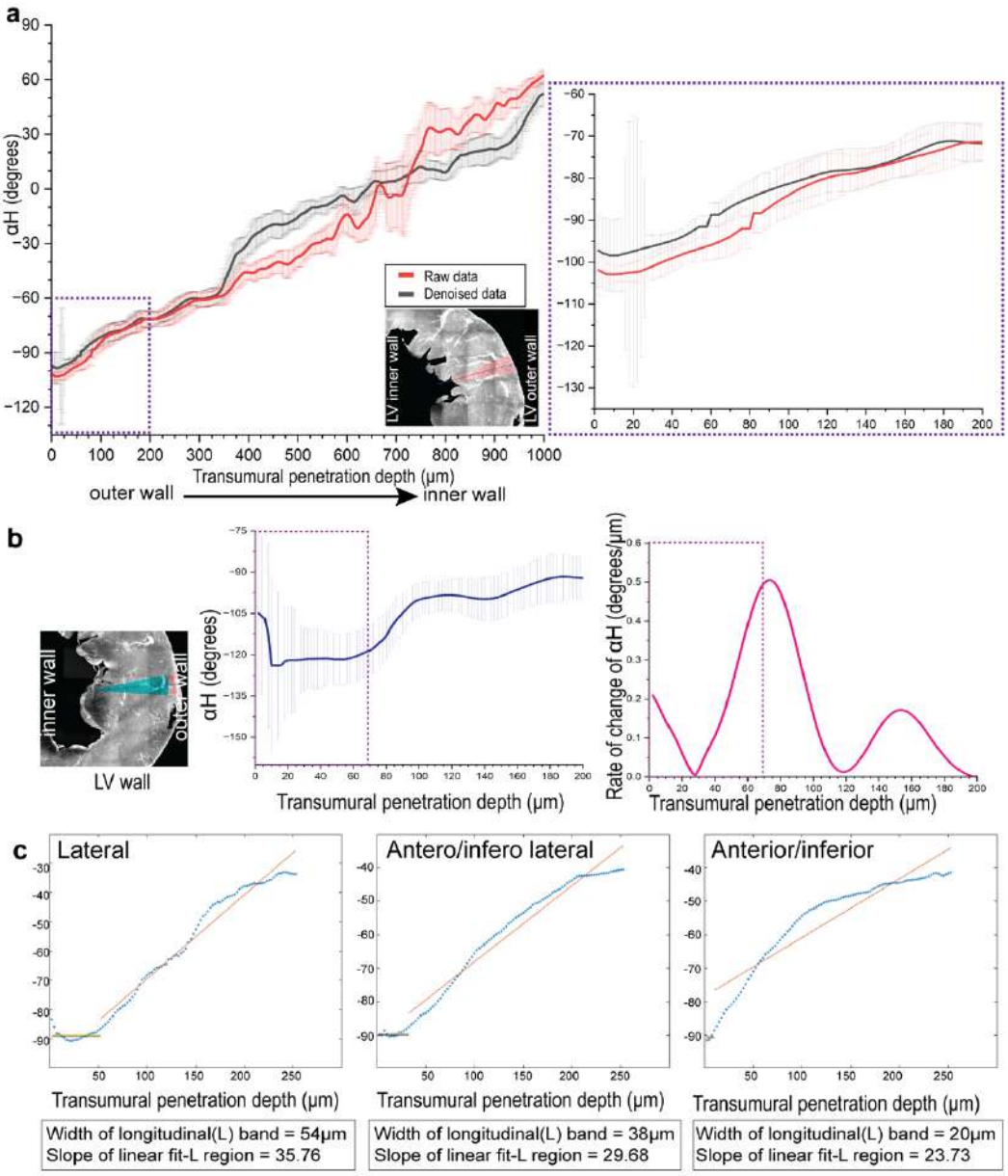

Figure 38: Significance of preprocessing steps in improving the SNR and analysis. **a.** αH estimates from a represenntative raw (red line) and denoised short-axis section image stacks (black line) are shown for comparison. The region of the LV wall analyzed is shown in the bottom left panel, with a zoom in on the first 200 microns on the bottom right. The transmural penetration direction is from the outer to the inner LV wall. The raw data agrees with denoised αH estimates in most of the places, however, we observed that estimation was much more consistent and robust to non-uniform illumination changes with denoised data. The intensity between two fields of view 4.5 Distinct outer wall cell layers of the left and right ventricular walls are continuous from apex to base (~350 microns in transmural penetration depth) the αH estimates begin to deviate marking the edges. **b.** αH plot (left), region of LV wall analyzed (middle) and rate of change of αH calculated over a neighborhood of 15 voxels. The region marked by a dashed box represents the outer wall long-axis cells, where the rate of change of αH is initially small and then increases sharply as one approaches the middle wall region, after which it plateaus and then increases again. **c.** Line fits for αH plots were calculated

for the lateral, antero/infero lateral and anterior/inferior regions, with the extent of the outer wall long-axis cells shown by length of the first line in each plot.

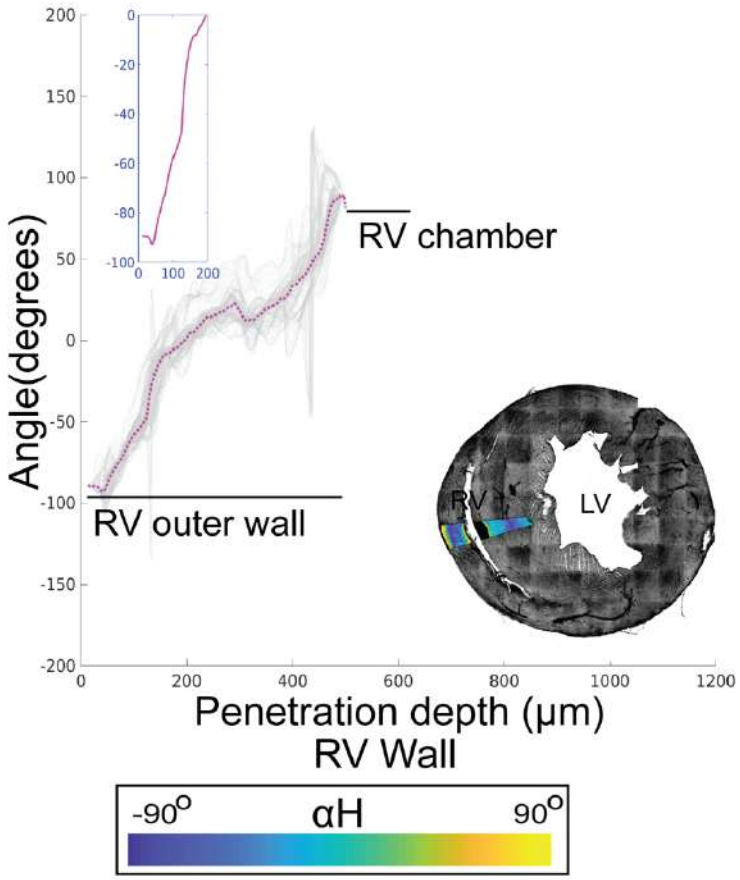

Figure 39: Average helix angle plots from outer to inner wall of the right ventricular wall.
The individual pie shaped sector that was averaged are overlayed using a parula colormap on a maximum intensity Z-projection of the WGA-stained short-axis section in grayscale (middle right).

4.5 Charting the continuity of the orthogonal myofibers

The analysis of short-axis sections allowed us to identify narrow bands of myofibers near the boundaries of the ventricular walls that are aligned to the long-axis direction of the heart (Figure 32). To determine the spatial extent of these myofibers across the entire length of the ventricular walls, we turned our attention to the analysis of long-axis sections (HLA-4C). Here the angle with the longitudinal axis, depicting the component of cardiomyocyte orientation in the XY plane, shows a smooth transition, similar to that in the mid-ventricular short-axis sections (Figures 40 and 41). In the colormaps of angle with longitudinal axis we show this layer in yellow tones, and it is evident that it extends all the way to the apex (Figures 40 and 41).

Those from the left ventricle outer wall are connected to the right ventricle outer wall and inner chamber walls (Figure 42). Thus, the entire long-axis myofiber system along with the endocardium longitudinal fiber forms a continuum from the ventricles to the apex (Figure 43) one that is structurally distinct from the circumferential system. We confirmed that the outer wall cells we refer to are indeed cardiomyocytes, as shown by the presence of sarcomeric structures with the help of alpha-actinin staining (Figure 44). In closing, we have discovered an entirely new long-axis fiber system in the outer wall of the heart (Figures 40-43).

4.6 Orthogonal cell-layers converge at the apex

In order to visualize the continuation of long-axis fibers at the apex, we extended our sectioning towards the apex region along the short-axis plane. At the apex, these long-axis fibers turn upwards towards the base of the heart and then continue to the adjacent boundaries of the heart wall forming a confluence (Figure 45). The bands of long-axis myofibers extend, intertwine, and continue into the opposite ends of the ventricular walls forming a complex geometry emerges near the apex region (Figure 45).

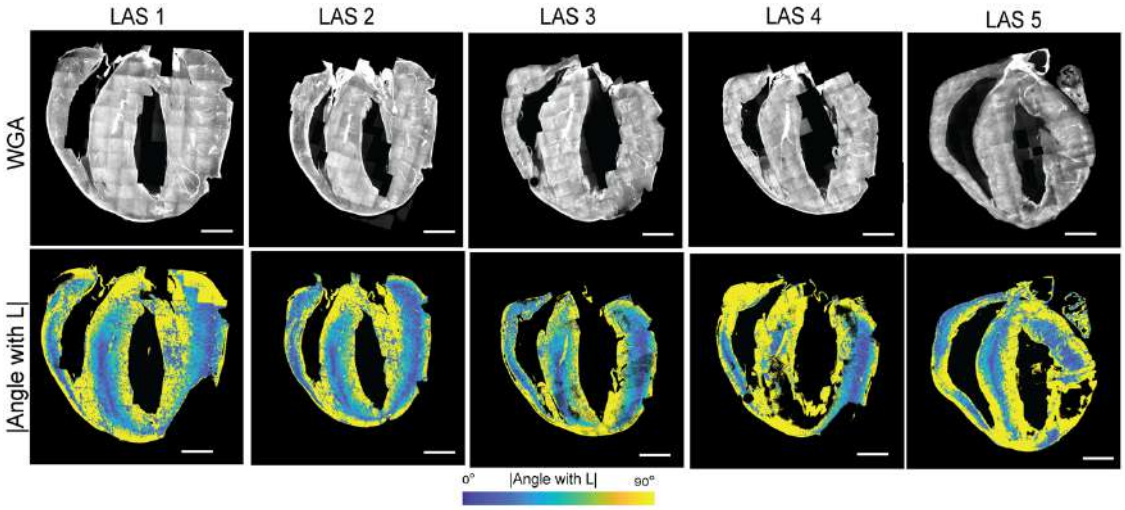

Figure 40: WGA staining and colormaps for magnitude of the angle with the longitudinal axis for different long-axis sections.
Five mouse heart ventricle long-axis sections are shown as maximum intensity Z-projections of the WGA stain, with the magnitude of the angle between the aggregate cell orientation and longitudinal axis shown with a parula colormap. The colorbar is as indicated, and the scale bar is 1000 microns.

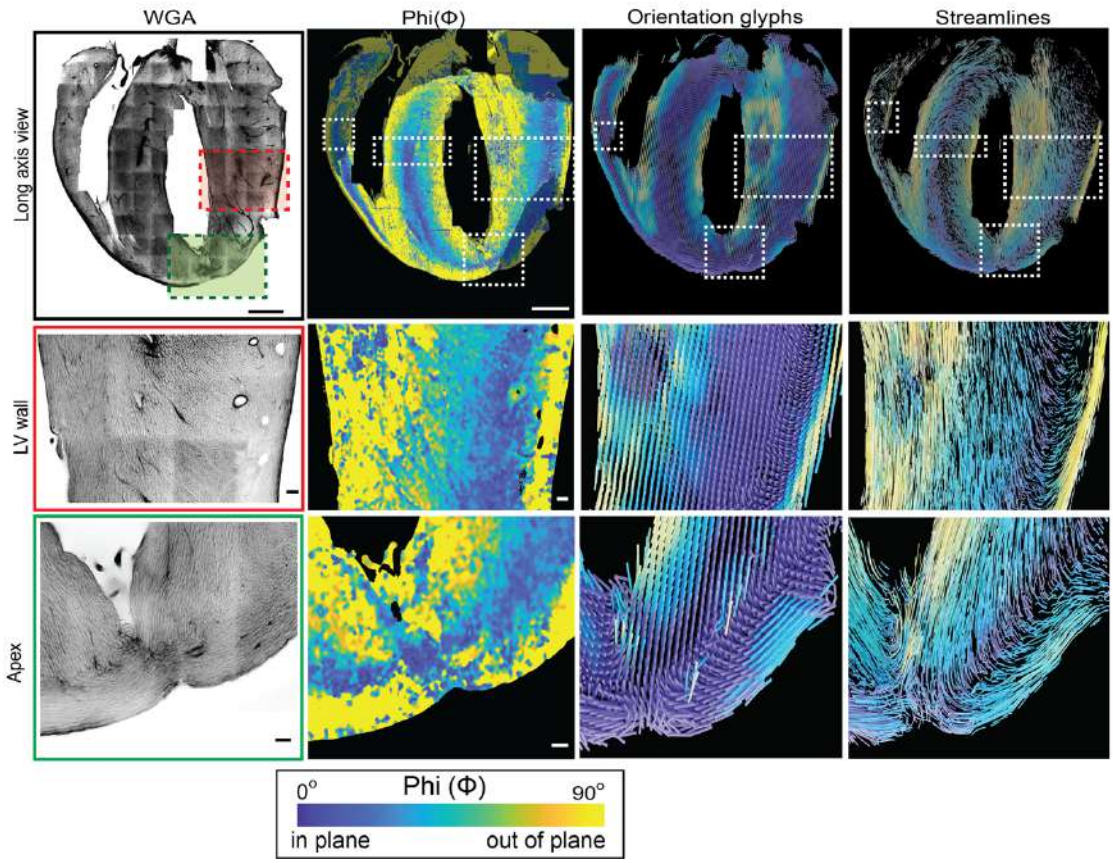

Figure 41: A detailed view of a long-axis section.
First column-WGA stain, second column-angle with long axis colormaps, third column-Estimated orientations as glyphs fourth column - Estimated orientations as streamlines. The colors follow a parula colormap, where the blue and yellow colors indicate in- and out- of short-axis plane cell orientations, respectively. Magnified views of the left ventricle (2nd row) and the apex region (3rd row) are shown for the regions in panel A. The color bar for the Φ angle is as indicated. The scale bar for the complete view is 1000 microns and for the zoomed in regions is 100 microns.

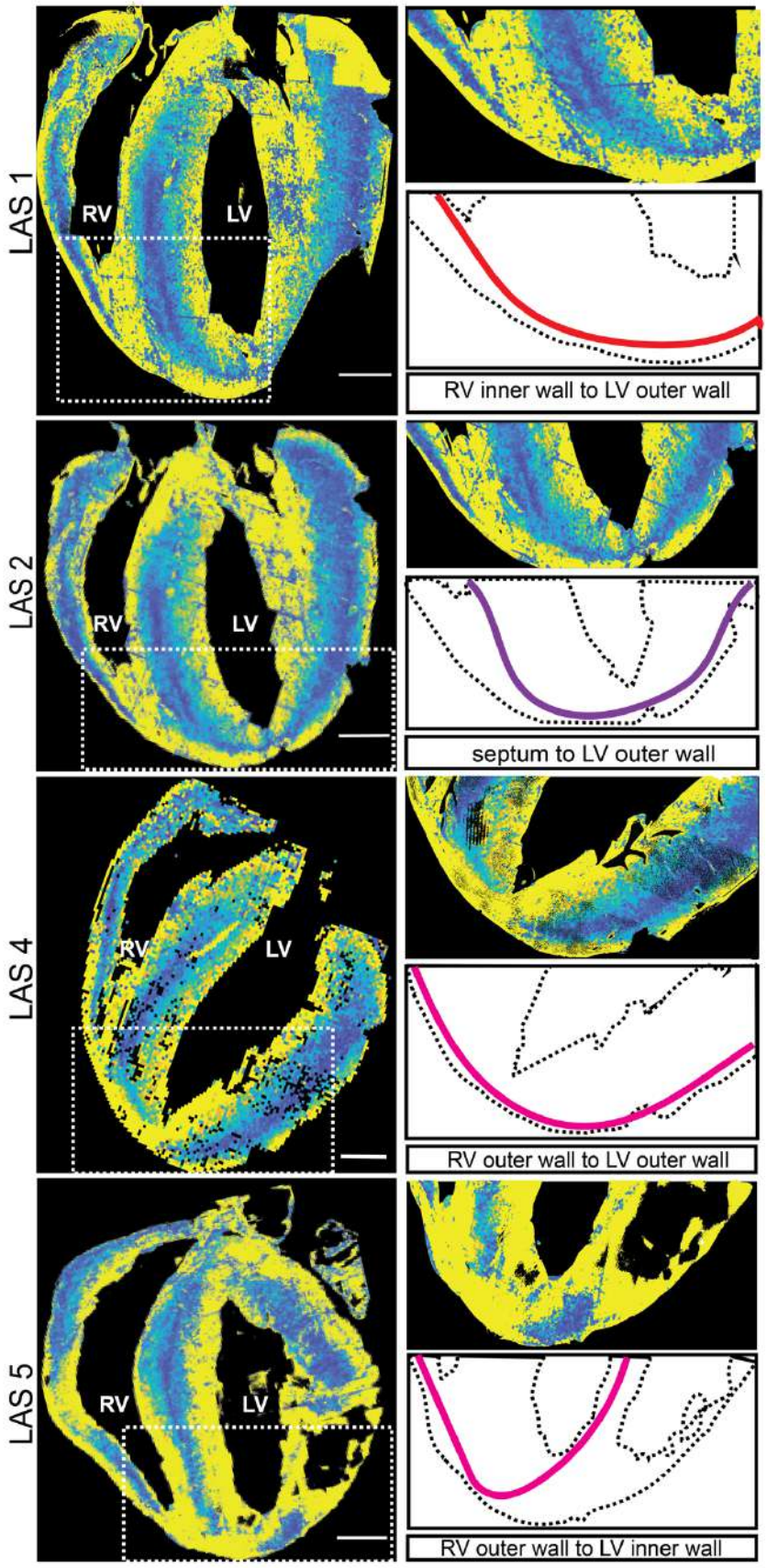

Figure 42: The angle with long axis colormaps of different long-axis sections and their connections at the apex.

Five mouse heart ventricle long-axis sections are shown as the angle with long axis of cell orientation shown with a parula colormap marked with a white dotted box highlighting the apex region under consideration (left column). A zoomed in view of the highlighted apex region from the respective long-axis sections and illustration of long-axis connections between different ventricular walls (right column). The continuity of the long-axis fibers from the septum to the left ventricle outer wall, from the right ventricle inner wall to the left ventricle outer wall, from the right ventricle outer wall to the left ventricle outer wall and from the right ventricle inner wall to the left ventricle inner wall, is highlighted in first, second, third and fifth row**,** respectively. The color bar is as indicated, and the scale bar is 1000 microns.

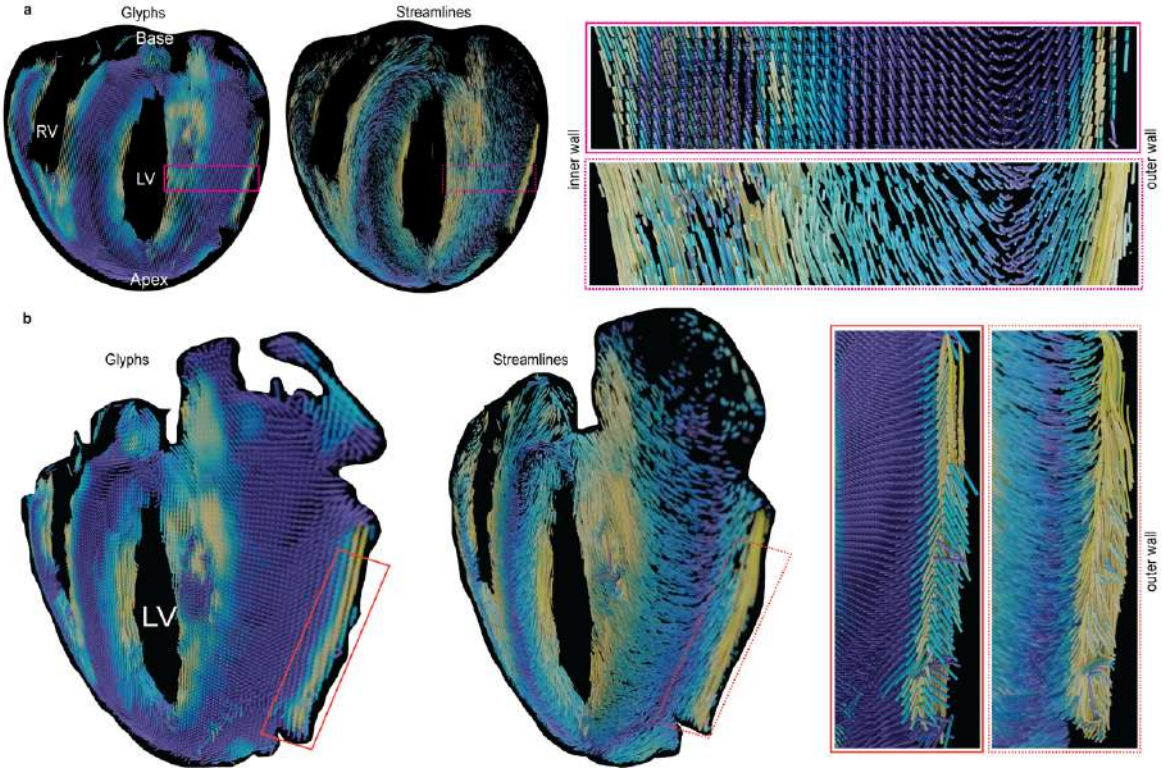

Figure 43: Evidence for a long-axis fiber continuum from the analysis of a long-axis section.
Estimated aggregate cardiomyocyte orientations are shown as glyphs (**a**) and streamlines (**b**) for the mouse LA sections. In each panel, a 3D visualization of the orientations is shown using either glyphs or streamlines, with a view obtained by rotation in a clockwise direction shown on the right (Methods). The colors follow a parula colormap, where the blue and yellow tones indicate cell orientations that are in and out of the short-axis plane, respectively. These visualizations reveal the continuity of cell orientations across the entire long-axis section, from base to apex.

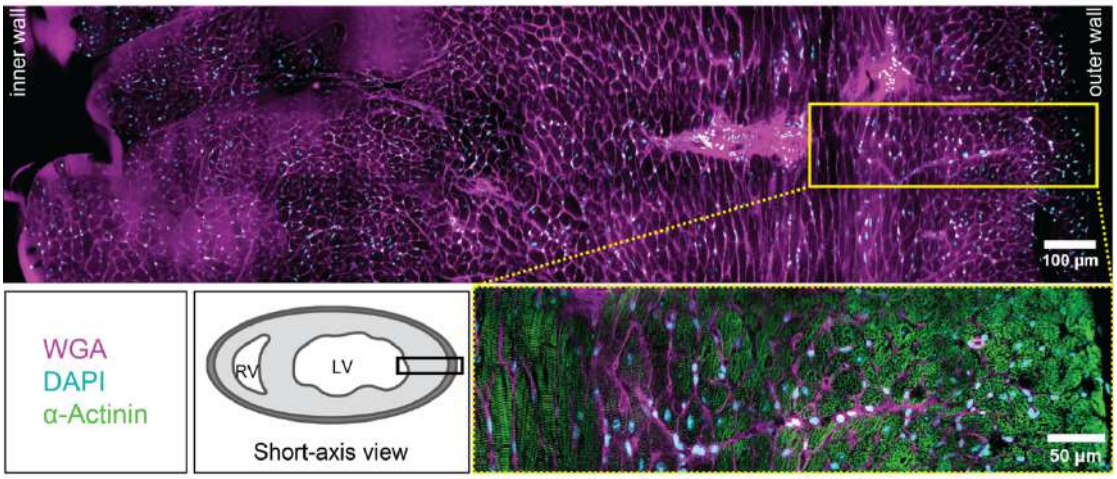

Figure 44: A representative image highlighting the cardiomyocytes stained using WGA, DAPI and alpha actinin to mark the cell membranes, nuclei and Z-disc regions of sarcomeres, respectively.
The images were acquired with a 60X objective using a confocal microscope. The LV-wall region marked with a black box in the schematic representation of the short axis section (bottom middle) is shown in the top panel. A zoomed in region (yellow box) showing the middle wall to outer wall area is shown in the bottom right panel. The cardiomyocytes in the outer wall pick up staining for alpha actinin, confirming the presence of cardiac muscle cells. The scale bars are as indicated.

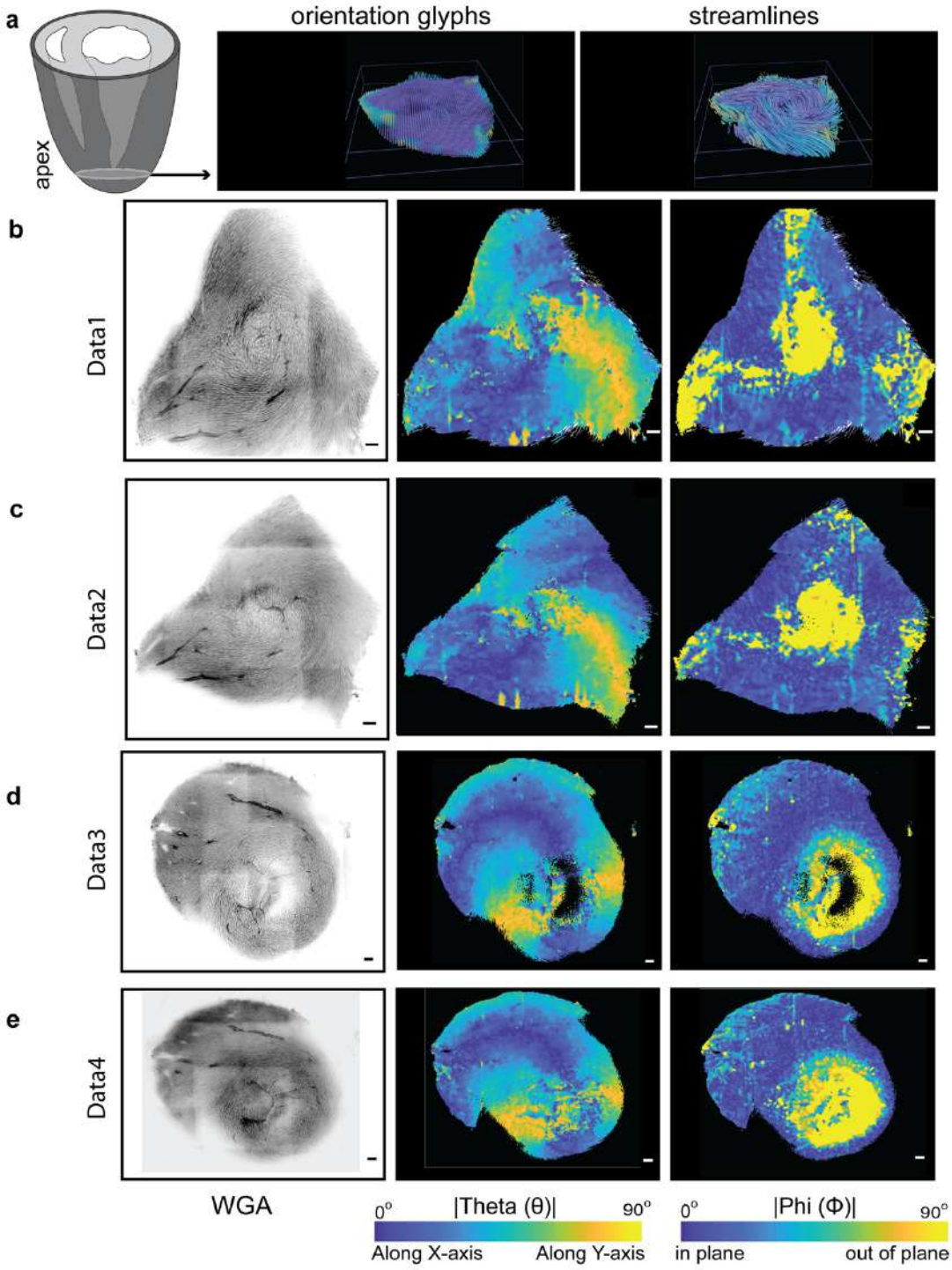

Figure 45: Analysis of a short-axis section from the apex region.
a. Orientation glyphs and streamlines for the apex section shown in b. **b-e.** WGA in grayscale, and θ and Φ colormaps of the representative apex section. The colormap scale is as indicated, with the scale bar being 100 microns from four different datasets.

CHAPTER – 5
DISCUSSION

5.1 Hypothesizing the role of the outer wall orthogonal cell layer for heart functioning

The mammalian four-chambered heart during each heartbeat cycle undergoes three different contractions; contraction w.r.t the short axis (radial), long axis (longitudinal) and helical to eject the blood. While existing literature mainly focuses on the circumferential and helical twisting of myofibers, the longitudinal movements or long-axis shortening are poorly explained (24,82). Our discovery of the distinct long-axis outer wall myofiber geometry opens new avenues to study the longitudinal contractions of the heart. We speculate that these long-axis myofibers from the outer wall might play a role in the longitudinal contraction of the heart. Though we have not observed any morphological or anatomical distinction between the circumferential (helical) cardiomyocyte layers and the long-axis cardiomyocyte layers from our WGA staining; the long-axis cardiomyocyte layers do seem to be geometrically unique and to run in confined bands from base to apex. The orientation pattern of the cardiomyocytes and the reconstructed streamlines from our work fits the description of being distinct fiber system in the heart wall. Previous work have discovered some proof of unique collagen organization in the subepicardial/ outer wall region (83). This suggests that there is a structural distinction at some level in terms of the extracellular matrix organization, but that this is independent of the cell-level study conducted in this thesis.

During heart contraction the ventricular walls undergo a wringing motion from the apex towards the base, accompanied by a slight shortening of the heart occurs along its long-axis direction. Together these motions produce sufficient ejection force to empty the chambers. While the bulk of the contraction is affected by the circumferential myocardial fibers, we hypothesize that the continuum of long-axis fibers might play a significant role in its long-axis shortening. Additionally, we have observed that the four bands of long-axis fibers continue upwards to the base from the apex (Figure 42) and are anchored to the atrioventricular valves (Figure 48). The opening and closing of the atrioventricular valves must be synchronized with the contraction of the left/right chambers, but currently no model exists that connects myofibers these valves. Since the long-axis fibers are anchored to the valves, we postulate that their opening/closing is partly controlled by contraction and relaxation of the long-axis fibers.

5.2 Orthogonal muscle arrangement in other organs/tissue types and their function

We have discovered a new long-axis fiber system which is a conserved feature in the ventricular outer walls of four-chambered rodent hearts. This new long-axis fiber geometry is, in fact, not restricted to mammalian hearts. Similar fiber organizations have been reported in other organs and entire animal body plans (84–86). The orthogonal muscle fiber system described in this study has similarities to other peristaltic organs that have multilayered fiber/muscle arrangement. The intestinal tract uses peristalsis to move food through the gastrointestinal tract (84,86). With the outer layer of muscles contracting in the opposite direction from the inner layer, the muscles in the intestinal wall are arranged in an orthogonal pattern. The peristalsis movement forces food through the digestive tract in a wave-like motion.

A similar system of orthogonal muscle fibers is also present in other organs, such as the ureter, which transports urine from the kidney to the bladder through peristalsis (87). The orthogonal muscle fiber system is present in these organs because it is necessary for the efficient and coordinated contraction required to move fluids and other materials through them. At the organ level, the co-existence of a circumferential and longitudinal fiber system is known to be important for the smooth muscle peristaltic motions seen in esophageal and intestinal tubes.

In planarians, in addition to the circumferential and longitudinal muscle fibers, a diagonal fiber system has been reported (85). This entire organism level orthogonal muscle array has been shown to be important for regeneration. However, an important difference between the heart and these layered muscle fiber organizations is that in the latter, the orthogonal arrays occupy an equal volume (84–86). In contrast, the orthogonal fiber systems recovered from our analysis account for only a small fraction of the myofibers in the heart wall, suggesting that they have highly specialized roles. In short the orthogonal muscle fiber system has been preserved throughout evolution in a variety of organisms, and a pump-like muscular architecture serves as a demonstration of its effectiveness.

5.3 Significance of long-axis fiber continuum in electrical conduction

The electrical signals from the sinoatrial node propagate to the atrioventricular node to cause the ventricles to pump blood, via a network of Purkinje fibers (18,88). In Purkinje cells, potassium channels are mainly located at the end of the cell, near the intercalated discs (17,89). This arrangement allows for a large influx of potassium ions during the plateau phase of the action potential. In contrast, potassium channels in working cardiomyocytes are located along the cell membrane and are more evenly distributed. This arrangement allows for a more even spread of potassium ions during the repolarization phase of the action potential.

It is reported that there is a spike in the action potential measurements in the epicardial regions of LV from the human heart and indication of a different geometrical arrangement of cardiomyocytes causing this sudden change in the action potential profile (90). The major cause of such repolarization events is attributed by potassium channel fluxing ions out of cells (89). In inference, there are numerous arguments in favor of a distinct action potential profiles and cellular/ECM orientation pattern in the area of the outer wall.

Analyses have shown that the circumferential fibers, together with their associated transmural turning from the outer wall to the inner wall, can explain the point-to-point time-to-arrival maps under a model of anisotropic diffusion (91). Moreover, the transmural turning has been shown to play a role in minimizing diffusion bias and mitigating the potentially harmful effects of stochastic propagation (24). However, how the timing of the contraction is controlled at any circumferential fibers is an open question.

What distinguishes Purkinje cardiomyocytes (inner wall), working cardiomyocytes (middle wall), and outer wall cardiomyocytes in terms of their ion channel configurations needs more research. However, it is well recognized that working cardiomyocytes are involved in the excitation-contraction coupling process, which produces the force required for cardiac contraction, and that Purkinje fibers play a significant part in the passage of electrical signals across the heart (10,17,18). Depending on their particular roles in the heart, it is likely that the types and configurations of ion channels found in these various types of cardiomyocytes may vary.

5.4 Importance of cardiomyocyte organizations in disease conditions and development

Pathological conditions of heart are known to cause sarcomere disarrays and acquired arrhythmia due course in time (10). In majority of cardiomyopathy cases, mutations in genes associated with sarcomere related proteins pertain (40,92). Channelopathies where the ion channels related mutations cause deformed ion imbalance have two opposite spectrum of diseases states; one with structural defects and the other without structural defects of heart. Laminopathy creates a nucleus deformation and sarcomere disarray in cardiomyocytes being one of first candidate cause for inherited DCM (38,41). It remains to be seen whether perturbations of the orthogonal fiber systems are associated with heart diseases such as cardiomyopathies, myocardial infarction and electrical conduction disorders.

Moreover, the stage of heart development at which this orthogonal myofiber array gets embedded in the heart wall is as yet not known. The myofiber organization at the micron scale recovered in this study lays a foundation for future examinations of the association between pathological heart conditions or disorders and fiber organization. But we do not know how these disease conditions can affect the cardiomyocyte organization in ventricles. In the future direction of this study, we intend to address these biologically relevant questions (Figure 49).

5.5 Advantages and Limitations

The protocols detailed in this thesis are limited to imaging and the data analysis derived from adult rodent hearts. While our protocol could be useful for studying any other organ at any developmental stage in 3D at the required spatiotemporal resolution, the challenges associated with the tissue specific properties, specimen handling, imaging and analysis could be expected with varying tissue features. Our strategic sectioning of the organ both in the short- and long-axis allowed us to get a full picture of heart myofibers. We took advantage of the elongated nature of cardiomyocytes, which aided the structure tensor method by feature extraction based on the intensity gradient near cell membranes. Our imaging technology might be used to image different cellular structures in various organs, albeit we opted to focus on the orientation of murine cardiomyocytes in this study. For instance, it might be applied to the liver to establish a precise hepatocyte orientation in respect to the various liver areas. With a better

understanding of the entire sarcoma microenvironment, it is possible to identify differences in the distributions of muscle cells in tumours and after drug distributions.
Our orientation estimation pipeline can be applied to other organs such as the kidney and liver if the asymmetric nature of cells and tissue architecture could be captured/imaged. However, for the other types of cells where the cell morphology is highly variable or geometry is more symmetrical, the segmentation-based orientation method would be more applicable for orientation estimation by structure tensor analysis. This is comparable to the ground truth experiment in this thesis where cardiomyocytes were hand segmented and average orientation per cell was calculated based on the cell contour. The cell segmentation could be automated in such cases based on neural network training for larger tissue volume analysis.
Our cardiomyocyte orientation reconstructions at the micron scale confirmed a distinct epicardial cell layer system geometrically. However, the physiological relevance of the outer wall cardiac fiber system has to be verified further. Although our images show that the long-axis cell layers converge at the apex, the exact architecture of cell layers and how fibers intertwine and emerge to the ventricular inner/outer wall sites is still an open question. With a thorough understanding of the structure at the apex, we can build more accurate computer models for simulations, leading to greater insights into heart function and potential drug development. The imaging depth that encodes each heart section in our study is limited by 300μm but from two different heart sections. This depth is sufficient to capture a complete cardiomyocyte in 3D but limited by the probability of such oriented cardiomyocytes within a block. The confocal microscopy imaging for tiling is time-consuming for covering the entire tissue sections but provides more precise signals pronounced by spectral detectors that reduce the pre-processing efforts. In this study, we used fluorescent WGA and did not face any issues with the penetration of dyes in thick tissue samples. However, the same tissue samples suffered staining and penetration issues when stained with antibodies. Similarly, the blurriness in the deeper layers is a common problem in any fluorescence imaging microscopy setup; light sheet microscopes with multi-objectives or sample rotating stages could allow multiview registration of the sample viewed from different angles reducing the blurriness in depth. A combination of advanced 3D imaging with light sheet microscopy along with fluorescent tag-expressed mouse models can overcome imaging thick tissues or intact organ samples.

Our study will provide crucial information about the cardiomyocyte architecture of the intact heart for a common data bank. A similar approach has already been successfully implemented in brain mapping studies, contributing to understanding many neurological diseases (93). The structural information obtained from our studies can be used to understand the mechanism of various cardiomyopathies affecting the heart.

In the field of regenerative therapy for the heart, one of the major problems is the failure of differentiated iPSC cells to function in accordance with the rest of the heart. Towards this aspect, Milica and colleagues have developed iPSC differentiated implants (cardiac patches) that require external electrical impulses to beat synchronously with normal cardiomyocytes (94). For the implanted cells to function properly, they must align with the native cardiomyocytes. For such applications, a thorough understanding of cellular orientation can be obtained from our model (Figure 47). Furthermore, this method correctly simplifies and downscales the data without changing any of the geometrical or signal intensity characteristics of the original images.

5.6 Future directions

The future directions of this project involve understanding the functional relevance of the long-axis outer-ventricular wall cardiomyocyte arrangement observed at the micron scale using light microscopy both during healthy and diseased conditions. One way to do this is to investigate the distribution of different molecular markers targeted at ion channels and T-tubular arrangement at high-resolution confocal microscopy. Ion channels are essential for cardiomyocyte function, and T-tubules are involved in the excitation-contraction process. By understanding how these molecular markers are distributed differently in the long-axis outer-ventricular wall compared to other regions of the heart, we can gain insights into how this unique cardiomyocyte arrangement may contribute to cardiac function.

Another way to investigate the functional relevance of this cardiomyocyte arrangement is to analyze the cardiomyopathy models such as MyBPC3-25bp del, PKC mutant, Lamin A mutant, and DMD hearts. These cardiomyopathy models are characterized by different types of heart disease, and it is possible that the long-axis outer ventricular wall cardiomyocyte arrangement may be altered in these conditions. By comparing the cardiomyocyte arrangement in healthy and diseased hearts, we can identify any changes that may be associated with heart disease.

In addition to investigating the functional relevance of the long-axis outer ventricular wall cardiomyocyte arrangement, the future directions of this project also include investigating the developmental emergence of this cardiomyocyte layer. This can be done by analyzing mouse embryonic hearts at different stages of development, from E12.5 to E16. By understanding how the long axis outer-ventricular wall cardiomyocyte layer develops, we can gain insights into how this unique cardiomyocyte arrangement may contribute to cardiac function in the adult heart.

The latest advancements in light microscopy, such as light-sheet illumination, can be used to investigate the more volumetric details of mouse ventricular walls, especially at the apex region. This was not possible earlier due to the limited depth of coverage of confocal imaging. By using these newer technologies, we can gain a more complete understanding of the three-dimensional structure of the heart, including the long axis outer-ventricular wall cardiomyocyte layer.

Overall, the future directions of this project are focused on understanding the functional relevance and developmental emergence of the long axis outer-ventricular wall cardiomyocyte arrangement. By investigating this unique cardiomyocyte arrangement using a combination of light microscopy and cardiomyopathy models, we can gain new insights into how this arrangement contributes to cardiac function both in health and disease. Understanding of the heart's complex structure and function, and could potentially pave the way for new diagnostic and therapeutic approaches for heart disease.

5.7 Summary of findings

Tissue clearing methods together with three-dimensional imaging of biological samples have revealed fundamental new insights (45,50,58). Inspired by this, we established a pipeline to image heart tissue using conventional confocal microscopy and analyze it quantitatively with computer vision methods (Synopis Figure). A key advancement in our study is the integration of fluorescence-based micron-scale heart imaging and geometric image analysis and myofiber reconstruction and methods for the microscopy images. This combination led to a resolution gain of ~3 orders of magnitude in scale (i.e., from millimeter to micron), revealing an entirely new fiber system, one that has eluded discovery by previous lower resolution imaging methods.

From the short-axis viewing plane, we demonstrate a long-axis fiber system that is distinctly orthogonal to the circumferential fibers in the myocardial layer. In the left ventricle this system occupies a very thin band (~50 microns in thickness), thus constituting only a small fraction (~ 3%) of the width of the heart wall. We have observed four bands of long-axis myofibers: a crescent shaped band restricted to the left and right ventricular outer walls and two orbicular layers surrounding the inner walls of the left and right ventricular chambers (Figures 32, 43 and 48). In the left ventricle the crescent-shaped encompasses the entire left side of the outer wall, with thinner parts tapering near the anterior and inferior side. In the right ventricle the long-axis myofibers are confined to the middle of the outer wall. Whereas the long-axis myofiber systems in the short-axis sections appear as isolated bands, the long-axis section reconstructions show that they indeed taper to form a continuum of long-axis fibers from the ventricles to the apex (Figure 43). Both this long-axis system at the outer wall and the longitudinal fibers in the endocardium, appear to be conserved features in the ventricular walls of four-chambered rodent hearts including mouse and rat (Figure 46).

At the apex the long-axis fibers turn upwards towards the base of the heart and then continue to the adjacent boundaries of the heart wall, e.g., the long-axis fibers of the left ventricular outer wall are connected to the right ventricle outer wall and inner chamber walls (Figure 42). Although from the HLA-4C sections we could only directly observe a few such connections between long-axis fibers, it is quite likely that all the long-axis fibers are interconnected. Further evidence for this is in the trifurcation of three distinct long axis bands of myofibers, from a single source region at the apex (Figure 45). Together these observations highlight our discovery of a continuum of long-axis myofibers which co-exist with but remain distinct from circumferential ones.

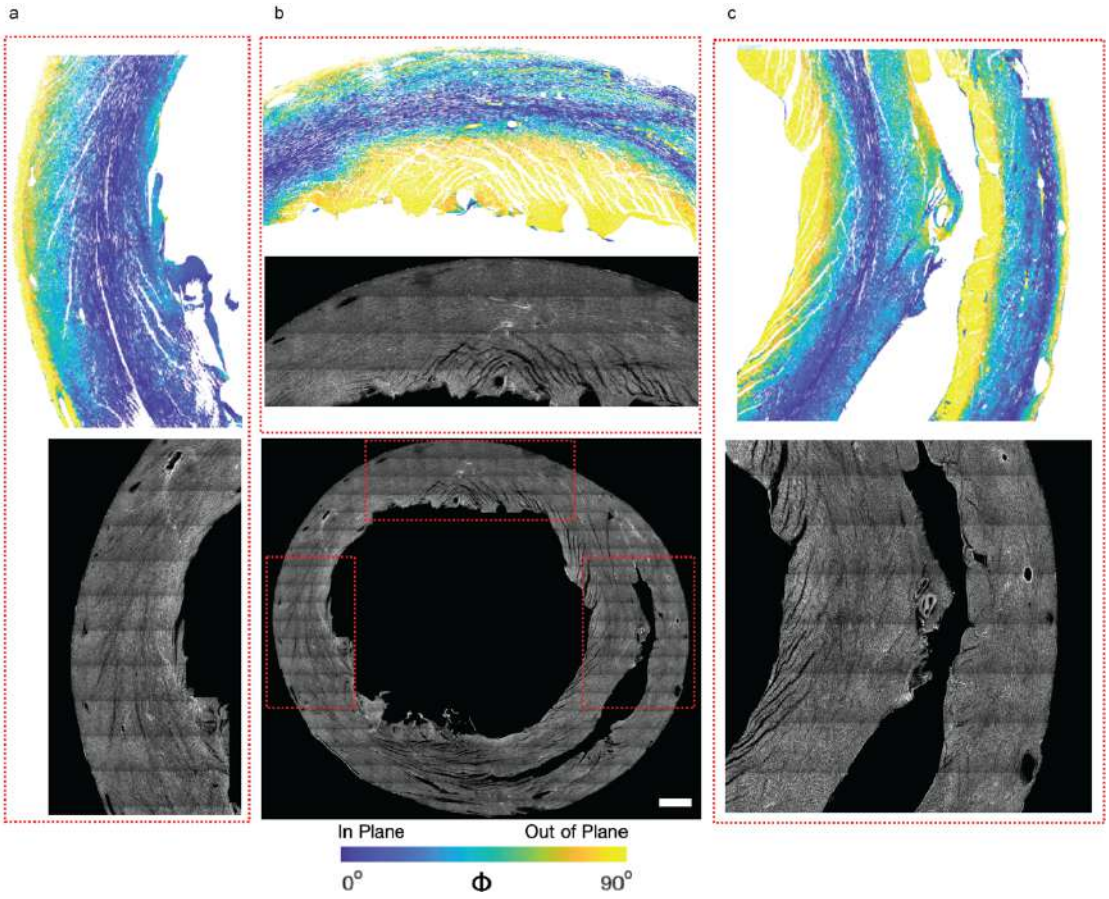

Figure 46: Short-axis section analysis of a rat heart.
a. A short-axis view of the ventricular chambers of a rat heart, sectioned at PSAX-PML (parasternal short-axis – papillary muscle level). A maximum intensity projection of the WGA stain is shown in grayscale, with the Φ angle shown using a parula colormap. The scale bar is 1000 microns. **b-d.** Zoomed in regions from the left ventricle, septum and right ventricle, with the WGA stain shown in grayscale and the Φ angle shown using a parula colormap. The scale bar is 1000 microns for full view (b-bottom panel). The color bar is as indicated.

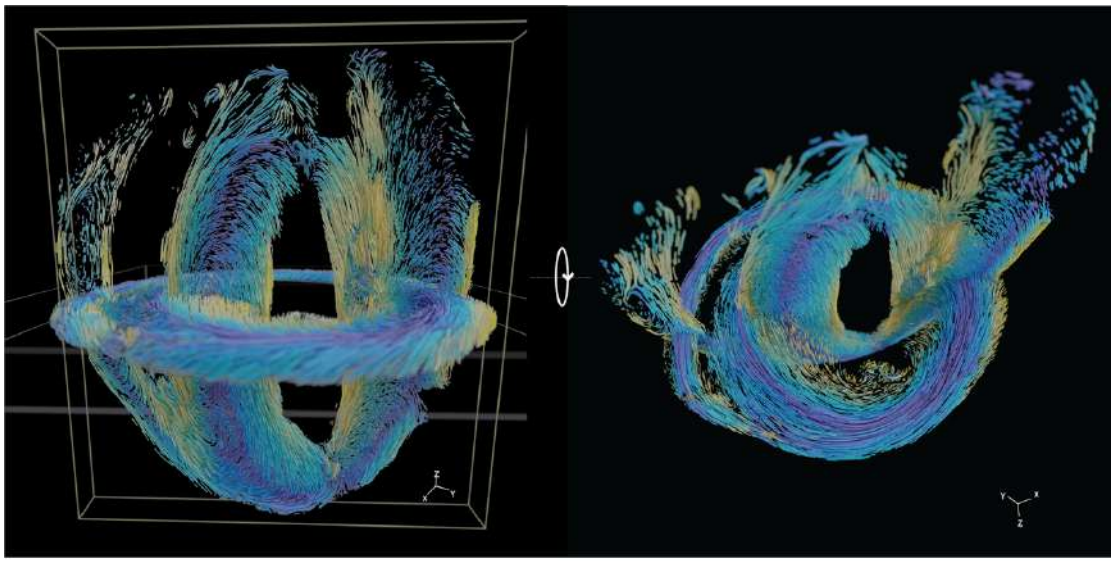

Figure 47: The composite model is obtained by superposition of the reconstructions of the short-axis and long-axis sections from different mouse hearts.
The structure tensor-based orientations are visualized as streamlines (Chapter 3, Methods). The colors follow a parula colormap, where the blue and yellow tones indicate orientations in or out of the short-axis plane, respectively.

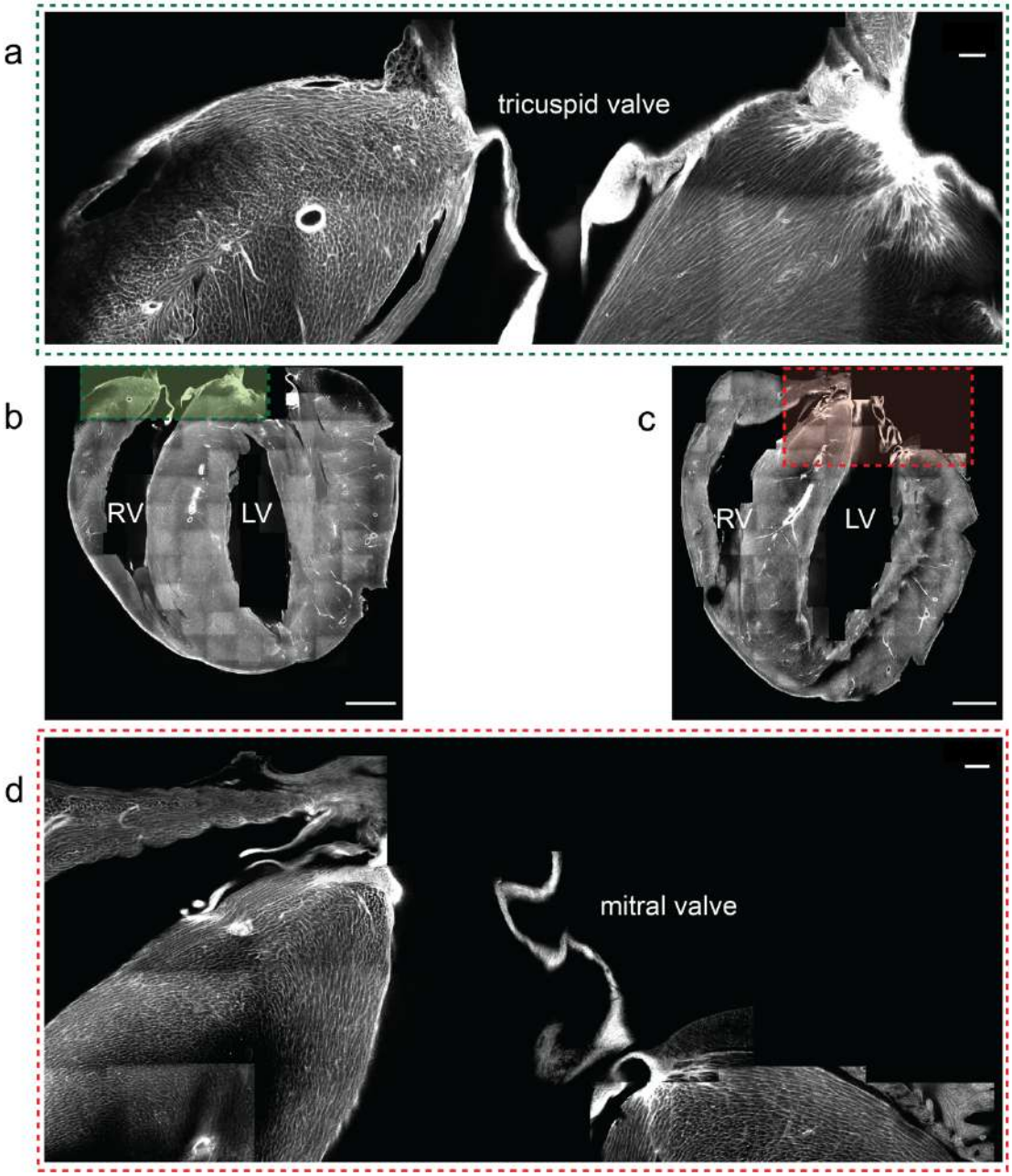

Figure 48: Connections of long-axis fibers at the atrioventricular valve region. Representative images highlighting the anchor points of the longitudinal fibers of the right ventricle and the septal outer and inner walls (top) and the long-axis fibers of the left ventricle and the septal outer and inner walls (bottom). **a. and c.** WGA maximum intensity Z-projection of the whole long-axis section. **b. and d.** Zoomed in regions of the right and left AV valve as indicated, WGA (in grey) and streamlines (in parula colormap). The scale bar is 1000 microns.

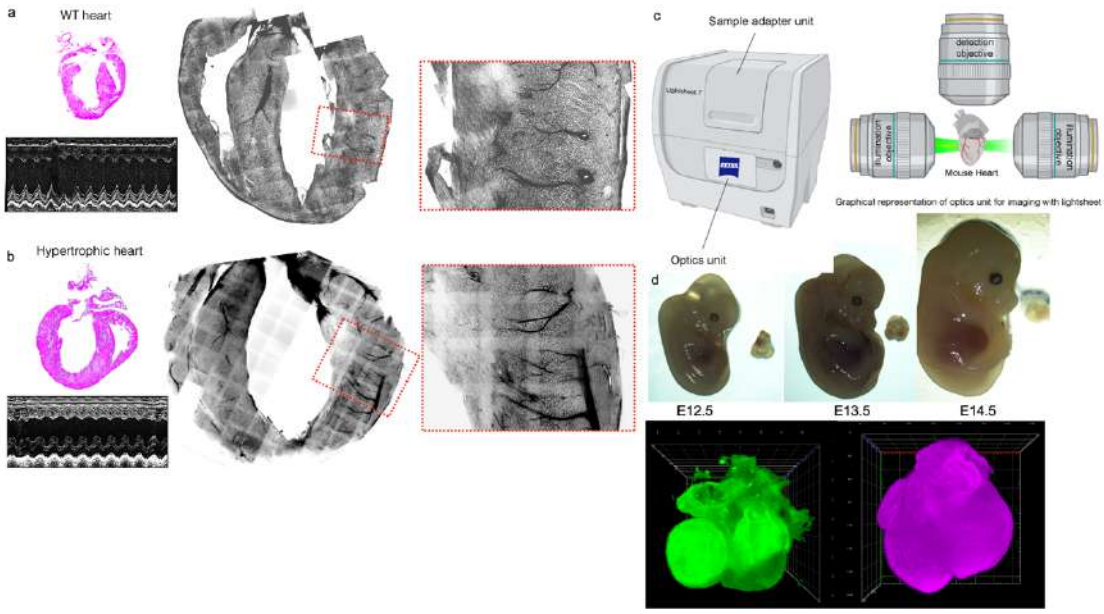

Figure 49: Future directions for investigating the functional relevance of the long axis outer-ventricular wall cardiomyocyte arrangement.
a-b. Analyzing cardiomyopathy models such as MyBPC3-25bp del, PKC mutant, Lamin A mutant, and DMD hearts to identify any changes in the long axis outer-ventricular wall cardiomyocyte arrangement. **c**. Using new light microscopy technologies such as light-sheet microscopy to investigate the more volumetric details of mouse ventricular walls, especially at the apex region. **d**. Investigating the developmental emergence of the long axis outer-ventricular wall cardiomyocyte layer by analyzing mouse embryonic hearts at different stages of development.

LIST OF PUBLICATIONS FROM PH.D. STUDIES

1. Dileep, D*., Syed, T. A*., Sloan, T. F., Dhandapany, P. S., Siddiqi, K., & Sirajuddin, M. (2023). Cardiomyocyte orientation recovery at micron scale reveals long-axis fiber continuum in heart walls. The *EMBO Journal.* *co-first authors. https://doi.org/10.15252/embj.2022113288

2. Syed, T. A., Wang, Y., Dileep, D., Sirajuddin, M., & Siddiqi, K. (2023, June). Ultrastructure Analysis of Cardiomyocytes and Their Nuclei. In International Conference on Functional Imaging and Modeling of the Heart (pp. 14-24). Cham: Springer Nature Switzerland. https://doi.org/10.1007/978-3-031-35302-4_2

3. Mendon, N., Ganie, R. A., Kesarwani, S., Dileep, D., Sasi, S., Lama, P., ... & Sirajuddin, M. (2023). Nanobody derived using a peptide epitope from the spike protein receptor-binding motif inhibits entry of SARS-CoV-2 variants. Journal of Biological Chemistry, 299(1). https://doi.org/10.1016/j.jbc.2022.102732

LIST OF SELECTED PH.D. WORK PRESENTATIONS IN CONFERENCES

1. EMBO-India Lecture Series on Microphysiological systems, CCMB, Hyderabad, 31st October to 4th November 2022 (Poster Presentation)
2. Imaging Mouse Development, HHMI Conference, Ashburn, USA, 18th-21st September 2022 (Poster Presentation)
3. inStem Annual Review of Research, Bangalore, 2022, March 2022 (Poster Presentation – Received Best Poster Award)
4. NCBS Annual Talks, Bangalore 2022, January 12, 2022. “Discovery of longitudinal myofiber system in heart ventricular walls” (Oral presentation)

REFERENCES

1. Olson EN. Gene Regulatory Networks in the Evolution and Development of the Heart. Science. 2006 Sep 29;313(5795):1922–7.

2. Tyser RCV, Srinivas S. The First Heartbeat—Origin of Cardiac Contractile Activity. Cold Spring Harb Perspect Biol. 2020 Jul;12(7):a037135.

3. Solc D. The heart and heart conducting system in the kingdom of animals: A comparative approach to its evolution. Exp Clin Cardiol. 2007;12(3):113–8.

4. Tran DB, Weber C, Lopez RA. Anatomy, Thorax, Heart Muscles. [Updated 2022 Dec 3]. In: StatPearls [Internet]. Treasure Island (FL): StatPearls Publishing; 2023 Jan-. Available from: https://www.ncbi.nlm.nih.gov/books/NBK545195/.

5. American Heart Association Writing Group on Myocardial Segmentation and Registration for Cardiac Imaging:, Cerqueira MD, Weissman NJ, Dilsizian V, Jacobs AK, Kaul S, et al. Standardized Myocardial Segmentation and Nomenclature for Tomographic Imaging of the Heart: A Statement for Healthcare Professionals From the Cardiac Imaging Committee of the Council on Clinical Cardiology of the American Heart Association. Circulation. 2002 Jan 29;105(4):539–42.

6. Litviňuková M, Talavera-López C, Maatz H, Reichart D, Worth CL, Lindberg EL, et al. Cells of the adult human heart. Nature. 2020 Dec 17;588(7838):466–72.

7. Alberts B, Johnson A, Lewis J, et al. Molecular Biology of the Cell. 4th edition. New York: Garland Science; 2002. Blood Vessels and Endothelial Cells. Available from: https://www.ncbi.nlm.nih.gov/books/NBK26848/.

8. Sommer JR, Scherer B. Geometry of cell and bundle appositions in cardiac muscle: light microscopy. Am J Physiol-Heart Circ Physiol. 1985 Jun 1;248(6):H792–803.

9. Kartha. Cardiomyocytes in Health and Disease. 2021;

10. Woodcock EA, Matkovich SJ. Cardiomyocytes structure, function and associated pathologies. Int J Biochem Cell Biol. 2005 Sep;37(9):1746–51.

11. Lipsett DB, Frisk M, Aronsen JM, Nordén ES, Buonarati OR, Cataliotti A, et al. Cardiomyocyte substructure reverts to an immature phenotype during heart failure. J Physiol. 2019 Apr;597(7):1833–53.

12. Sheikh F, Ross RS, Chen J. Cell-Cell Connection to Cardiac Disease. Trends Cardiovasc Med. 2009 Aug;19(6):182–90.

13. Cretoiu D, Pavelescu L, Duica F, Radu M, Suciu N, Cretoiu SM, Xiao J. Muscle atrophy. Adv Exp Med Biol 2018108823-46.

14. Olivotto I, d'Amati G, Basso C, Van Rossum A, Patten M, Emdin M, et al. Defining phenotypes and disease progression in sarcomeric cardiomyopathies:

contemporary role of clinical investigations. Cardiovasc Res. 2015 Apr 1;105(4):409–23.

15. Ibrahim M, Gorelik J, Yacoub MH, Terracciano CM. The structure and function of cardiac t-tubules in health and disease. Proc Biol Sci. 2011 Sep 22;278(1719):2714–23.

16. Watanabe H, Tao G, Gan P, Westbury BC, Cox KD, Tjen K, et al. Purkinje Cardiomyocytes of the Adult Ventricular Conduction System Are Highly Diploid but Not Uniquely Regenerative. J Cardiovasc Dev Dis. 2023 Apr 7;10(4):161.

17. Dun W, Boyden PA. The Purkinje cell; 2008 style. J Mol Cell Cardiol. 2008 Nov;45(5):617–24.

18. Sedmera D, Gourdie R. Why Do We Have Purkinje Fibers Deep in Our Heart? Physiol Res Acad Sci Bohemoslov. 2014 Feb 24;63 Suppl 1:S9–18.

19. von Deuster C, Sammut E, Asner L, Nordsletten D, Lamata P, Stoeck CT, et al. Studying Dynamic Myofiber Aggregate Reorientation in Dilated Cardiomyopathy Using In Vivo Magnetic Resonance Diffusion Tensor Imaging. Circ Cardiovasc Imaging [Internet]. 2016 Oct 1 [cited 2021 Sep 2];9(10):e005018. Available from: https://www.ahajournals.org/doi/full/10.1161/CIRCIMAGING.116.005018

20. Chen J, Song SK, Liu W, McLean M, Allen JS, Tan J, et al. Remodeling of cardiac fiber structure after infarction in rats quantified with diffusion tensor MRI. Am J Physiol-Heart Circ Physiol [Internet]. 2003 Sep 1 [cited 2021 Sep 2];285(3):H946–54. Available from: https://journals.physiology.org/doi/full/10.1152/ajpheart.00889.2002

21. Geerts-Ossevoort L, Bovendeerd P, Prinzen F, Arts T, Nicolay K. Myofiber orientation in the normal and infarcted heart, assessed with MR-diffusion tensor imaging. In: Computers in Cardiology 2001 Vol28 (Cat No01CH37287). 2001. p. 621–4.

22. Rushmer RF, Crystal DK, Wagner C. The Functional Anatomy of Ventricular Contraction. Circ Res. 1953 Mar;1(2):162–70.

23. Young RJ, Panfilov AV. Anisotropy of wave propagation in the heart can be modeled by a Riemannian electrophysiological metric. Proc Natl Acad Sci U S A. 2010 Aug 24;107(34):15063–8.

24. Aumentado-Armstrong T, Kadivar A, Savadjiev P, Zucker SW, Siddiqi K. Conduction in the Heart Wall: Helicoidal Fibers Minimize Diffusion Bias. Sci Rep. 2018 May 8;8(1):7165.

25. Sweeney HL, Hammers DW. Muscle Contraction. Cold Spring Harb Perspect Biol. 2018 Feb;10(2):a023200.

26. Arackal A, Alsayouri K. Histology, Heart. [Updated 2023 Jan 2]. In: StatPearls [Internet]. Treasure Island (FL): StatPearls Publishing; 2023 Jan-. Available from: https://www.ncbi.nlm.nih.gov/books/NBK545143/.

27. Parmacek MS, Epstein JA. Cardiomyocyte Renewal. N Engl J Med. 2009 Jul 2;361(1):86–8.

28. Gilbert SH, Benson AP, Li P, Holden AV. Regional localisation of left ventricular sheet structure: integration with current models of cardiac fibre, sheet and band structure. Eur J Cardiothorac Surg. 2007 Aug;32(2):231–49.

29. Torrent-Guasp F, Buckberg GD, Clemente C, Cox JL, Coghlan HC, Gharib M. The Structure and Function of the Helical Heart and Its Buttress Wrapping. I. The Normal Macroscopic Structure of the Heart. Semin Thorac Cardiovasc Surg. 2001 Oct 1;13(4):301–19.

30. Savadjiev P, Strijkers GJ, Bakermans AJ, Piuze E, Zucker SW, Siddiqi K. Heart wall myofibers are arranged in minimal surfaces to optimize organ function. Proc Natl Acad Sci. 2012 Jun 12;109(24):9248–53.

31. Remodeling of cardiac fiber structure after infarction in rats quantified with diffusion tensor MRI | American Journal of Physiology-Heart and Circulatory Physiology [Internet]. [cited 2022 Dec 18]. Available from: https://journals.physiology.org/doi/full/10.1152/ajpheart.00889.2002

32. O'Donnell LJ, Westin CF. An Introduction to Diffusion Tensor Image Analysis. Neurosurg Clin N Am. 2011 Apr;22(2):185–96.

33. Anderson PA. The heart and development. Semin Perinatol. 1996 Dec;20(6):482–509.

34. Brade T, Pane LS, Moretti A, Chien KR, Laugwitz KL. Embryonic Heart Progenitors and Cardiogenesis. Cold Spring Harb Perspect Med. 2013 Oct 1;3(10):a013847–a013847.

35. Wexler RK, Elton T, Pleister A, Feldman D. Cardiomyopathy: an overview. Am Fam Physician. 2009 May 1;79(9):778–84.

36. Basit H, Brito D, Sharma S. Hypertrophic Cardiomyopathy. [Updated 2023 Apr 7]. In: StatPearls [Internet]. Treasure Island (FL): StatPearls Publishing; 2023 Jan-. Available from: https://www.ncbi.nlm.nih.gov/books/NBK430788/.

37. Marian AJ, Braunwald E. Hypertrophic Cardiomyopathy: Genetics, Pathogenesis, Clinical Manifestations, Diagnosis, and Therapy. Circ Res. 2017 Sep 15;121(7):749–70.

38. Giri P, Mukhopadhyay A, Gupta M, Mohapatra B. Dilated cardiomyopathy: a new insight into the rare but common cause of heart failure. Heart Fail Rev. 2022 Mar;27(2):431–54.

39. Schultheiss HP, Fairweather D, Caforio ALP, Escher F, Hershberger RE, Lipshultz SE, et al. Dilated cardiomyopathy. Nat Rev Dis Primer. 2019 May 9;5(1):32.

40. Kamisago M, Sharma SD, DePalma SR, Solomon S, Sharma P, McDonough B, et al. Mutations in Sarcomere Protein Genes as a Cause of Dilated Cardiomyopathy. N Engl J Med. 2000 Dec 7;343(23):1688–96.

41. Nikolova V, Leimena C, McMahon AC, Tan JC, Chandar S, Jogia D, et al. Defects in nuclear structure and function promote dilated cardiomyopathy in lamin A/C–deficient mice. J Clin Invest. 2004 Feb 1;113(3):357–69.

42. Saleh M, Ambrose JA. Understanding myocardial infarction. F1000Research. 2018 Sep 3;7:1378.

43. Bensley JG, De Matteo R, Harding R, Black MJ. Three-dimensional direct measurement of cardiomyocyte volume, nuclearity, and ploidy in thick histological sections. Sci Rep. 2016 Apr 6;6(1):23756.

44. Seidel T, Edelmann JC, Sachse FB. Analyzing Remodeling of Cardiac Tissue: A Comprehensive Approach Based on Confocal Microscopy and 3D Reconstructions. Ann Biomed Eng. 2016 May;44(5):1436–48.

45. Perbellini F, Liu AKL, Watson SA, Bardi I, Rothery SM, Terracciano CM. Free-of-Acrylamide SDS-based Tissue Clearing (FASTClear) for three dimensional visualization of myocardial tissue. Sci Rep. 2017 Jul 12;7(1):5188.

46. Fei P, Lee J, Packard RRS, Sereti KI, Xu H, Ma J, et al. Cardiac Light-Sheet Fluorescent Microscopy for Multi-Scale and Rapid Imaging of Architecture and Function. Sci Rep. 2016 Mar 3;6(1):22489.

47. Greenbaum RA, Ho SY, Gibson DG, et alLeft ventricular fibre architecture in man.Heart 1981;45:248-263.

48. Young, Legrice, Young, Smaill. Extended confocal microscopy of myocardial laminae and collagen network. J Microsc. 1998 Nov;192(2):139–50.

49. Teh I, McClymont D, Zdora MC, Whittington HJ, Davidoiu V, Lee J, et al. Validation of diffusion tensor MRI measurements of cardiac microstructure with structure tensor synchrotron radiation imaging. J Cardiovasc Magn Reson. 2017 Dec;19(1):31.

50. Tian T, Yang Z, Li X. Tissue clearing technique: Recent progress and biomedical applications. J Anat. 2021 Feb;238(2):489–507.

51. Susaki EA, Ueda HR. Whole-body and Whole-Organ Clearing and Imaging Techniques with Single-Cell Resolution: Toward Organism-Level Systems Biology in Mammals. Cell Chem Biol. 2016 Jan;23(1):137–57.

52. Verveer PJ, Swoger J, Pampaloni F, Greger K, Marcello M, Stelzer EHK. High-resolution three-dimensional imaging of large specimens with light sheet-based microscopy. Nat Methods. 2007 Apr;4(4):311–3.

53. Zhan Y, Wu H, Liu L, Lin J, Zhang S. Organic solvent-based tissue clearing techniques and their applications. J Biophotonics. 2021 Jun;14(6):e202000413.

54. Tainaka K, Murakami TC, Susaki EA, Shimizu C, Saito R, Takahashi K, et al. Chemical Landscape for Tissue Clearing Based on Hydrophilic Reagents. Cell Rep. 2018 Aug;24(8):2196-2210.e9.

55. Susaki EA, Tainaka K, Perrin D, Yukinaga H, Kuno A, Ueda HR. Advanced CUBIC protocols for whole-brain and whole-body clearing and imaging. Nat Protoc. 2015 Nov;10(11):1709–27.

56. Choi SW, Guan W, Chung K. Basic principles of hydrogel-based tissue transformation technologies and their applications. Cell. 2021 Aug;184(16):4115–36.

57. Gradinaru V, Treweek J, Overton K, Deisseroth K. Hydrogel-Tissue Chemistry: Principles and Applications. Annu Rev Biophys. 2018 May 20;47(1):355–76.

58. Advanced CLARITY for rapid and high-resolution imaging of intact tissues | Nature Protocols [Internet]. [cited 2022 Dec 19]. Available from: https://www.nature.com/articles/nprot.2014.123

59. Tomer R, Ye L, Hsueh B, Deisseroth K. Advanced CLARITY for rapid and high-resolution imaging of intact tissues. Nat Protoc. 2014 Jul;9(7):1682–97.

60. Goodyer WR, Beyersdorf BM, Paik DT, Tian L, Li G, Buikema JW, et al. Transcriptomic Profiling of the Developing Cardiac Conduction System at Single-Cell Resolution. Circ Res. 2019 Aug 2;125(4):379–97.

61. Budde MD, Frank JA. Examining brain microstructure using structure tensor analysis of histological sections. NeuroImage. 2012 Oct;63(1):1–10.

62. Yang B, Treweek JB, Kulkarni RP, Deverman BE, Chen CK, Lubeck E, et al. Single-Cell Phenotyping within Transparent Intact Tissue through Whole-Body Clearing. Cell. 2014 Aug 14;158(4):945–58.

63. Dey N, Blanc-Feraud L, Zimmer C, Roux P, Kam Z, Olivo-Marin JC, et al. Richardson–Lucy algorithm with total variation regularization for 3D confocal microscope deconvolution. Microsc Res Tech. 2006 Apr;69(4):260–6.

64. Mairal J. Sparse Modeling for Image and Vision Processing. Found Trends® Comput Graph Vis. 2014;8(2–3):85–283.

65. Zukić D, Jackson M, Dimiduk D, Donegan S, Groeber M, McCormick M. ITKMontage: A Software Module for Image Stitching. Integrating Mater Manuf Innov. 2021 Mar;10(1):115–24.

66. Schneider CA, Rasband WS, Eliceiri KW. NIH Image to ImageJ: 25 years of image analysis. Nat Methods. 2012 Jul;9(7):671–5.

67. Helm P, Beg MF, Miller MI, Winslow RL. Measuring and mapping cardiac fiber and laminar architecture using diffusion tensor MR imaging. Ann N Y Acad Sci. 2005 Jun;1047:296–307.

68. Beg MF, Helm PA, McVeigh E, Miller MI, Winslow RL. Computational cardiac anatomy using MRI. Magn Reson Med. 2004 Nov;52(5):1167–74.

69. Fiber architecture of the left ventricular wall: An asymptotic analysis - Peskin - 1989 - Communications on Pure and Applied Mathematics - Wiley Online Library [Internet]. [cited 2022 Dec 19]. Available from: https://onlinelibrary.wiley.com/doi/abs/10.1002/cpa.3160420106

70. Camelliti P, Borg T, Kohl P. Structural and functional characterisation of cardiac fibroblasts. Cardiovasc Res. 2005 Jan 1;65(1):40–51.

71. Poveda F, Gil D, Martí E, Andaluz A, Ballester M, Carreras F. Helical Structure of the Cardiac Ventricular Anatomy Assessed by Diffusion Tensor Magnetic Resonance Imaging With Multiresolution Tractography. Rev Esp Cardiol Engl Ed. 2013 Oct 1;66(10):782–90.

72. Spotnitz HM. Macro design, structure, and mechanics of the left ventricle. J Thorac Cardiovasc Surg. 2000 May;119(5):1053–77.

73. Gilbert SH, Benson AP, Li P, Holden AV. Regional localisation of left ventricular sheet structure: integration with current models of cardiac fibre, sheet and band structure. Eur J Cardio-Thorac Surg Off J Eur Assoc Cardio-Thorac Surg. 2007 Aug;32(2):231–49.

74. Chen J, Liu W, Zhang H, Lacy L, Yang X, Song SK, et al. Regional ventricular wall thickening reflects changes in cardiac fiber and sheet structure during contraction: quantification with diffusion tensor MRI. Am J Physiol-Heart Circ Physiol [Internet]. 2005 Nov 1 [cited 2021 Apr 26];289(5):H1898–907. Available from: https://journals.physiology.org/doi/full/10.1152/ajpheart.00041.2005

75. Peyrat JM, Sermesant M, Pennec X, Delingette H, Xu C, McVeigh ER, et al. A computational framework for the statistical analysis of cardiac diffusion tensors: application to a small database of canine hearts. IEEE Trans Med Imaging. 2007 Nov;26(11):1500–14.

76. Lombaert H, Peyrat JM, Croisille P, Rapacchi S, Fanton L, Cheriet F, et al. Human atlas of the cardiac fiber architecture: study on a healthy population. IEEE Trans Med Imaging. 2012 Jul;31(7):1436–47.

77. Savadjiev P, Strijkers GJ, Bakermans AJ, Piuze E, Zucker SW, Siddiqi K. Heart wall myofibers are arranged in minimal surfaces to optimize organ function. Proc Natl Acad Sci [Internet]. 2012 Jun 12 [cited 2021 Apr 26];109(24):9248–53. Available from: https://www.pnas.org/content/109/24/9248

78. Streeter DD, Spotnitz HM, Patel DP, Ross J, Sonnenblick EH. Fiber Orientation in the Canine Left Ventricle during Diastole and Systole. Circ Res. 1969 Mar;24(3):339–47.

79. Chen J, Liu W, Zhang H, Lacy L, Yang X, Song SK, et al. Regional ventricular wall thickening reflects changes in cardiac fiber and sheet structure during contraction: quantification with diffusion tensor MRI. Am J Physiol-Heart Circ Physiol. 2005 Nov;289(5):H1898–907.

80. Computational cardiac anatomy using MRI - Beg - 2004 - Magnetic Resonance in Medicine - Wiley Online Library [Internet]. [cited 2022 Dec 19]. Available from: https://onlinelibrary.wiley.com/doi/full/10.1002/mrm.20255

81. Lombaert H, Peyrat JM, Croisille P, Rapacchi S, Fanton L, Cheriet F, et al. Human Atlas of the Cardiac Fiber Architecture: Study on a Healthy Population. IEEE Trans Med Imaging. 2012 Jul;31(7):1436–47.

82. Anisotropy of wave propagation in the heart can be modeled by a Riemannian electrophysiological metric | PNAS [Internet]. [cited 2022 Dec 19]. Available from: https://www.pnas.org/doi/abs/10.1073/pnas.1008837107

83. Pope AJ, Sands GB, Smaill BH, LeGrice IJ. Three-dimensional transmural organization of perimysial collagen in the heart. Am J Physiol-Heart Circ Physiol. 2008 Sep;295(3):H1243–52.

84. Mittal RK. Longitudinal muscle of the esophagus: its role in esophageal health and disease. Curr Opin Gastroenterol. 2013 Jul;29(4):421.

85. Scimone ML, Cote LE, Reddien PW. Orthogonal muscle fibres have different instructive roles in planarian regeneration. Nature. 2017 Nov;551(7682):623–8.

86. Diamant NE. Physiology of Esophageal Motor Function. Gastroenterol Clin North Am. 1989 Jun 1;18(2):179–94.

87. Spirka TA, Damaser MS. Modeling Physiology of the Urinary Tract. J Endourol. 2007 Mar;21(3):294–9.

88. Romero D, Camara O, Sachse F, Sebastian R. Analysis of Microstructure of the Cardiac Conduction System Based on Three-Dimensional Confocal Microscopy. Talkachova A, editor. PLOS ONE. 2016 Oct 7;11(10):e0164093.

89. Grant AO. Cardiac Ion Channels. Circ Arrhythm Electrophysiol. 2009 Apr;2(2):185–94.

90. Yan GX, Shimizu W, Antzelevitch C. Characteristics and Distribution of M Cells in Arterially Perfused Canine Left Ventricular Wedge Preparations. Circulation. 1998 Nov 3;98(18):1921–7.

91. Young RJ, Panfilov AV. Anisotropy of wave propagation in the heart can be modeled by a Riemannian electrophysiological metric. Proc Natl Acad Sci. 2010 Aug 24;107(34):15063–8.

92. Niimura H, Patton KK, McKenna WJ, Soults J, Maron BJ, Seidman JG, et al. Sarcomere Protein Gene Mutations in Hypertrophic Cardiomyopathy of the Elderly. Circulation. 2002 Jan 29;105(4):446–51.

93. Levy LM. Brain Mapping Project: Clinical Aspects and Role of Neuroradiology. Am J Neuroradiol. 2013 May;34(5):942–3.

94. Radisic M, Christman KL. Materials Science and Tissue Engineering: Repairing the Heart. Mayo Clin Proc. 2013 Aug;88(8):884–98.

APPENDIX

Table 1: A list of datasets - sections and animals used in this study

Dataset	Orientation of dataset	Animal Sex	Derived from animal number	Cleared (by CLARITY) or Uncleared
SAS1*	Short-axis section	Female	Mouse 1	Cleared
SAS2*				
SAS3*				
SAS4*				
SAS5			Mouse 2	Cleared
SAS6			Mouse 3	Cleared
SAS7			Mouse 4	Uncleared
LAS1#	Long-axis section		Mouse 5	Cleared
LAS2#				
LAS3#				
LAS4#				
LAS5			Mouse 6	Cleared
APEX1*	Apex in short-axis view		Mouse 1	Cleared
APEX2*				
APEX3*				
APEX4*				
RSAS1	Short-axis section	Male	Rat1	Uncleared

*/# indicates serial sections from the same animal

Table 2: A list of reagents and resources used in this study

REAGENT or RESOURCE	**SOURCE**	**IDENTIFIER**
Dye and antibody		
WGA(wheat germ agglutinin)	ThermoFisher	W21404
Monoclonal anti-alpha actinin rabbit Antibody	Cell signalling	D6F6, 6487
Anti Rabbit alexa-647 Goat Antibody	Life technologies	A21245
Chemicals and others		
2, 20-Azobis[2-(2-imidazolin-2-yl)propane] dihydrochloride	Wako Chemicals USA	VA-044
Histodenz	Sigma	D2158
500 μm spacers	SUNjin Lab, Taiwan	IS002
SOFTWARES AND ALGORITHMS		
Matlab	Version: R2019b academic use version	
FiJi	Version: v1.53r	
Blender	The orientation reconstructions were rendered using Python and blender	
C++ and python	For stitching fields of view and rendering orientation reconstructions	
DATA DEPOSITED		
gitfront	[https://gitfront.io/r/haaput/6KGUZMJm8r6R/myofibrometry/]	

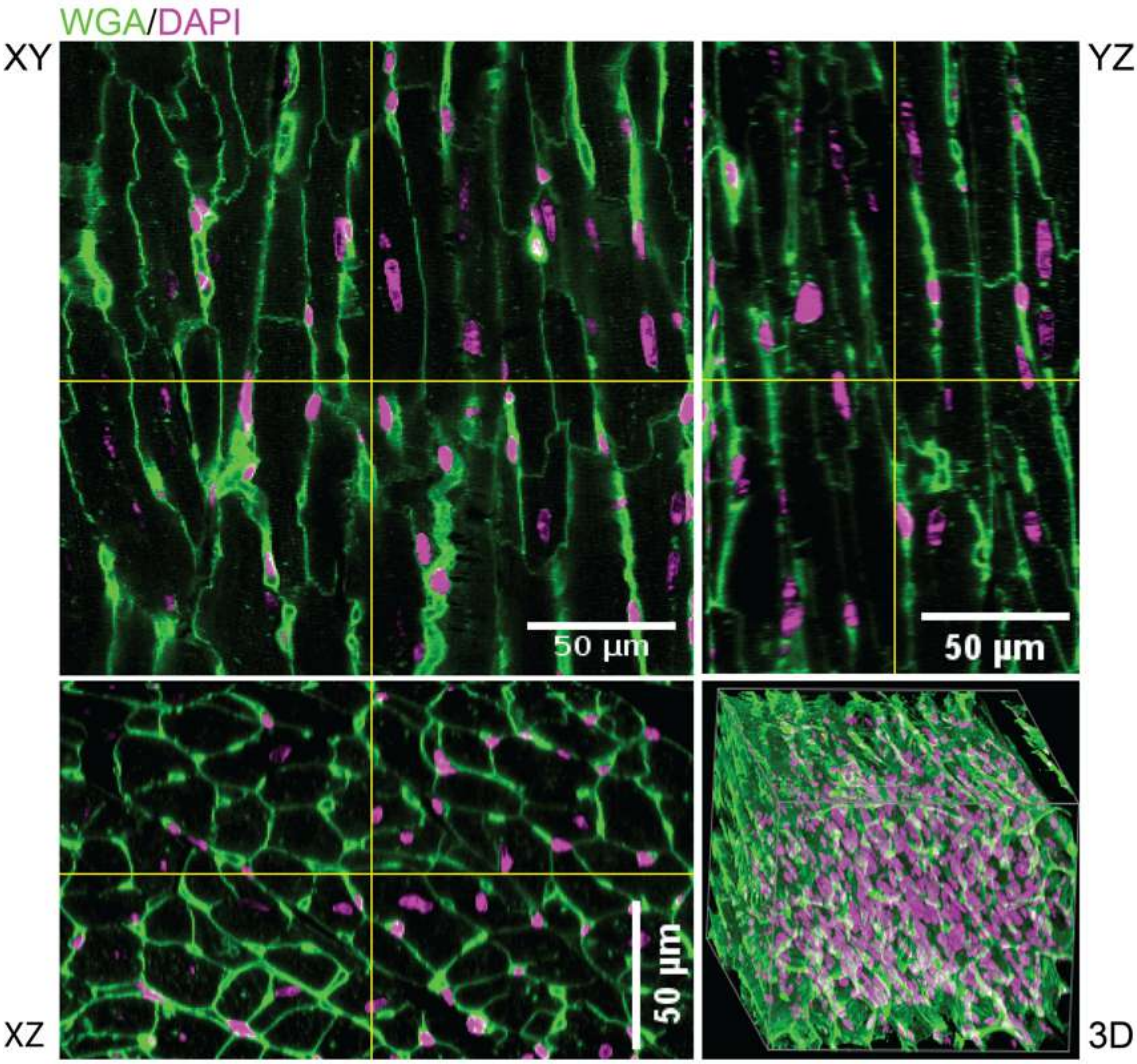

Appendix Figure 1: Representative field of view of 60X imaging.
Orthogonal views and a 3D representative view of cardiomyocytes in long axis plane imaged at 60X are shown; DAPI appears in magenta, WGA-AF633 appears in green and scale bar is 50µm as indicated.

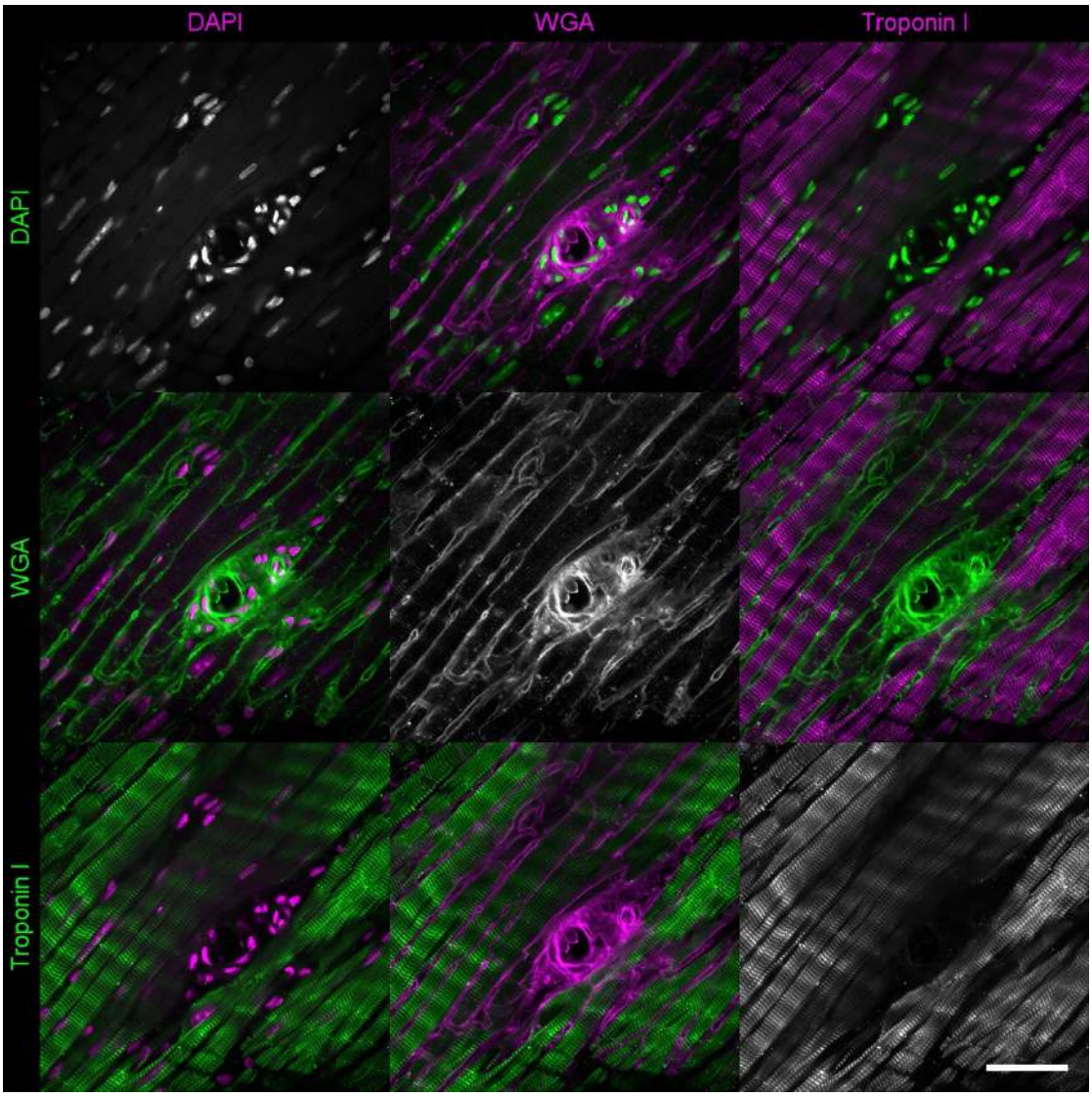

Appendix Figure 2: Representative image of sarcomere staining with Troponin I. Cardiomyocytes in long axis plane stained with Troponin I, DAPI and WGA-AF633 imaged at 60X are shown. Scale bar is 50μm as indicated.

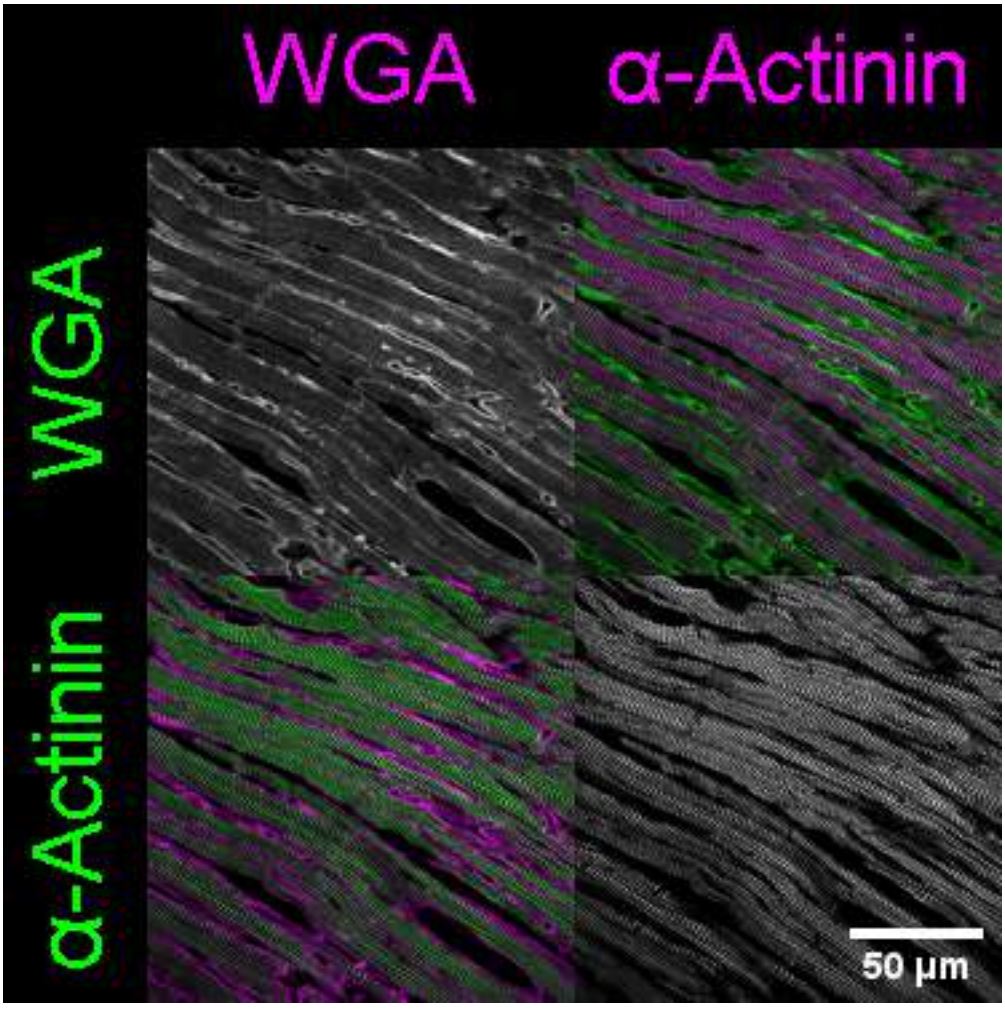

Appendix Figure 3: Representative image of sarcomere staining with α-Actinin. Cardiomyocytes in long axis plane stained with α-Actinin, DAPI and WGA-AF633 imaged at 60X are shown. Scale bar is 50µm as indicated.

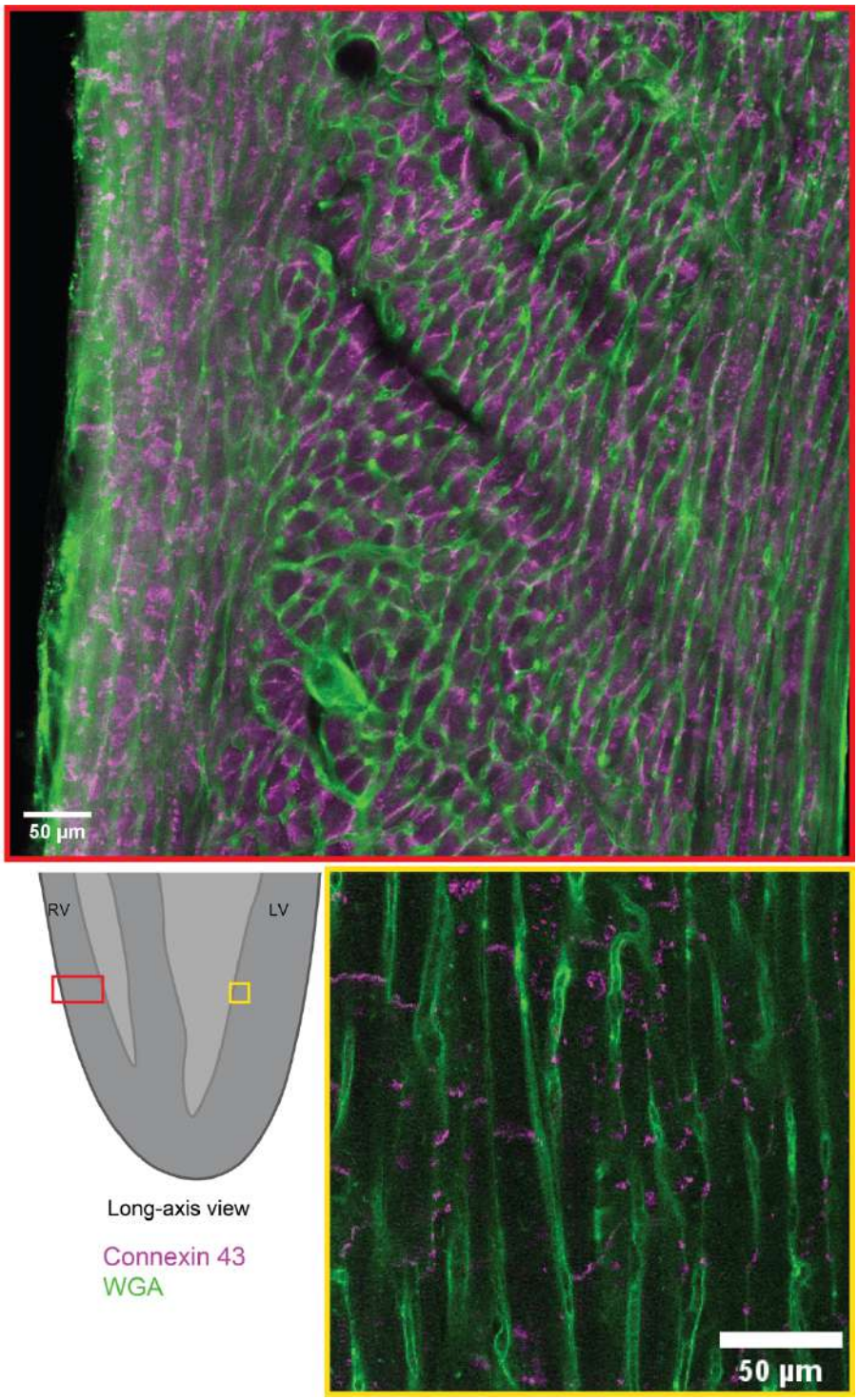

Appendix Figure 4: Representative image of Connexin 43 staining from various heart regions.
Cardiomyocytes from RV wall (in red box) and LV inner wall (yellow box) stained with connexin 43 (secondary AF-640) and WGA-AF488 imaged at 60X are shown. Connexin 43 is expressed in inner, mid and outer ventricular walls. Scale bar is 50µm as indicated.

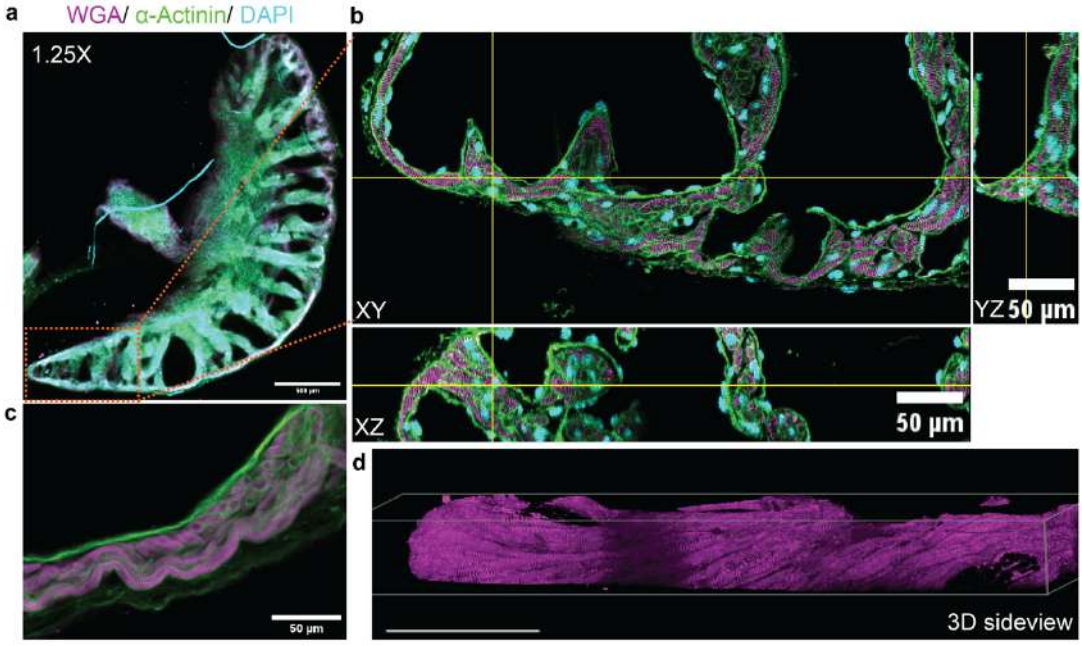

Appendix Figure 5: Representative image of sarcomere staining from mouse atrium. **a.** An overview of atrium stained with DAPI (cyan) WGA-AF488 (green) and α-actinin (magenta) imaged at 1.25X is shown. **b.** A selected region of atrium imaged at 60X is shown in orthogonal views. **c.** A zoom in region of the atrium wall shows cardiomyocytes arranged in different organization. **d.** A 3D view of atrial cardiomyocyte arrangements viewed from sides. Scale bars as indicated.

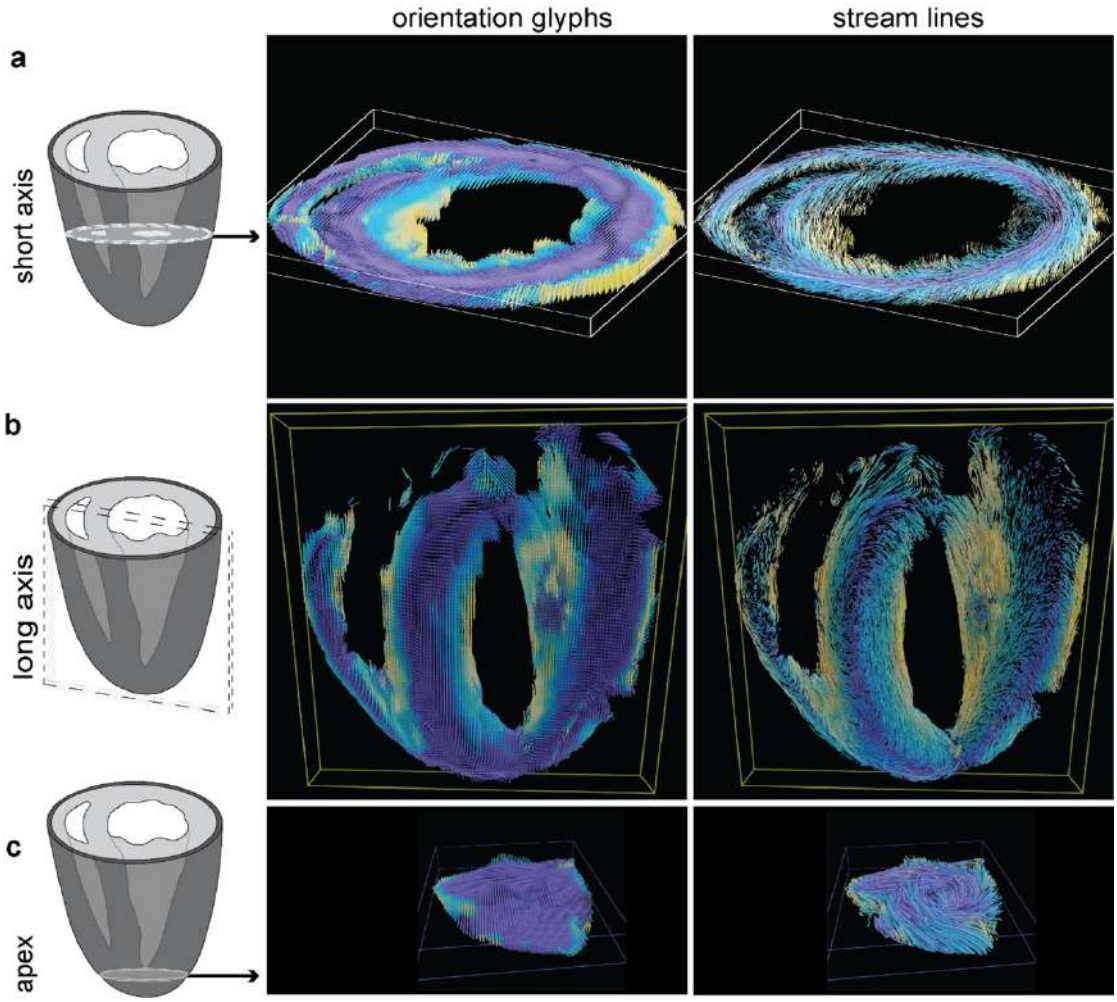

Appendix Figure 6: Long-axis and circumferential myofibers in the heart ventricular walls.
Schematics of the heart ventricle walls and the heart sections analyzed (left); **a.** A short-axis (mid- ventricular region) section, **b.** A long-axis (transverse section) and **c.** An apical section. Structure tensor based orientations are visualized as glyphs (middle) and streamlines (right). The colors follow a parula colormap, where the blue and yellow tones indicate orientations that are in or out of the short-axis plane, respectively.